Single- and Few-Layer Graphene by Ambient Pressure Chemical Vapor Deposition on Nickel

by

Alfonso Reina Cecco

B.S., Instituto Tecnológico y de Estudios Superiores de Monterrey (2004)

Submitted to the Department of Materials Science and Engineering in partial fulfillment of the requirements for the degree of

Doctor of Philosophy in Materials Science and Engineering

at the

MASSACHUSETTS INSTITUTE OF TECHNOLOGY

June 2010

Author .....
Department of Materials Science and Engineering
May 21, 2010

Certified by .....
Jing Kong
Associate Professor
Thesis Supervisor

Accepted by .....
Christine Ortiz
Chairman, Department Committee on Graduate Theses

Single- and Few-Layer Graphene by Ambient Pressure Chemical Vapor Deposition on Nickel

by

Alfonso Reina Cecco

Submitted to the Department of Materials Science and Engineering
on May 21, 2010, in partial fulfillment of the
requirements for the degree of
Doctor of Philosophy in Materials Science and Engineering

Abstract

An ambient pressure chemical vapor deposition (APCVD) process is used to fabricate graphene based films consisting of one to several graphene layers across their area. Polycrystalline Ni thin films are used and the graphene can be transferred from the Ni surface to dielectric substrates in order to integrate them to graphene device prototypes. Uniform single layer graphene can be grown with the same process by using single crystalline Ni with a (111) surface orientation. Raman spectroscopy and electron diffraction characterization is undertaken in order to determine the nature of the layer stacking for the case of multilayer graphene.

Thesis Supervisor: Jing Kong
Title: Associate Professor

Acknowledgments

I am deeply grateful to my advisor Prof. Jing Kong for her continuous encouragement and motivation. Her openness, kindness and care for her students have been vital components of my experience as a graduate student. I am thankful for her patience with me. I am also indebted to Prof. Mildred Dresselhaus for introducing to me the field of Raman spectroscopy which was extremely valuable in the characterization and understanding of the graphene grown. Her endless dedication to her work and her students was very valuable for the completion of this work. I am thankful to all co-workers who I have interacted with during the past few years, specially: Stefan Thiele, Xiaoting Jia, Roland Koch, Sreekar Bhaviripudi, Ki Kang Kim, Mario Hofman, Hyungbin Son, Hootan Farhat, Federico Villalpando, Ya-Ping Hsieh, Kyeon-Jae Lee, Daniel Nezich and Allen Hsu. I learned and received helped from them in many ways. I am also thankful to Jakub Kedzierski, Paul Healy and John Daneu who work in Lincoln Lab for providing Ni thin films and polished Ni single crystals. Their contribution was essential in order to carry out this research project. Finally, I am also thankful to Dr. Gene Dresselhaus whose presence I have enjoyed deeply and from whom I have learned a great deal.

This work was supported partially by NSF Grant DMR 07-04197.

Contents

List of Figures

Chapter 1

Introduction

The search for graphene fabrication methods that allow its integration with potential applications is motivated by this material's exceptional properties. These properties extend from electrical to mechanical aspects. In this thesis, a way to fabricate graphene-based films is presented. This method is based on ambient pressure chemical vapor deposition (APCVD) on nickel surfaces. The films consist of regions with single layer graphene (1-LG) and regions with few-layer graphene (F-LG). The thickness uniformity and the ability to grow films with only 1-LG depend on the substrate used and CVD conditions. The new contributions of the method presented to the current research on CVD approaches to grow graphene are the following:

(1) The ability to grow 1-LG using ambient pressure conditions is demonstrated. This is advantageous from the scalability point of view of graphene production. 2) The films synthesized this way can be isolated from the Ni surface and transferred to other substrates. This is one of the first demonstrations of this possibility and it allows the integration of graphene with different platforms/substrates as prototypes for various applications.

This progress in the CVD of graphene is expected to expand the potential of the material's large scale application in microelectronics. This thesis is organized in the following way. Chapter 2 will be devoted to the description of single- (1 LG) and few-layer graphene (F-LG) in terms of its structure and properties. The current status of graphene fabrication research will be briefly reviewed as well. In chapter 3, the

concept of carbon segregation on transition metals will be discussed. The use of carbon segregation on Ni by means of a CVD process to produce graphene films will be presented. The transfer of the so produced graphene films from the growth substrate to other non-specific substrates will be described also. Chapter 4 will present the effect of the Ni substrate microstructure on the graphene film morphology. Chapter 5 will discuss the effect of segregation rate on the film's morphology and properties. The use of single crystalline Ni using the same fabrication method will be described in chapter 6.In chapter 8, the structural characterization of the material with transmission electron microscopy (TEM), selective area electron diffraction (SAED) and Raman spectroscopy will be presented. Finally, a conclusion chapter is included to summarize the main findings of this research and possible future work along the same lines of research.

Chapter 2

Graphene Properties and Fabrication

2.1 Graphene structure and properties

Graphene can be viewed as a monoatomic plane of carbon atoms arranged hexagonally. A crystal structure is usually formed by a lattice and a basis. The lattice defines the crystal's symmetry and unit cell. The basis defines the number of atoms at each lattice point or within each unit cell. Graphene has a two-dimensional hexagonal lattice (plane group p6m) and a basis of two carbon atoms. The crystal structure of graphene, its lattice and its base are shown in Figure 2-1. The consecutive stacking of graphene layers in the c-axis produces the more commonly known material, graphite. Because of this, graphene has been used historically to understand and predict the electronic properties of graphite. In this work, reference to stacks of more than one monolayer will be utilized. These are typically referred to as few-layer graphene (FLG) or n-layer graphene (n LG). For example, stacks of two, three and four graphene layers are named two- (2 LG), three- (3 LG), and four-layer (4 LG) graphene, respectively.

The bonding between carbon atoms in the graphene structure occurs by sp^2 orbital hybridization. In this configuration, one $2s$ carbon orbital is mixed with two of the $2p$ carbon orbitals. This combination forms three degenerate sp^2 electron orbitals with

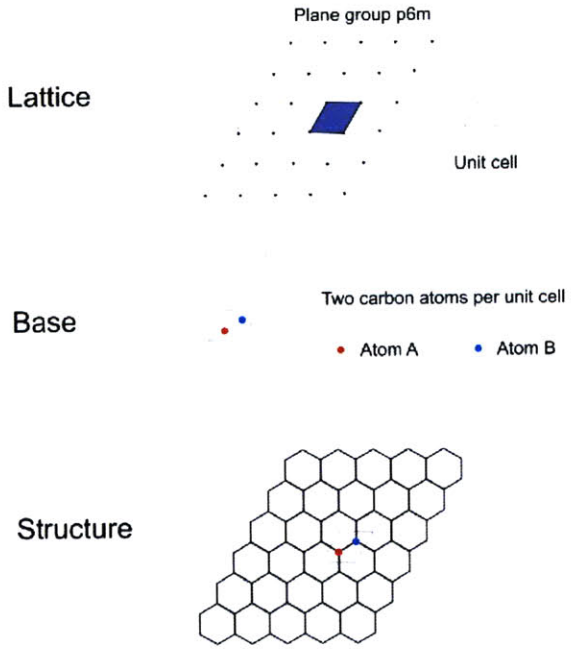

Figure 2-1: Graphene structure.
It is formed by a hexagonal, two-dimensional lattice (plane group p6m) a base of two atoms (A and B). The lattice defines the unit cell of the structure and the base the number of atoms per unit cell.

which each carbon atom forms three sigma (σ) bonds with their nearest neighbors. The bond direction of each sigma bonds lies in the same plane forming the hexagonal arrangement depicted in Figure 2-1. These bonds are responsible for the strong mechanical properties of graphene [1]. Lastly, for every carbon atom there is a half-filled $2p$ orbital that does not participate in the sp^2 hybridization. These orbitals (π orbitals) are oriented perpendicular to the σ bonds and electrons in them are responsible for electrical conduction in graphene and graphite.

The band structure of graphene, first predicted in 1947 by Wallace [2], shows a linear dispersive relationship between the energy of the π electrons and their wave vector in the crystal lattice. This gives rise to the unusual massless Dirac fermion behavior of the electrons [3, 4].

A monolayer of graphene (1 LG) can have a high electron mobility (up to 200000 $cm^2/V\ s$) [5, 6] with high current carrying capability (up to $3 \times 10^8\ A/cm^2$) [7] and mechanical stability [1]. These properties make the material an attractive alternative

for various applications. Its high surface area to volume ratio enables an enhanced sensitivity for the adsorption or desorption of single gas molecules [8]. A single layer absorbs around 2.3% of normally incident light [9], which in combination with its good electrical conduction capabilities, makes it a desired alternative for transparent electrodes. All of these properties drive the interest to find fabrication ways that allow graphene applications. In the next sections, an overview of existing graphene fabrication methods will be presented.

2.2 Fabrication methods

Although there were ways known to generate a monolayer of graphene since the last century, it was not until 2004 that it was possible to isolate a large, high quality monolayer of graphene on a dielectric substrate. The implication of this was the probing of specific properties of graphene for the first time. This was done by the micromechanical cleaving of HOPG or graphite using adhesive tape [10]. The characterization of graphene materials derived from this approach made researchers invest effort to develop other ways to fabricate graphene or to combine and improve previous techniques. These efforts were rooted in the interest to realize this material's applications in the large scale and with low cost. Although the micromechanical cleaving of graphite was not the first known way to produce graphene, it was an important step towards a better understanding and characterization of the material. Some of the first reports on the synthesis of graphene utilized chemical vapor deposition (CVD) and carbon segregation on transition metals. The discussion of both of these processes will be reserved for the next chapter since they are the techniques used for this thesis. This section will start by reviewing the micromechanical cleaving of graphite. The remaining sections will be devoted to summarize the most explored methods of graphene fabrication and the properties of the respective materials produced. Emphasis will be given to research geared towards the scalable production of graphene for electronic applications.

2.2.1 Micromechanical cleavage

In layered materials such as graphite, monoatomic or diatomic layers are stacked one over the other to form a bulk material. Usually, the in-plane atomic bonding of each layer is stronger than that occurring perpendicular to each layer. The latter is typically a van der Waals bonding [10]. Because of this, it is possible to cleave these materials along the in-plane direction of the layers. This procedure is used to obtain a smooth surface of graphite for AFM or STM imaging or other purposes. It can also be implemented iteratively in order to reach the thickness limit of layered materials, a monoatomic layer [10]. One can think of this process as the consecutive removal of cards from a deck or cards. Repeating this process indefinitely leads to the last card at the bottom of the initial deck of cards.

To obtain a monolayer of graphene, this concept can be implemented in the following way. A graphite crystal is laid on top of a clean piece of adhesive tape. Another piece of tape is used to cleave the crystal, resulting in a second graphite crystal on the second piece of tape. This is repeated multiple times using adhesive tape. Each time the original crystal stack will cleave laterally producing thinner graphite pieces on the surface of the tape. Every time the cleavage procedure is repeated, each of the graphite pieces will be cleaved in two. After multiple iterations, one of the tapes with cleaved graphite pieces is pressed onto an oxidized Si substrate (SiO_2-Si). After thoroughly rubbing the tape's surface, to make sure the graphite pieces are in close contact with the SiO_2-Si surface, the tape is stripped from the substrate. Some of the graphite pieces will have adhered to the SiO_2-Si. A few of them will be one layer (1 LG) or just a few layers (FLG) in thickness. Figure 2-2 shows a schematic overview of this procedure.

Identification of the thinnest crystals is done by conventional optical microscopy [10]. Identification is possible since one atomic layer of graphite is capable of creating an amplitude shift of the light reflected from the graphene-SiO_2-Si interface with respect to the light reflected from the bare SiO_2-Si surface. This amplitude shift creates a color contrast between the bare substrate and the graphene on the same surface [11, 12].

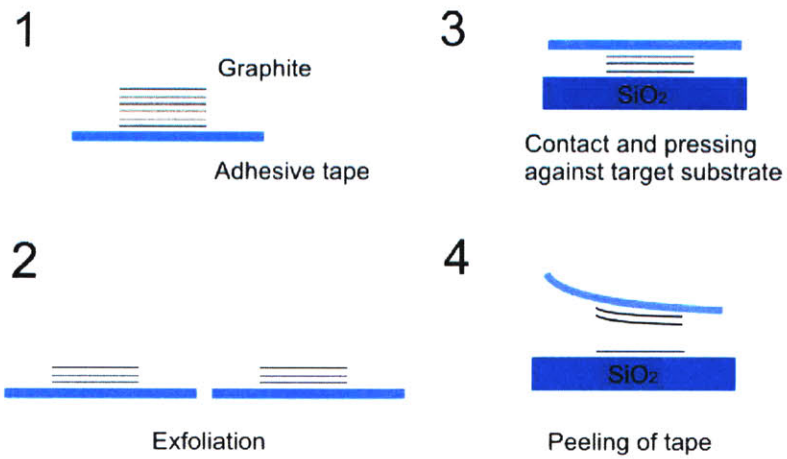

Figure 2-2: Steps involved in the micromechanical cleaving of graphite to produce 1- or few-layer graphene.

This color contrast depends on the number of layers, therefore, enabling the identification of the layer number in such stacks. Figure 2-3 shows a typical image of single-layer (1 LG) and few-layer graphene (FLG) pieces.

In order to apply this method in large scale applications, it is necessary to control the yield and size of the graphene pieces. Recent research has driven progress on this regard accomplishing graphene flakes with around 1 mm in lateral size [13]. However, other methods being currently explored may also show promise to fabricate graphene on the wafer scale.

2.2.2 Transfer-printing methods

These methods utilize the possibility of exfoliating graphene layers from a bulk piece of graphite or HOPG, similarly to the method described above. However, these processes involve the aid of other parameters such as electrostatic forces and adhesion layers on the target surfaces. Furthermore, in order to control the position of the graphene flakes, these methods use patterned stamps from which the graphene materials are placed on the target substrate. This produces an array of graphene flakes with the dimensions of the features of the stamps.

Liang et al [14] used a SiO_2 stamp which they press on a graphite sample in order to break few-layer graphene (FLG) pieces from it. Figure 2-4 summarizes their

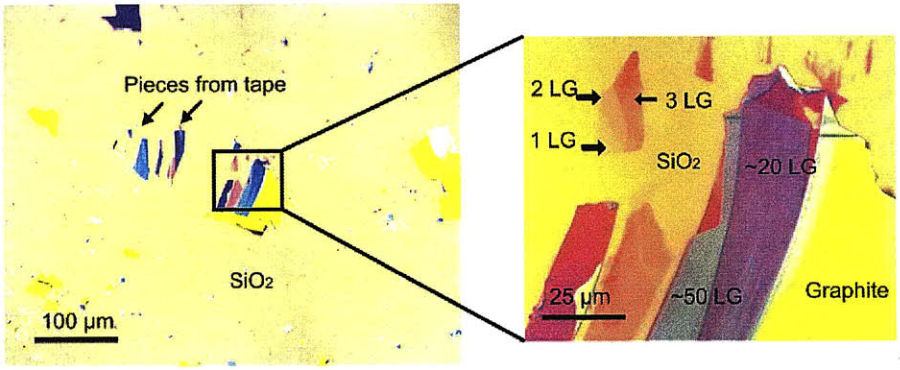

Figure 2-3: Graphene on SiO_2.
Optical images of 1 LG and FLG on an oxidized Si surface (300 nm thickness of SiO_2) transferred from an adhesive tape after the micromechanical cleaving of graphite pieces. The change of color is correlated with the number of graphene layers of the pieces deposited.

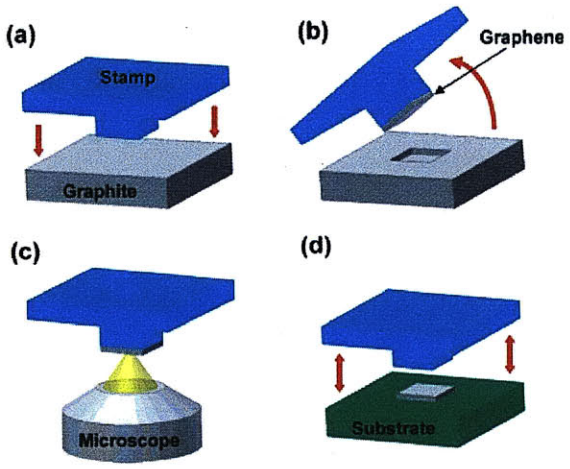

Figure 2-4: Stamping of graphene.
Steps involved in cutting and transferring of FLG from an HOPG piece by the use of a SiO_2 stamp (from ref. [14]). The stamp cuts the FLG pieces from the HOPG piece and picks them up. The stamp is then pressed on the target substrate to deposit FLG pieces on it and further cleave the FLG pieces it carries. Adhesive layers can be used on the stamp and on the substrate in order to increase the adhesion of the FLG pieces to the stamp or substrate while cutting and depositing the pieces.

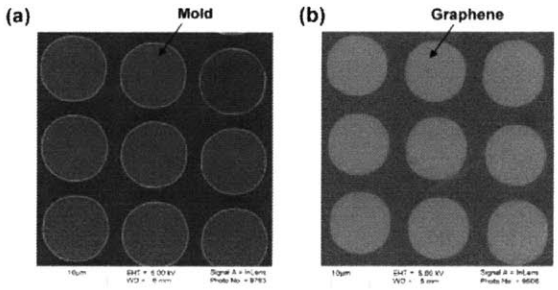

Figure 2-5: SEM images of a SiO_2 stamp.
(a) and an array of FLG graphene pieces (b) produced by the process described in Figure 2-4. From ref. [14]

process. The edges of the features on the stamp apply a shear force on the graphite which causes fracture of the graphite surface along the edges defined by the stamp. When the stamp is separated from the graphite surface, the stamp exfoliates a thin layer of graphite with the dimensions of its features. An adhesion layer on the stamp is used for this step and it is usually a resin-based material that can be spin-coated on the stamp surface. Lastly, the stamp is pressed on the target substrate. Here, a fixing layer can be used to increase the adhesive strength between the graphene on the stamp and the target substrate. In order to release the graphene from the stamp features, the adhesion provided from this fixing layer should be stronger than either the graphene interlayer forces or the graphene-stamp interface energy. The target substrate utilized was SiO_2-Si and it was found that using thermal curable glue or treating the surface with oxygen plasma worked as good fixing layers. Untreated SiO_2-Si surfaces also enable the release of the graphene from the stamp. Figure 2-5 shows SEM images of the pristine SiO_2 stamp and the pattern of FLG generated by applying this process.

Other approaches utilize the graphite samples as the stamp. Here, the graphite surface is patterned to create pillars. This is done by conventional lithographic processes involving an etch mask and reactive ion etching (RIE). Dongsheng et al. [15] utilized the method shown in Figure 2-6 in order to produce such a graphite stamp. Figure 2-7 shows SEM images of the graphite pillars generated on their graphite sur-

face. Similarly to Liang et al. [14], they press this stamp onto the target substrate. Afterwards, the stamp and substrate are separated and a few layers of graphene are exfoliated and left on the substrate. The fact that only a few layers of graphene are exfoliated is explained by analyzing the work required in breaking the interfacial forces involved. The possible scenarios after the separation of the stamp from the surface are shown in Figure 2-8. In one case, the separation occurs between the bottom most graphene layer and the target surface (Figure 2-8(b)). In the second case and third case, it occurs between two graphene layers away from and close to the target surface, respectively. The third case generates a few graphene layers and it is used to explain the generation of thin graphene layers in the work by Dongsheng et al. [15]. The work required in each case is equated to the energy of the interface being broken. It was concluded, with the aid of ab-initio calculations, that the third case involved the least work. This is due to the strong adhesion between graphene and SiO_2 which makes the first scenario unlikely. Furthermore, Dongsheng et al. predict a screening of the graphene interlayer forces due to a strong adhesion between the first graphene layer and the substrate. This screening makes the interlayer forces between graphene layers close to the substrate weaker with respect to the same forces in the bulk of the graphite pillar. Therefore, it was concluded that the third scenario in Fig2-8(d) would be more energetically favorable than the second scenario shown in Fig2-8(c). The weakening of the interlayer forces mentioned above is represented in the work expression as δ.

Other external forces, such as electrostatic forces, can be incorporated in the exfoliation and stamping of graphene [16]. This is done by applying a voltage between the graphite stamp and the target surface as shown in Figure 2-9. The electrostatic charge generated at the stamp-substrate interface assists the exfoliation of graphene layers. Because of the small screening length of electrostatic charges in graphite (≤ 0.5 nm) [16], the electrostatic force acts only on the bottom most graphene layers of the stamp. This allows only a small number of graphene layers to be exfoliated and finally stamped on the desired surface. Figure 2-10 shows a model in which a graphite pillar of 1 μm diameter and 0.5 μm high is pressed against a silicon substrate. Figure 2-

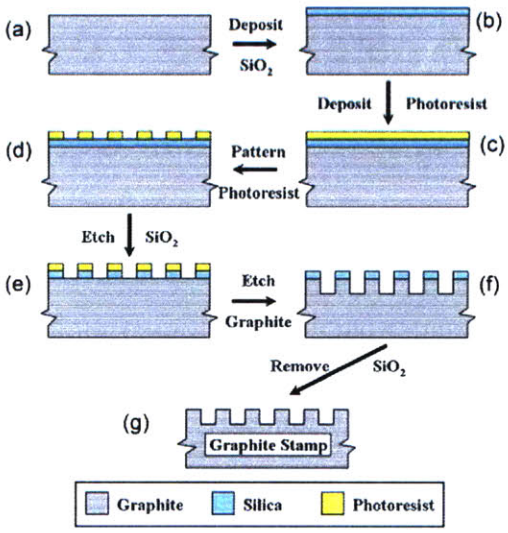

Figure 2-6: Fabrication steps of a graphite stamp by lithography.
From ref. [15]

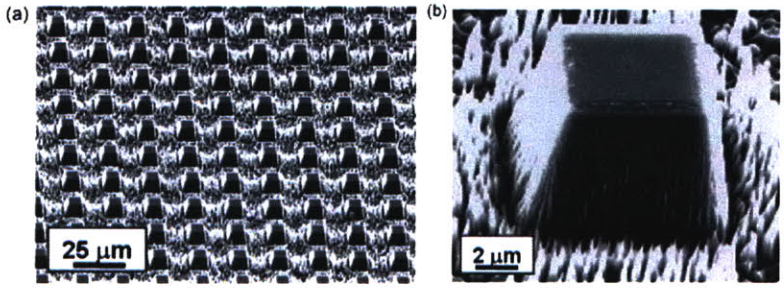

Figure 2-7: SEM images of a graphite stamp.
a) Low magnification image of the array of graphite pillars making up the stamp.
b) High magnification image of one of the graphite pillars fabricated on the stamp.
From ref. [15]

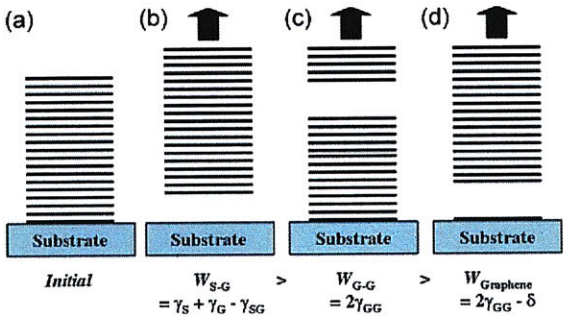

Figure 2-8: The separation of a graphite stamp from a substrate.
a) The stamp is brought into contact with the target surface. b) The separation occurs between the silicon surface and the last graphene layer. The work involved is equal to the sum of the surface energies of graphite (γ_G) and silicon (γ_S) minus the silicon-graphite interface energy (γ_{SG}). c) Case in which the separation occurs between graphene layers far away from the surface-graphite interface. The work involved is equal to the creation of two graphite surfaces ($2\gamma_G$). d) Separation occurring between two graphene layers close to the Si-graphite interface. The work involved is equal to the creation of two graphite surfaces ($2\gamma_G$) minus a screening term. This screening is due to the large interface energy between the Si and graphite which weakens the graphite interlayer adhesion close to the interface. From ref. [15]

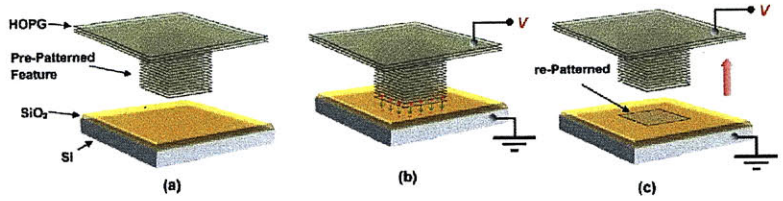

Figure 2-9: Summary of the electric force assisted exfoliation of graphite (EFEG).
a) A graphite stamp is brought into contact with a target substrate. b) While in contact, a voltage is applied between the graphite stamp and the target substrate. This generates electrostatic charges on the graphite and the target surface (opposite sign to each other). Due to the small screening length ($\leq$ 0.5 nm) of electrostatic charges in graphite, the charge is accumulated in the first few graphene layers of the stamp. This results in the preferential exfoliation of just a few graphene layers after separation of the stamp from the surface (c). From ref. [16].

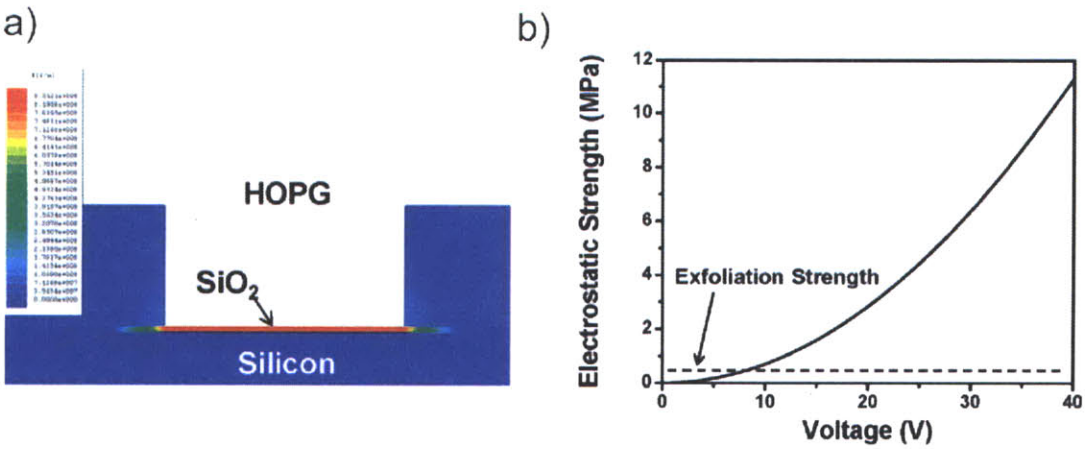

Figure 2-10: Modeling of the EFEG process.
a) Cross sectional view of a graphite pillar in contact with the target Si surface. The magnitude of the electric field, acting in the perpendicular direction of the target surface is shown in a color scale. b) Plot of the electrostatic strength as a function of the applied voltage (solid curve). The dashed horizontal line is the exfoliation strength for one graphene layer. From ref. [16].

10(b) shows a plot of the estimated electrostatic strength versus applied voltage. Notice that for voltages greater than 8.5 V the electrostatic strength is larger than the exfoliation strength. The use of voltages larger than this value should be enough to generate FLG pieces during stamping. This type of stamping allows the generation of arrays of FLG flakes over large areas, typically around 1 cm^2 (Figure 2-11). The yield of graphene flakes on the desired surface is enhanced by a factor of 2 with the application of an electrostatic force. The average thickness of the graphene pieces stamped is 4.5 nm with a standard deviation of 3.0 nm (Figure 2-12).

Further improvements lead to the incorporation of a roller-style electrostatic printing [17]. Here, the stamp is prepared with an HOPG film of 10 μm in thickness. The patterned HOPG film on tape is placed around a metal rod. The stamping occurs by rolling the metal rod over the desired surface while applying a voltage between the metal rod and the substrate (Figure 2-13). The rolling applies a shear force over the graphite surface which assists the electrostatic force in exfoliating the pieces during stamping (Figure 2-14). The role of the shear force is to induce an outslip edge composed of a few layers (see dashed box in Figure 2-14 (a)). As the rolling proceeds,

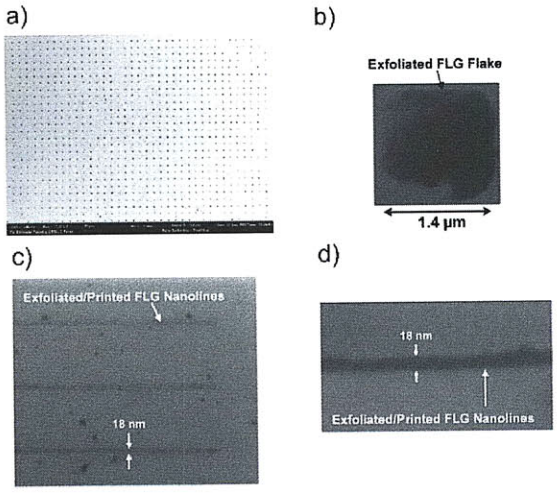

Figure 2-11: Graphene features stamped by the EFEG process.
a) Low magnification SEM image of an array of FLG pieces produced by this process. b) High magnification SEM image of one of the FLG pieces. Low (c) and high (d) magnification SEM images of FLG nanolines generated by the same method. From ref. [16].

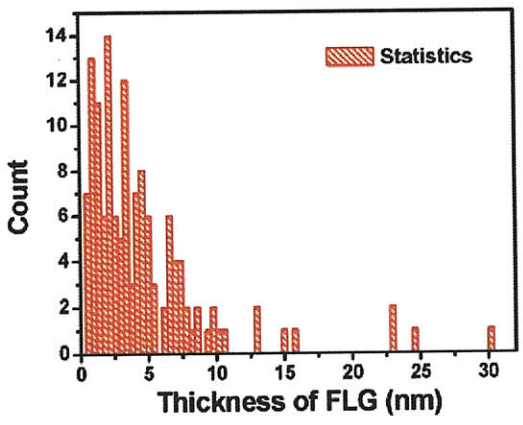

Figure 2-12: Thickness distribution of the features stamped by the EFEG process. The average thickness is 4.5 nm with a standard deviation of 3.0 nm. From ref. [16].

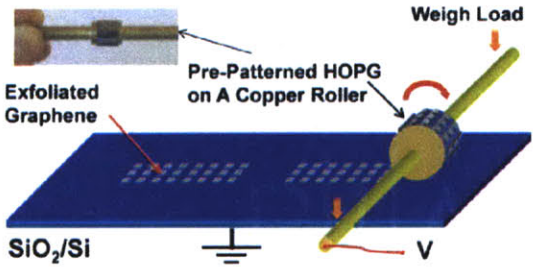

Figure 2-13: Schematic overview of the roller-style electrostatic printing of 1-LG and F-LG.
A copper rod is wrapped with a thin (10 μm) graphite film which has been patterned. A voltage is applied between the copper rod and the target surface as the rod is rolled over the surface. From ref. [17].

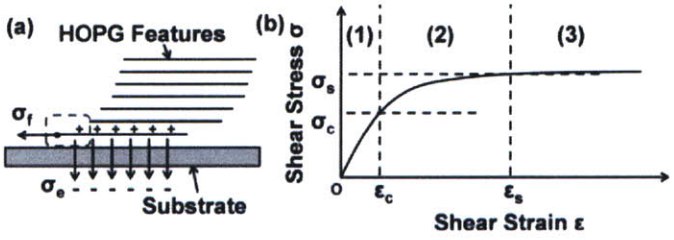

Figure 2-14: Cross sectional view of the graphite-Si interface.
Electrostatic charge at the interface aids in the exfoliation of the graphene layers below the outslip plane created by the rolling of the stamp. b) Plot of shear force vs. shear strain induced by the rolling. The plot shows three regimes: elastic (1), plastic (2) and laminar flow (3). The experiments presented in reference [17] are performed in the laminar flow regime (3).

the electrostatic force peels the graphene layers from the outslip edge. The slip of the shear force significantly weakens the interlayer bonding strength at the outslip edge. This enables the outer 1-2 monolayers to be preferentially exfoliated. From all the graphene flakes produced, 30% and 40% are 1 LG and 2 LG, respectively.

These methods show promise for the fabrication of large arrays (1 cm^2) of single- and few-layer graphene. The graphene features in the arrays are typically in the order of a few tens of microns in lateral sizes. This is compatible to feature sizes in typical electronic devices and prototypes. Furthermore, the possibility of fabricating position-controlled graphene regions at room temperature may find its use in fabrication processes over substrates on which pre-fabricated device components do not

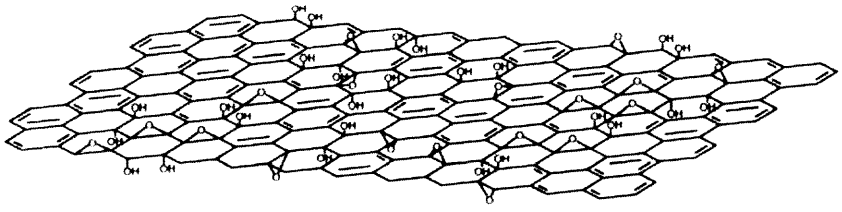

Figure 2-15: Structure of a graphene oxide sheet.
Carbon atoms of the sheet tend to bond to hydroxyl (-OH) groups and epoxide groups (COC). From ref. [20].

resist high processing temperatures. One of the remaining challenges, however, is the degree of control on the number of layers being stamped. Future efforts may lead to more improvements as the understanding of graphite exfoliation is advanced.

2.2.3 Chemical exfoliation of graphite

Graphite can be exfoliated in bulk quantities to produce liquid colloidal systems of graphene or chemically modified graphene (CMG) platelets. One possible route is the oxidation of graphite to generate graphene oxide sheets which are dispersible in water. The oxidation of graphite typically occurs in strong acids and oxidants such as, sulfuric acid (H_2SO_4), sodium nitrate ($NaNO_3$) and potassium permanganate ($KMnO_4$) [18]. Graphite oxide consists of a layered structure of graphene oxide sheets that are hydrophilic in a way that water molecules can intercalate the structure. It is possible to completely separate graphene oxide to produce stable aqueous colloidal suspensions of graphene oxide sheets with procedures such as sonication [19]. This exfoliation is readily accomplished due to the expanded interlayer spacing caused by the oxidation of the graphene sheets and the intercalated water. In Figure 2-15, the most likely graphene oxide model is shown. As seen, the sp^2-bonded carbon network is disrupted and a significant fraction of carbon atoms is bonded to hydroxyl groups (-OH) or form part of epoxide groups (C-O-C). Carboxylic (R-COOH) or carbonyl groups (C=O) (not shown) are also believed to populate the edges of the graphene oxide layers [20].

The graphene oxide sheets produced by this method are electrically insulating, therefore, necessitating reduction procedures to generate electrically conductive graphene. Efforts to accomplish this include the use of chemical methods with reductants such as hydrazine (N_2H_4) [21], dimethylhydrazine ($C_2H_8N_2$) [22], hydroquinone ($C_6H_4(OH)_2$) [23] and sodium borohydride ($NaBH_4$) [24]. Since reduction of the graphene oxide diminishes the material's hydrophilicity, the platelets agglomerate in water and produced a conductive powder when dried. However, it is possible to perform the reduction in the presence of either polymer or surfactants [21] that prevent the sheets from agglomerating after reduction and therefore, producing stable colloids of conductive sheets (see Figure 2-16). This procedure has afforded the ability to incorporate these sheets in polymers to create CMG composites. Alternatively, the stabilization of CMG graphene can also be carried by electrostatic charges induced on the graphene sheets [25]. Here, the graphene oxide is reduced by hydrazine. Shifting the pH level of the original graphene oxide colloid to 10 converts the neutral carboxylic groups to negatively charged carboxylate groups, so that when the graphene oxide sheets are reduced by hydrazine, the negatively charged sheets do not agglomerate.

Reduction of graphene oxide sheets by the methods described above does not restore completely the chemical structure of pristine graphene sheets. Another possibility to create graphene colloidal dispersions is without the use of graphite oxide as the starting material. In this case, graphite, graphite intercalation compounds (GIC) or expandable graphite (a type of GIC) can be used. Sonication of graphite powder can create suspensions of graphene sheets in organic solvents such as N-Methylpyrrolidone (NMP) [26] with relatively lower concentration and yields of single-layer graphene (0.01 mg/ml). Commercial expandable graphite can also be exfoliated by thermal treatment at 1000 °C, re-intercalation with oleum and expansion with tetrabutylammonium hydroxide (TBA) [27]. After this, the suspension of graphene sheets is produced by sonication in dimethylformamide (DMF) with 1,2-Distearoyl-phosphatidyl ethanolamine-methyl-polyethyleneglycol (DSPE-mPEG) as surfactant. Expandable graphite can also produce stable suspensions in water [28]. This is accomplished by rapidly heating expandable graphite to 1000 °C and mixing

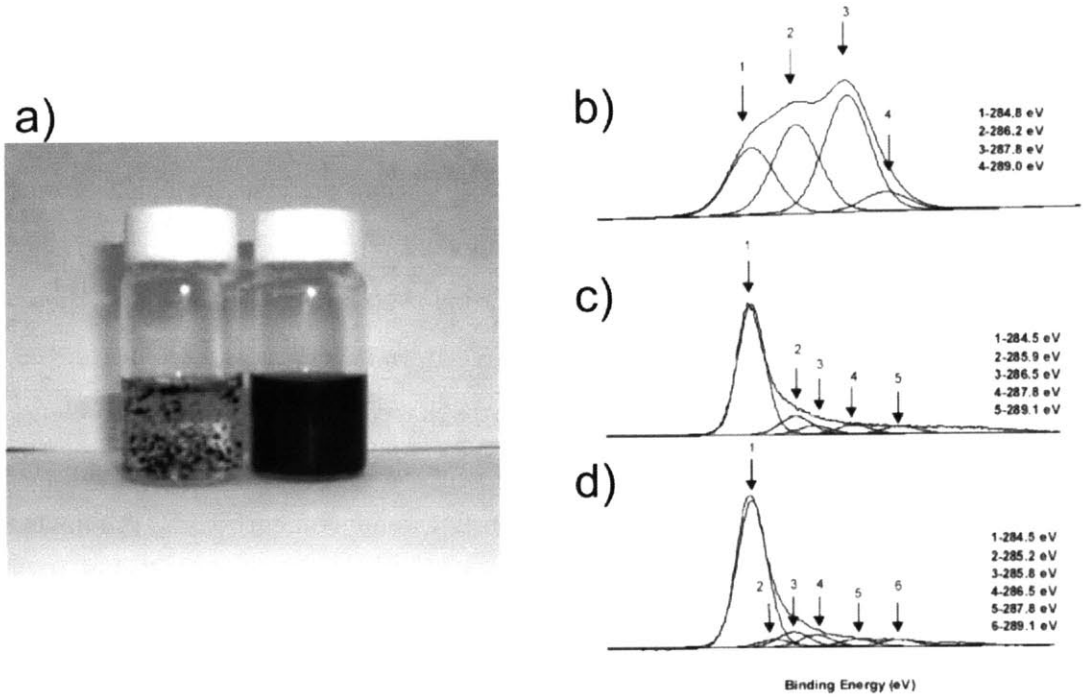

Figure 2-16: Graphene oxide dispersions.
a) Optical images of aqueous dispersions of reduced graphene oxide. The reduction took place without (left) and with (right) poly(sodium 4-styrenesulfonate) (PSS) as surfactant and hydrazine hydrate as the reducing agent. The presence of PSS avoids agglomeration of the graphene oxide platelets. b) XPS spectra of graphite oxide. Five peaks are present; the non-oxygenated ring C (284.8 eV), the C in C-O bonds (286.2 eV), the carbonyl C (C=O, 287.8 eV), and the carboxylate carbon (O-C=O, 289.0 eV). c) XPS spectra of reduced graphene oxide without PSS. d) XPS spectra of reduced graphene oxide with PSS. In both reduced graphene spectra, the non-oxygenated C is the most prominent peak. The oxygenated C peaks are significantly decreased. One additional peak is present in the reduced graphene spectra (285.9 eV) corresponding to the C in the C=N bonds of hydrazones. From ref. [19].

it with 7,7,8,8-tetracyanoquinodimethane (TCNQ) in the presence of several drops of dimethyl sulphoxide (DMSO). The suspension (0.01 mg/ml) is produced after sonication of the mixture in water. It is thought that TCNQ anions adsorb on the sheets and stabilize them in water. Graphene films produced by graphite based suspensions usually exhibit enhanced electrical conductivities with respect to those produced by reduced graphene oxide suspensions [21].

The methods described here enable the production of liquid colloids of graphene sheets that can be easily spin-cast and sprayed on multiple substrate without the need of high temperature processes. Furthermore, these techniques are scalable and low-cost. Current challenges may be the increment and control of the size of the graphene sheets produced.

2.2.4 Graphene by Si evaporation from SiC

Single- and few-layer graphene can be grown over entire single-crystal wafers of SiC. This process relies on the evaporation of Si atoms from the SiC surface. SiC has several polytypes which refer to the type of z-axis stacking of bilayers consisting of Si and C atoms [29]. Examples of the possible stacking sequences of several SiC polytypes are shown in Figure 2-17. Here, the cross section defined by the (1100) plane is shown for different SiC polytypes. Each circle represents the position of a Si atom within each bilayer. The Ramsdell notation is used to refer to each of the polytypes [30]. In this notation, each number and letter are used to define the number of layers and the type of lattice, respectively, of the unit cell formed by the stacking sequence. For example, 4H refers to a hexagonal (H) lattice in which the stacking sequence of SiC bilayers is repeated every 4 layers. Substrates of the 4H and 6H SiC polytypes are the most used in graphene growth (Figure 2-18). The surface used can have two polarities referring to the termination of the SiC surface. These can be either Si-terminated or C-terminated, usually referred to as Si-face or (0001) and C-face or $(000\bar{1})$, respectively (see Figure 2-18).

Even the highest grade of commercial SiC substrates show scratches left from polishing. Therefore, pre-treatments of the surface are performed before graphitization

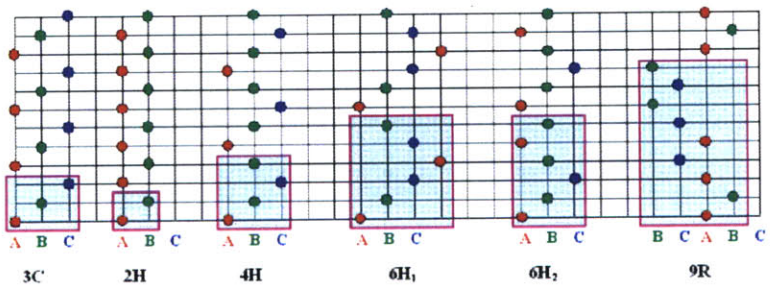

Figure 2-17: Possible stacking sequences of SiC bilayers giving rise to different SiC polytypes. Each colored circle corresponds to the position of a Si atom (for C atoms, see Figure 1-19). The pink box encloses the unit cell of each type of stacking sequence.

of the SiC. This usually involves etching by H_2 at temperatures around 1600 °C [31]. This step helps in the formation of a stepped SiC surface with terraces. Step density and terrace lengths are determined by the initial miscut of the substrate. Oxides are also present on the SiC surface. These can be removed by annealing at ultra high vacuum (UHV) conditions at 900-1000 °C to promote the formation of SiO gas [32]. Evidence of the effect of these pre-treatments on the graphene quality and structure is yet to be proven.

The growth of graphene layers occurs during subsequent annealing of the SiC surface at higher temperatures (1300-1500 °C) and UHV conditions [34]. Both, the Si-face and C-face of 4H and 6H SiC can be used for this process. There are two carbon atoms per unit cell in graphene and one carbon atom per unit cell in SiC, giving area densities of $2/a_G^2$ and $1/a_{SiC}^2$, respectively (where a_G and a_SiC are the lattice constants of graphene and SiC). Therefore, in order to form one graphene monolayer, it is required to obtain the carbon contained in three SiC bilayers ($2/a_G^2/1/a_{SiC}^2$=3.139).

There are differences between the graphene films grown on the Si-face and C-face in terms of growth kinetics, final surface roughness, graphene film structure and stacking order between graphene layers [33]. The number of graphene layers grown on Si-face SiC is usually independent of the process temperature and time (Figure 2-19), contrary to the case of the C-face SiC in which temperature and time strongly influence the number of layers grown. Also, the graphitization temperature is lower

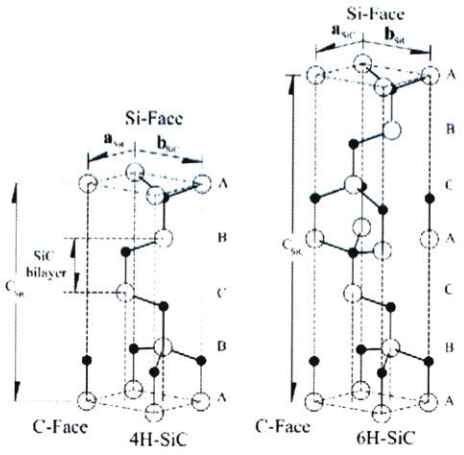

Figure 2-18: Unit cells of the most used SiC polytypes for graphene growth. 4H and 6H are shown on the left and right, respectively. The Si-face, (0001) orientation, in each polytype is shown on the top of each of the unit cells. The C-face, $(000\bar{1})$ orientation, is shown on the bottom of the unit cells. From ref. [33].

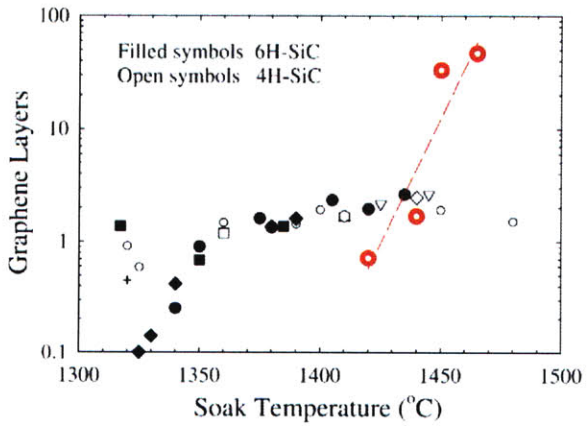

Figure 2-19: Graphene film thickness as a function of temperature. Black filled symbols and black open symbols correspond to the Si-face (0001) of 4H-SiC and 6H-SiC, respectively. Different symbols correspond to different soaking times at the given temperature; (+) 3 min, (square) 5 min, (o) 6 min, (Δ) 7 min, (∇) 8 min and (hexagon) 20 min. Red, partially filled circles correspond to graphene films grown on the C-face of 4H-SiC. From ref. [33].

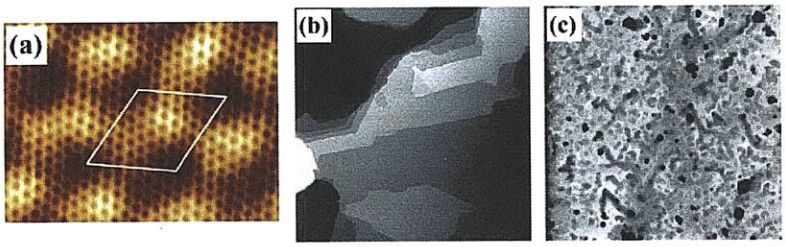

Figure 2-20: Roughness of graphene on SiC.
a) STM image (3.3 nm × 2.4 nm) of graphene grown on the Si-face of SiC showing the hexagonal structure and the quasi-cell (shown in white) formed by the graphene-SiC interface ($6\sqrt{3} \times 6\sqrt{3}$) R30. b)Large scale STM image of the Si-face of SiC after graphene growth (150 nm × 150 nm). c) AFM image of the same surface (9 μm × 9 μm). From ref. [33].

for the Si-face case. Typically, samples of graphene films grown on C-face SiC will have a few tens of graphene layers rather than just a few as in the case of the Si-face. A major problem with the growth of graphene on Si-face SiC is the strong roughening of the surface after graphene growth. This is shown in the scanning tunneling microscopy (STM) and atomic force microscopy (AFM) images shown in Figure 2-20. The average terrace size after graphitization is no larger than 50 nm with an rms roughness of 0.17 Å. This is compared to 1-2 μm long SiC terraces before graphitization. In contrast, an AFM image of the surface of C-face SiC after graphene growth is shown in Figure 2-21. The average terrace width is typically larger than 1 μm and the rms roughness is less than 0.05 Å. Typically, C-face films preserve the pre-graphitized substrate step density.

Low energy electron diffraction (LEED) is one of the most used tools to characterize the structure of the graphene films grown on SiC. Figure 2-22 shows representative LEED patterns of Si-face and C-face SiC after surface graphitization with 2 and 7 graphene layers, respectively [35]. The LEED pattern for the Si-face shows both the diffraction rods for graphite, $(hkl)_G$, rotated 30 degrees from the diffraction rods for SiC, (hkl). The rest of the diffraction spots correspond to the $(6\sqrt{3} \times 6\sqrt{3})$R30 surface reconstruction which corresponds to the graphene/SiC interface. This type of reconstruction is typically observed before graphene formation and it is regarded

Figure 2-21: AFM image of graphene grown on the C-face of SiC. The image size is 8 μm $\times$ 8 μm. From ref. [33].

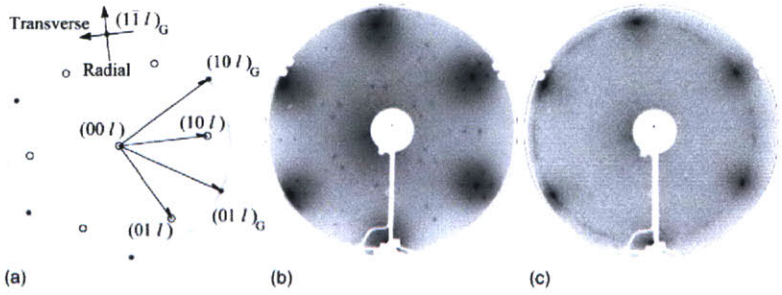

Figure 2-22: Low energy electron diffraction of graphene on SiC. a) Schematic of reciprocal space of graphite over SiC. Graphite diffraction rods (filled circles) are rotated 30^o from those of SiC (unfilled circles). Radial and transverse scans relevant for Figure 2-23 are also shown. b) LEED pattern for 2 graphene layers grown on Si-face SiC. c) LEED pattern for 7 graphene layers grown on C-face SiC. From ref. [35].

as a precursor of graphene growth on the Si-face. The LEED pattern for the C-face shows only diffraction rods corresponding to the graphite lattice [35]. The $(6\sqrt{3} \times 6\sqrt{3})$R30 interface reconstruction does not occur on this face. The diffuse ring along the graphite spots initially suggested azimuthal rotational disorder between graphite crystals with AB stacking of its layers. However, later experiments showed this was not the correct interpretation and attributed this disorder to the unique rotational stacking of graphene layers that distinguishes the graphene grown on the C-face [36].

This is one of the main differences between the graphene films of both surfaces. Hass et al. [36] explains the azimuthal streaking in the LEED pattern of C-face

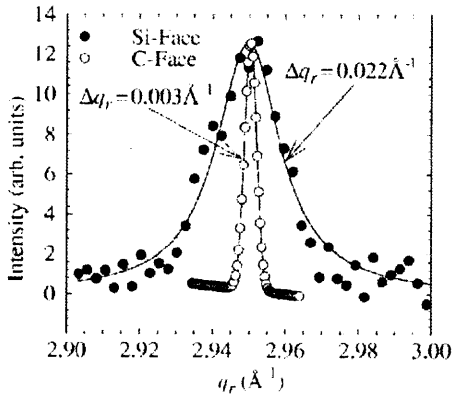

Figure 2-23: LEED radial scans of graphene on SiC.
Scans along the (1,-1,1.5) graphite rod for graphene grown on Si-face (filled circles) and C-face SiC (unfilled circles). From ref. [35].

graphene (Figure 2-22) in the following way. Besides the prominent peak at 30° from the $[10\bar{1}0]$ SiC direction, X-ray azimuthal scans reveal two additional diffused peaks split at symmetrical rotations of ±2.2° around the same SiC direction. These three rotational phases coincide with angles corresponding to both a graphene-SiC and a graphene-graphene commensuration, therefore, explaining the preferential existence of these rotations. Further surface x-ray diffraction (SXRD) experiments suggest that stacking faults on these graphene films occur every 1.6 to 2.5 layers. Due to this large stacking fault density, there is a weak interlayer interaction which helps to preserve the symmetry of the graphene sheets. The reason why multilayer graphene on C-face SiC behaves like an isolated graphene layer is attributed to this structural property of C-face graphene [36].

The superior structural quality of the graphene grown on the C-face is also suggested by SXRD studies and transport measurements [37, 38]. Figure 2-23 shows a radial scan along the SXRD $(10l)_G$ rod for Si-face and C-face graphene. The linewidth Δq_r is inversely proportional to the crystal size ($L = 2\pi/\Delta q_r$). Initial x-ray studies of this kind estimated a lower limit on the average graphene crystal size to be 100 nm and 300 nm for the Si-face and C-face cases, respectively [37, 38]. However, these measurements are limited by the fact that graphene from adjacent steps and terraces scatters incoherently. In fact, the graphene coherency length may be larger than

what these SXRD studies imply. This is supported by STM studies showing that graphene can grow continuously and coherently across SiC steps [39]. More detailed studies are needed to characterize more accurately the lateral domain size of these films. Kedzierski et al. [38] have shown that significantly higher mobilities of 500-5000 cm^2/V s are obtained for top gated graphene transistors on the C-face compared to 600-1200 cm^2/V s for the Si-face. However, recent improvements in the graphene growth process on the Si-face have resulted in surface roughness, thickness uniformity and device mobilities improvements [40]. These improvements also included processing under atmospheric pressure, therefore, making the growth of graphene on SiC more scalable and less costly.

The graphene films grown on SiC have the advantage of growing on a dielectric substrate on which transistors and electronic devices can be built. However, other applications require the use of graphene on substrates with other properties such as flexibility and transparency. Efforts aiming towards the large scale transfer of these graphene films are underway. This would be an important step due to the possibility of implementing the unique properties of these graphene films. The peculiar characteristics of the SiC-graphene system deserve its own attention and careful characterization.

2.3 Summary

The methods presented in this chapter represent most of the effort in exploring ways to fabricate graphene in a large scale in the last few years. Methods involving CVD and carbon segregation will be presented in the next chapter since these are relevant to the work presented by this thesis. The progress done in graphene fabrication research has proved the possibility of generating FLG films over wafer size areas. Some of these methods involve processing at room temperature which is highly desirable for applications involving materials with low operating temperatures. Two common challenges to be addressed in all of these methods is the controllability of the number of layers being generated and the size of single crystalline domains. These have implica-

tions on the type of electronic properties obtained from devices or applications made. Furthermore, future work should involve the detailed characterization of the structure and electronic properties of the materials fabricated by each method explored. In this regard, the case of graphene grown on SiC seems to be the most studied and better known. In the SiC case, important differences in structural and electronic properties were found between graphene films grown on different SiC polytypes and faces. The same must be suspected for graphenes processed differently, especially those derived by chemical methods such as reduction of graphene oxide and CVD.

In the next chapter, the use of CVD and carbon segregation will be presented as an addition to the variety of methods being explored. The use of CVD and the use of carbon segregation to generate 1 LG have been known previously. Both methods had been implemented independently. In this thesis, CVD is used as an enabling platform for the generation of carbon segregation on Ni surfaces to form a FLG film. As an addition, this process is done in ambient pressure CVD (APCVD) and it enables the transfer of the graphene films to other substrates at room temperature. In this way, the method presented aims to combine the advantages of several of the processes presented in this chapter, such as scalability, low cost, non-specificity of target substrates, high conductivity and room temperature deposition.

Chapter 3

Single- and Few-layer Graphene Films by by Ambient Pressure CVD

The production of graphene on transition metals is relevant due to its scalability and its potential to control graphene feature locations. Its development is founded on the studies of graphite growth which were explored starting in the 1960s. Such studies involved graphite grown by hydrocarbon pyrolysis over transition metals (or CVD) and graphite grown from melts of transition metals. There are different mechanisms by which graphite and graphene grow on transition metals. For the purposes of this chapter, it is necessary to emphasize the distinction between processes based on: i) CVD direct deposition, ii) carbon segregation, and iii) their combination (CVD-enabled carbon segregation).

Growth by direct CVD deposition is due to carbon atoms adsorbing on a substrate from the gas phase. These atoms are typically produced by the pyrolysis of a hydrocarbon at elevated temperature assisted by the catalytic activity of the substrate. Growth by carbon segregation occurs due to the supersaturation of a liquid or a solid phase material. Supersaturation usually occurs during a cooling stage in the process due to the temperature-dependent solubility of carbon in the host material. Lastly, it is possible to combine these two mechanisms. Here, the carbon generated

during pyrolysis diffuses to the bulk of the substrate and then precipitates in the form of graphene and graphite. Such saturation can be induced either by cooling or by increasing the carbon concentration to the point of saturation at a constant temperature. The work presented in this chapter involves the growth of FLG films by carbon segregation where CVD is used to introduce carbon to the bulk of a Ni thin film. Formation of the FLG film occurs by saturation of the Ni film during cooling.

It is also helpful to define the differences between segregation and precipitation. Segregation will refer to the enrichment of a particular constituent of a mixture of two or more components to the free surfaces or interfaces of the mixture. Segregation occurs without a transformation of phase in the mixture. The mixture can be a solid solution of the components where one of the components is the host material and the rest are the solutes. Such solutes can exist within a crystalline host by occupying interstitial sites. Precipitation refers to the formation of a new phase in the mixture in question. That is, precipitation occurs due to a transformation of phase occurring in the mixture or solid solution due to a perturbation such as a fluctuation in local solute concentration or a supersaturation of the mixture. Usually a precipitation event can be preceded by one of segregation. For example, the enrichment of particular species at an interface can increase the local concentration of a solute beyond the equilibrium point, therefore, triggering the precipitation of a second material phase at such interface.

This chapter will first discuss previous work on the growth of graphene and graphite by carbon segregation and CVD direct deposition. Afterwards, an ambient pressure CVD (APCVD) method to induce the growth of FLG films by carbon segregation will be presented. Also the transferring of such films to other substrates will be discussed.

3.1 Graphite and Graphene by Carbon Segregation

A popular way to obtain single crystals of graphite in the first half of the $\times\times$ century was the purification of flakes of natural graphite [41]. It was understood that such graphite was formed after precipitation from solution in mineral mix [42]. It was later discovered that graphite was also produced in steel-making (kish graphite) during the cooling of steel. This was explained by steel's high solubility of carbon impurities which precipitated as highly crystalline graphite upon cooling. Further developments in the production of graphite crystals came along during the 1960s [41, 43, 44]. Such processes relied on the formation of a melt of transition metals (solvent) containing carbon impurities (solute). The carbon solute was introduced from the graphite crucible on which the melt was formed at high temperatures. Supersaturation by cooling [41] or the creation of a temperature gradient across the body of the melt [44] induced the segregation of carbon to the surface of the melt and finally the formation of graphite. Figure 3-1 shows a schematic of the experimental set-up used by Austerman et al. [44] to create a steady state temperature gradient in a metal melt.

The segregation of carbon to the surface of a metal in the solid phase was studied by various groups during the 1970s. Derbyshire et al. [45, 46] deposited amorphous carbon (50 nm thick) on cold foils of nickel. Afterwards, the foils were heated to 950 °C, a point at which they reported the disappearance of the deposited carbon. They repeated the procedure until the deposited carbon did not disappear when heated to 950 °C. They assumed that the carbon film disappeared due to the dissolution of carbon to the bulk of the Ni foils and that saturation was reached when the last amorphous carbon film was intact upon heating. At the saturation point, they heated up their sample to 1050°C and observed that the carbon film that was not dissolving previously was now doing so. Afterwards, the sample was cooled back to 950 °C and instantaneously a graphite film formed on the nickel surface. Carbon atoms dissolved in the Ni foil were now segregating on the Ni surface and forming graphite.

Blakely et al. [47] in particular studied the segregation of carbon to a Ni(111)

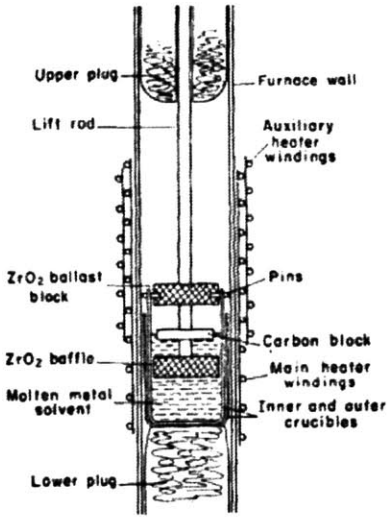

Figure 3-1: Setup used to induce a thermal gradient across a metal melt. Graphite grows from dissolved carbon at the colder surface of the melt. From ref. [44]

surface. Such studies were primarily aimed towards understanding the segregation of impurities in metals since such segregation contributed to the hardening of metal structures. With their work, they realized that a graphene monolayer could be grown on a Ni(111) surface. They introduced carbon into a Ni substrate by contacting the top Ni(111) surface of their samples with a graphite piece at an elevated temperature. After equilibrium is reached, the concentration of carbon in the metal is known. Afterwards, they heated the Ni(111) substrates at UHV conditions. During cooling of the samples, they observed that carbon segregated at the Ni surface and formed a monolayer of graphite. As cooling proceeded, the precipitation of a graphitic phase consisting of multiple graphene layers was detected 100 K below the temperature at which the monolayer formed. The carbon coverage was quantified by Auger spectroscopy. Figure 3-2 shows the Auger peaks of carbon and Ni (270 eV and 62 eV, respectively), taken from the Ni(111) surface, as a function of temperature. The first and second steps in the Auger intensity curves correspond to the coverage of the surface with one graphite monolayer and the precipitation of additional graphite layers, respectively.

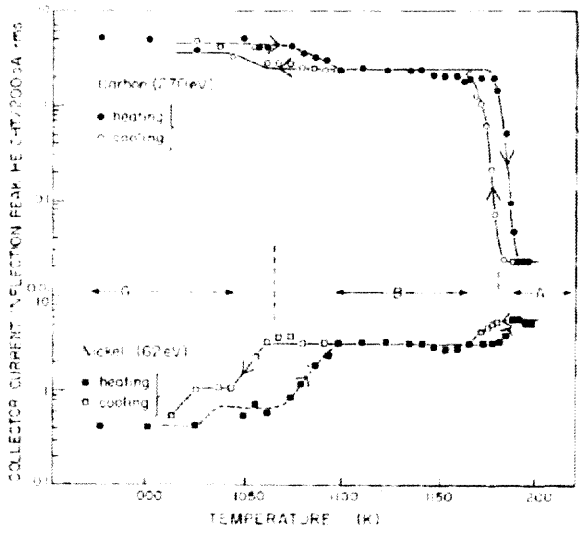

Figure 3-2: Equilibrium segregation of carbon to a Ni(111) surface.
Intensity of the Auger peaks from Ni (62 eV) and C (270 eV) as a function of temperature measured during cooling (open squares) and heating (filled squares) of a Ni (111) substrate containing carbon impurities in solution. The carbon impurities segregate while cooling, reflected by the sudden increase in carbon Auger signal close to 1200 K. After this transition, the intensity is constant for a range of 100 K. In this range, the surface of Ni(111) is covered with one monolayer of graphite. The lower temperature transition corresponds to the initiation of graphite precipitation. From ref. [47]

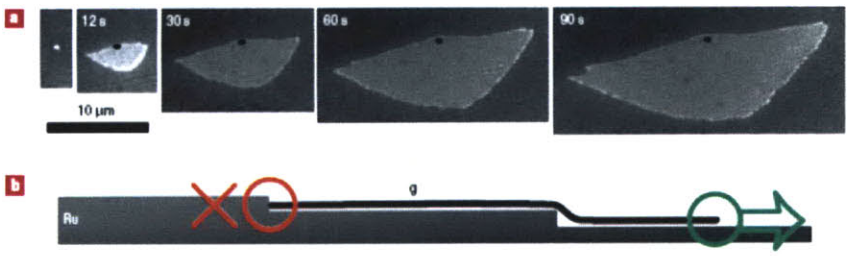

Figure 3-3: Graphene grown on Ru.
a) Low energy electron microscopy (LEEM) images of a graphene domain growing on a Ru surface by carbon segregation. b) Mechanism of graphene growth. Graphene extends across steps in a downhill manner. From ref. [49]

The temperature dependent solubility of carbon in Ruthenium was used by Sutter et al. [48] to grow 1 LG and 2 LG. The growth occurred expitaxially on a Ru(0001) surface under UHV conditions. In their process, carbon is evaporated over Ru(0001). At 1150 °C carbon is absorbed by the Ru bulk. The samples were cooled slowly to 850 °C to promote the formation of 1-LG and 2-LG. The growth of 1-LG and 2-LG islands, as large as 200 μm, was observed by in-situ electron microscopy and LEED after carbon segregation. Remarkably, such islands grew continuously across the steps of the Ru surface suggesting that every island was a single crystal (Figure 3-3(a)). The growing graphene glides across the surface by stepping down on each of the surface steps. The growth of the islands can only proceed in this direction (3-3(b)). Sutter et al. also conclude that the first graphene layer growing on such substrate is strongly bound to the Ru surface and therefore looses its electrical conductivity. Electrical conduction is only observed for the second layer growing on the Ru surface.

The segregation of carbon to grow graphene has been known since the 1970s and it was recently employed as a means to fabricate this material. These processes are similar to the graphite growth from melts developed in the 1960s. However, the latter involves carbon segregation from a liquid phase. The focus on transition metals in these processes was due to the advantages posed by the high carbon solubility and relative lower melting temperature [44] of the metals employed. In the next section, the growth of graphene and few-layer graphene by direct CVD deposition

over transition metals will be discussed.

3.2 Graphite and graphene by CVD

In graphite growth research, the exploration of carbon segregation from melts was paralleled by the use of pyrolysis of carbon containing gases. This also took place early in the 1960s [50, 51, 52]. Initially, pyrolysis was done over non-metallic substrates such as porcelain. Banerjee et al. [50] realized that the rate of carbon formation and the structure of the graphite film formed was different depending on the substrates used. Specifically, they realized that graphite films grown over nickel had a higher degree of crystallinity compared to those grown on other substrates such as porcelain, copper and platinum. Moreover, an enhanced rate of carbon formation was observed for the case of nickel [50]. Karu et al. [51] and Presland et al. [42] used pyrolysis of methane (CH_4) and acetylene (C_2H_2), respectively, over nickel. The choice of such hydrocarbons was based on the thought that transition metals catalyze the dehydrogenation of aliphatic hydrocarbons such as CH_4 and C_2H_2. This led to more work on the growth of graphite by pyrolysis over nickel and other transition metals [51, 42]. Specifically, nickel, iron and cobalt were found to be good catalysts for graphite growth [45]. The crystallinity of the material produced by pyrolysis of hydrocarbons over transition metals was further improved by annealing it at inert atmospheres and high pressures (400 atm) at temperatures of 3000°C. This work was pioneered by Ubbelohde and Moore [52] in the early 1960s and it allowed the production what is today known as highly oriented pyrolytic graphite (HOPG).

The choice of nickel and other transition metals was based on their dehydrogenation ability rather than their high carbon solubility like in the case of carbon segregation. Indeed, during early experiments it was not clear whether the graphite grown on nickel was formed directly from the carbon produced during the hydrocarbon decomposition or if it involved the dissolution of carbon into the bulk followed by precipitation of graphite [42]. Presland et al. initially theorized that the former was the more likely on the basis that the cooling of their foils would only take place

in a few seconds, making the formation of highly crystalline graphite during cooling unlikely. Later in the 1970s it was realized that the pyrolysis processes could also involve the dissolution-precipitation mechanism. [45, 46]. This took place while carbon segregation studies on nickel were better understood by Derbyshire et al. [45, 46] (discussed in the last section).

The direct deposition of graphite with CVD without dissolution-precipitation can be accomplished either by: i) the use of lower CVD operating temperatures or ii) the use of metallic substrates which have negligible carbon solubility at the desired CVD temperature. Most of the reports on graphite growth by CVD are unclear about whether diffusion to the bulk of the metal substrates takes place during the process [53, 54, 55]. A clearer differentiation between both mechanisms emerged as more work was done aimed towards the lowering of CVD temperatures [56] and the growth of thinner graphite films [54].

The growth of a monolayer of graphite on Ni(111) by CVD was possible using relatively lower temperatures (500-600°C), UHV conditions and hydrocarbons such as ethylene and propylene [57, 58, 59]. The growth of 1 LG this way was applied in the study of surface phonon properties of 1 LG over transition metals [59]. Coverage of the Ni(111) surface with one monolayer was accomplished by the exposure to a few langmuirs (1 L = 1×10^{-6} Torr·s) of the hydrocarbon used [57, 58, 59]. The growth of 1 LG was reported to be self limiting. This observation was explained by the fact that the catalytic activity of the Ni(111) surface was negligible once covered with one monolayer of graphite. At the hydrocarbon partial pressure in operation, the reduced catalytic activity would not generate enough carbon species to sustain further graphite growth.

Following the increased interest in graphene research during the last few years, the literature on CVD growth of graphene became more specific about whether the growth occurred via a direct deposition or carbon by segregation. Loginova et al. [60] intentionally used low temperatures (500-700 °C) to avoid diffusion to the substrate bulk during the evaporation of C atoms over Ru(0001). In contrast, Sutter et al. [49] used higher temperature (850-1150 °C) to promote carbon dissolution and segregation

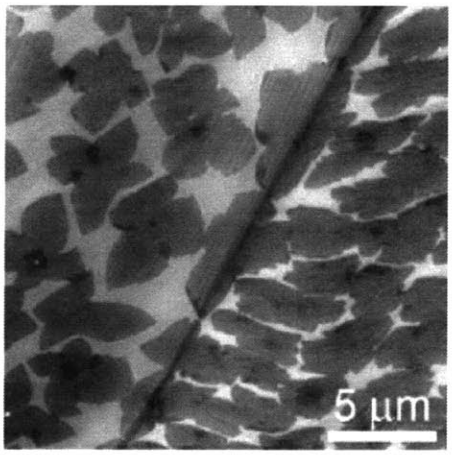

Figure 3-4: Graphene grown on Cu foils.
Graphene domains (darker features) growing on a Cu foil. The brightest features correspond to the metal surface. From ref. [62]

for the growth of 1 and 2 LG. These two examples represent the ability to use different temperature ranges to select the mechanism by which graphene grows.

The use of other metals such as Cu, with negligible carbon solubility at high temperatures, is an alternative way to grow 1 LG without carbon dissolution. Indeed, this was proved possible with Cu. Li et al. [61] used Cu foils and low pressure CVD (LPCVD) to grow 1 LG by direct CVD deposition. The temperature at which the growth occurs is 1000 °C. At this temperature other metals such as Ni and Ru show significant carbon diffusion to the bulk. It was suggested that the growth by Li et al. is also self-limiting due to the reduced hydrocarbon decomposition after the surface is covered with graphene. Figure 3-4 shows a scanning electron microscopy (SEM) image of monolayer graphene domains growing on the Cu foil surface.

Li et al. [62] also showed the differences between the graphene growth mechanisms on Ni and Cu at the same temperature. It was shown that at elevated temperatures close to 1000 °C graphene films growing on Ni grew by carbon segregation from the bulk whereas those grown over Cu grew from carbon atoms adsorbed on the Cu surface (Figure 3-5). This was show by switching the hydrocarbon source between C^{12} and C^{13} labeled methane during a CVD process. Spatial distributions of the carbon isotopes forming the graphene could be identified by mapping the Raman G-

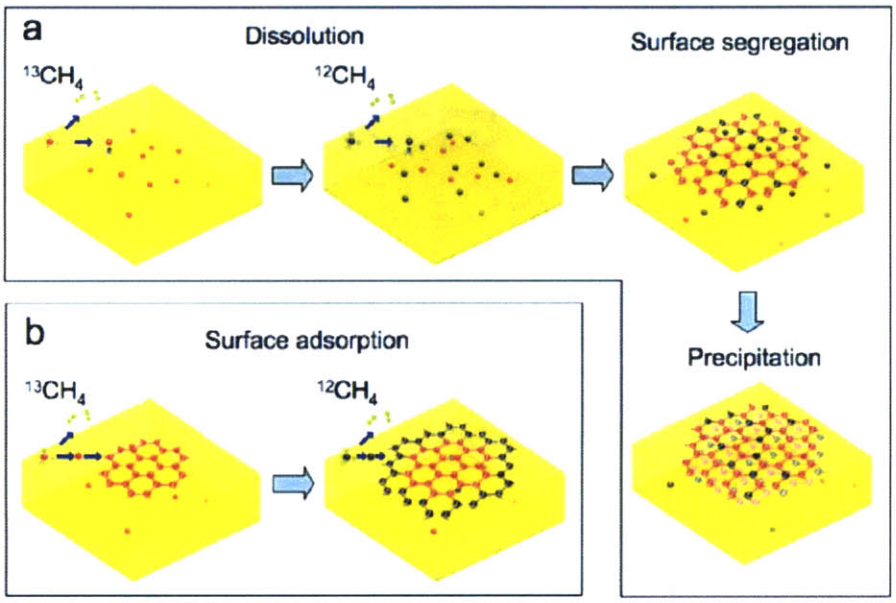

Figure 3-5: Graphene growth mechanisms.
Differentiation of the graphene growth mechanisms in Cu and Ni. Graphene grows on Cu by direct deposition from CVD. In Ni, graphene grows by precipitation after dissolution of carbon in the bulk. From ref. [62]

band frequency from of the graphene surface. The phonon frequency corresponding to the G band shifts due to the mass difference between the two carbon isotopes [62]. If the growth of graphene occurred due to the dissolution-precipitation model, it was expected that mixing of the carbon isotopes occurred in the bulk and the resulting graphene film would be formed of randomly distributed carbon isotopes. However, if the graphene film grew without dissolution of the carbon isotopes, it was expected that the switching between the two types of methane gases would be reflected in the spatial distribution of the carbon isotopes on the grown graphene film. Dissolution of carbon was observed in Ni (Figure 3-6) whereas no dissolution was observed in Cu during graphene growth (Figure 3-7).

The work presented in the next sections aims to address the possibility of using ambient pressures to grow graphene films and to transfer the films to other substrates. This is done with the intention to improve the scalability of graphene growth on transition metals and to use the material so produced on other substrates.

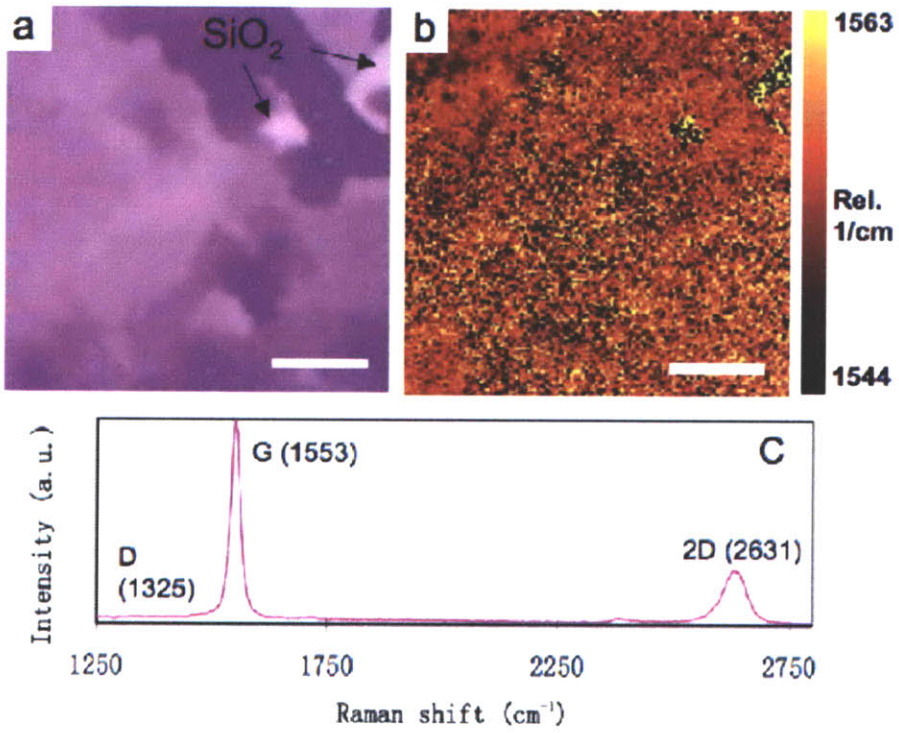

Figure 3-6: C^{12} and C^{13} distribution on graphene from Ni.
a) Optical image of the surface of a graphene film grown on Ni. b) Map of the G band frequency of the surface region in a). The G band frequency is homogeneous across the area mapped. This suggests a homogeneous distribution of carbon isotopes across the graphene film. c) Raman spectra obtained from a). From ref. [62]

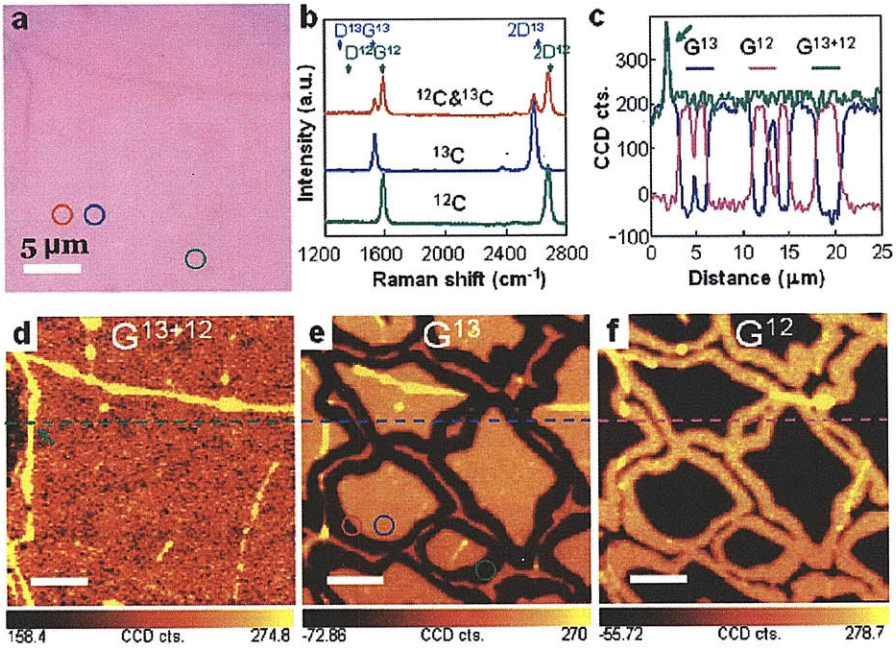

Figure 3-7: C^{12} and C^{13} distribution on graphene from Cu.
a) Optical image of the surface of a graphene film grown on Cu. b) Raman spectra from graphene composed of C^{13} (blue), C^{12} (green) and from the junction between C^{13} and C^{12} graphene (red). c) Raman intensities from the G band signal corresponding to C^{13} (G^{13}=1500-1560 cm^{-1}) , C^{12} (G^{12}=1560-1620 cm^{-1}) and both cases (G^{13+12}=1500-1620 cm^{-1}) across the line shown in d)-e). Integrated intensity maps of (d) G^{13+12}, (e) G^{13} and (f) G^{12} from the surface region shown in a). From ref. [62]

3.3 APCVD-enabled Carbon Segregation Process to Fabricate Few-layer Graphene Films

3.3.1 Description of the APCVD process

This section will begin by introducing the method utilized to fabricate graphene films in ambient pressure CVD (APCVD) via a carbon segregation mechanism. The approach also aims to create graphene films which can be transferred to non-specific substrates. The APCVD process will be discussed in the current section. The transferring of graphene films will be described in the following section 3.3.2.

The catalyst used is nickel in the form of thin films with thickness ranging from 200 to 500 nm. The thin films are deposited by e-beam evaporation or by sputtering of nickel. Although, most of the work is focused on studying graphene grown on thin films, some of the research presented in later chapters will include bulk Ni substrates. The nickel thin films are deposited over oxidized silicon substrates (SiO_2-Si) with 100 nm of silicon dioxide (Figure 3-8). Chapter 4 will discuss the effects of the Ni thin film deposition and its microstructure in the morphology of the graphene films. The CVD process involves three stages (Figure 3-9):

1. Annealing of the Ni film. Here, the catalyst film is annealed at temperatures between 900 and 1000 °C in order to induce its recrystallization. Figure 3-10 shows an SEM image of a nickel film annealed at 900 °C under Ar and H_2. The grain boundaries are visible only after the annealing step occurs. Increased grain sizes can help in avoiding excess nucleation sites for amorphous carbon or multilayer graphene (chapter 4). Furthermore, by annealing the Ni thin film, it is possible to induce a preferential texture of the film towards the (111) orientation. This is desired due to the lattice matching of graphene on the Ni(111) surface. This makes the precipitation of a monolayer of graphite more favorable over graphite precipitation during carbon segregation [47]. The Ni film microstructure and the growth of graphene on Ni(111) will be discussed in chapters 4 and 6. The annealing treatment is always done under a gas mixture of Ar (50-60% vol.) and H_2 (40-50% vol.).

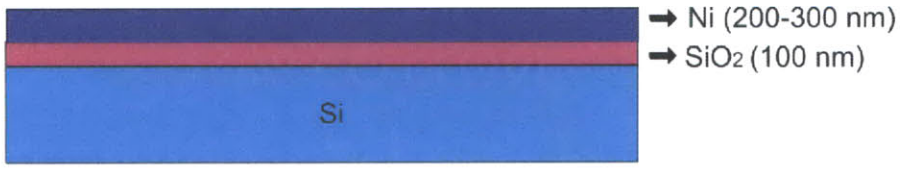

Figure 3-8: Cross-sectional view of deposited Ni films on SiO_2-Si substrates

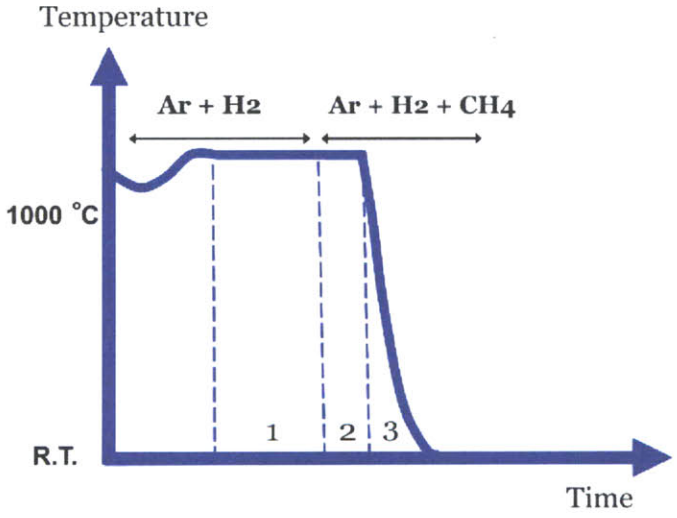

Figure 3-9: Temperature-time diagram for the APCVD process used to grow F-LG films.
1) Annealing of Ni thin films. 2) Exposure to methane. Carbon is produced on the surface of Ni and diffuses to the bulk to form a Ni-C solid solution. 3) Sample cooling. F-LG precipitates on the surface of the Ni film.

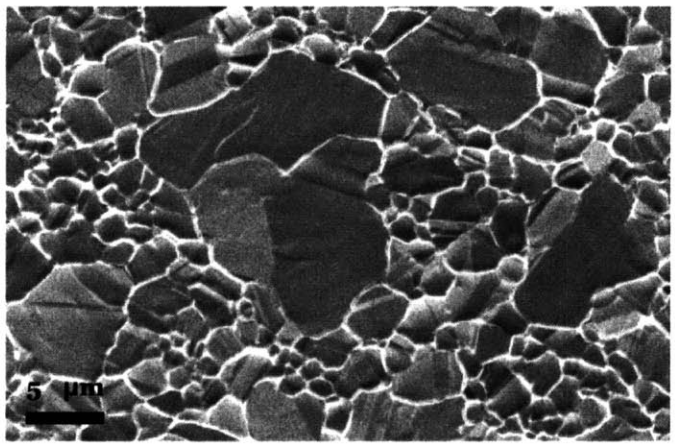

Figure 3-10: Ni film after annealing.
SEM image of the surface of a thin Ni film after annealing under Ar and H_2 at 900 °C for 20 minutes. The bright lines correspond to Ni grain boundaries.

2. Exposure to CH_4. After the annealing treatment, the Ni surface is exposed to diluted methane gas. The hydrocarbon gas is introduced with the same Ar and H_2 volume flow rates during the previous process. Typically, the temperature during this part of the process is the same as the annealing temperature. It is expected that methane is decomposed catalytically on the surface of Ni to produce carbon atoms on its surface. The decomposition of methane by transition metals has been studied extensively. The following reaction is used to describe the decomposition:

$$CH_4 \rightleftharpoons C(s) + 2H_2(g) \tag{3.1}$$

However, it is also thought that such decomposition may involve intermediate steps involving other hydrocarbons such as ethylene (C_2H_4) and acetylene (C_2H_2) [42]. Since this process occurs at temperatures around 900 and 1000 °C, it is expected that diffusion of the carbon to the bulk of the Ni film occurs. Previous experiments have suggested that amorphous carbon deposited on Ni will not diffuse into the bulk at

temperatures below 900 °C [45]. It is possible to estimate at which temperature to expect complete carbon diffusion into a Ni slab. The flux of impurities in a material is given by Fick's first law of diffusion:

$$\vec{J} = -D\frac{\partial c(x)}{\partial x}, \tag{3.2}$$

where D is the diffusivity of the impurities inside the host material and a function of temperature. The flux of atoms occurs as long as there is a concentration gradient of carbon atoms. Values for the diffusivity of carbon in Ni can be found in [63]. The time-dependent concentration profile of carbon inside the Ni film can be obtained from Fick's second law of diffusion:

$$\frac{\partial c(x,t)}{\partial t} = \frac{\partial \vec{J}(x)}{\partial x} = -D\frac{\partial^2 c(x)}{\partial^2 x}. \tag{3.3}$$

Assuming a constant concentration of carbon atoms always present on the Ni surface due to the decomposition of methane, and that there is no initial carbon inside the film (Figure 3-11(a)), the following boundary conditions for , apply:

$$c(t,0) = C_s \tag{3.4}$$

$$c(0,x) = 0, \tag{3.5}$$

where C_s is the surface concentration. At the Ni-SiO_2 interface ($x = l$):

$$\frac{\partial c(x,t)}{\partial x} = 0. \tag{3.6}$$

The solution for the concentration distribution of carbon atoms inside the Ni film is then described by:

$$\frac{c(x,t)}{C_s} = 1 - \frac{4}{\pi}\sum_{n=0}^{\infty}\frac{(-1)^n}{2n+1}exp(\frac{-D(2n+1)\pi^2 t}{4l^2})\cos(\frac{(2n+1)\pi(x-l)}{2l}). \tag{3.7}$$

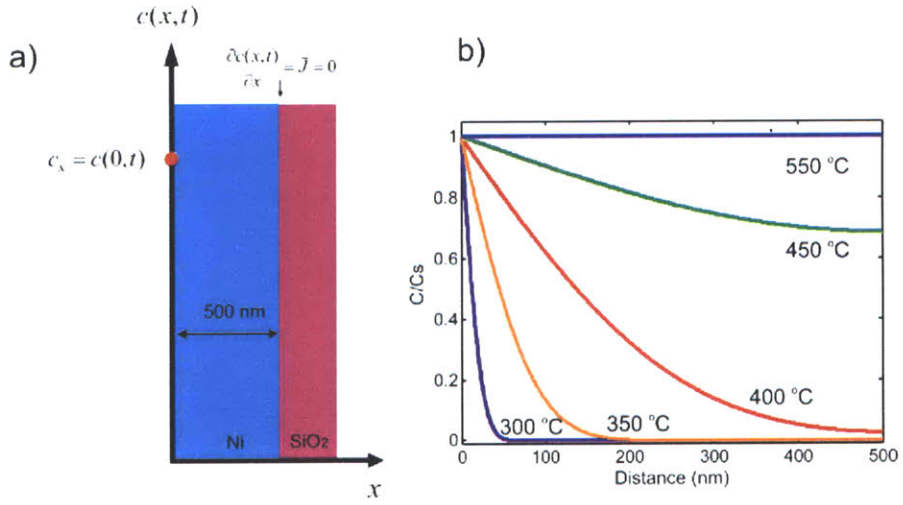

Figure 3-11: Diffusion of carbon in a Ni thin film
a) Diffusion model for a constant surface concentration of carbon at the top surface of a Ni thin film. Null flux of carbon is assumed for the Ni-SiO_2 interface. b) Carbon concentration distributions inside a 500 nm film for various temperatures and after 5 minutes of diffusion. Equilibrium with the surface is reached close to 550 °C. Solutions are taken from equation 3.7

Figure 3-11(b) shows the carbon concentration inside a 500 nm Ni film for various temperatures after diffusing for five minutes (typical time for the CVD process described). The concentration is normalized to the surface concentration C_s. From this simple model, it is expected that above 550 °C the bulk of the Ni reaches the same concentration of carbon impurities as that of the surface. This is as long as the concentrations involved are below the Ni carbon solubility at the given temperatures. Therefore, it is expected that within the temperature range of the CVD process (900-1000 °C), diffusion of carbon to the Ni bulk will always occur. Saturation of the nickel film is not expected during this stage of the processing. This is due to the dilution of methane gas during our conditions (0.1-1% vol.) and experimental observations that suggest that graphene forms only during the cooling of the sample (chapter 5). The thickness uniformity of the F-LG film depends strongly on the cooling rate.

3. Cooling of the Ni film. Segregation of the carbon stored inside the nickel film is promoted by cooling the nickel sample. The carbon segregated to the surface initiates the growth of single- and few-layer graphene. Average cooling rates between 4 and100

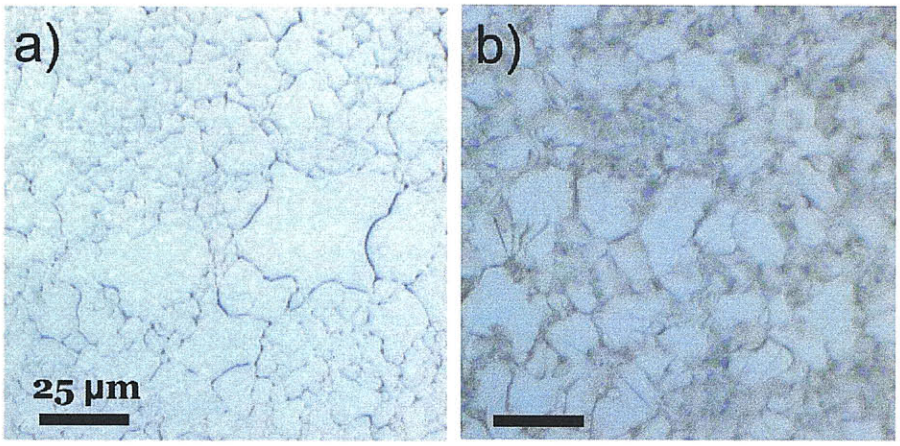

Figure 3-12: F-LG on Ni.
a) Optical image of a clean Ni film which was annealed. b) Optical image of a Ni film after graphene growth.

°C min^{-1} are utilized. The methane partial pressure is left constant during this stage and the same as in the previous stage. It was realized that this was necessary in order to avoid the methanation of carbon species during cooling on the Ni surface. Nickel can not only catalyze the dehydrogenation of hydrocarbons but can also induce the formation of methane in the presence of carbon and hydrogen [64]. Cooling down under the absence of hydrogen (only Ar) was problematic due to destruction of the nickel thin film during prolonged cooling. The effect of the cooling rate on the film morphology, thickness uniformity and properties will be addressed in chapter 5.

Figure 3-12 compares a clean Ni film which was only annealed and a Ni film after the three process steps described above. The dark features suggest the precipitation of F-LG and graphite. Their nucleation distribution depends on the grain size of the initial Ni film and this will be discussed in more detail in the next chapter. The clear regions contain 1-LG or 2-LG and these tend to be away from the grain boundaries of the Ni film. They can only be detected optically once the graphene film has been isolated from the Ni and transferred to a SiO_2-Si substrate (discussed in the next section).

Inspection by AFM shows the formation of "wrinkles" on the surface (Figure 3-13). These are usually seen on graphite and FLG films grown over various substrates

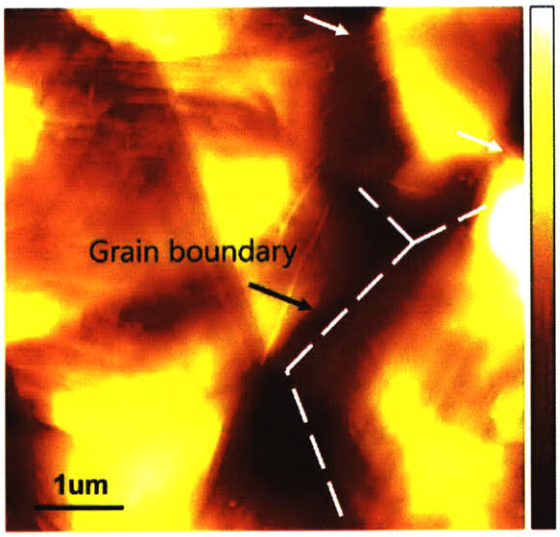

Figure 3-13: AFM image of a graphene film on a polycrystalline Ni thin film. The ripples (pointed out by white arrows) at the edge of the groove indicate that the film growth bridges across the gaps between grains.

including transition metals and SiC [55, 33]. These ridges have been a subject of study previously and their formation is usually attributed to the difference in the thermal expansion coefficient (TEC) between Ni and graphite [55, 65]. The difference in thermal expansion coefficient between 1000°C and 25°C for Ni is 21×10^{-6} K^{-1} to 13×10^{-6} K^{-1} [66], whereas for graphite it is from -1.2×10^{-6} K^{-1} to $0.7\times10^{-6}K^{-1}$ [67]. Ni contracts during cooling and graphite expands (negative TEC), therefore, inducing stress on the assembly of both films: that is, a tensile stress on Ni and a compressive one for graphite. The release of such stress is expected to induce formation of the ridges in order to compensate for the extra length existing for the graphite film [55, 68]. Therefore, the wrinkles observed in the AFM characterization are assigned to the F-LG film formed on the Ni thin film. These wrinkles usually extend across the grain boundaries identified in the AFM images. This is suggestive of the formation of a F-LG film which extends continuously across the grain boundaries of the Ni film.

The formation of a graphite-based film over Ni is confirmed by X-ray photoemission spectroscopy (XPS). Figure 3-14 shows the C1s peak taken from the surface of a Ni thin film after the CVD process. This peak corresponds to 1s electrons of carbon

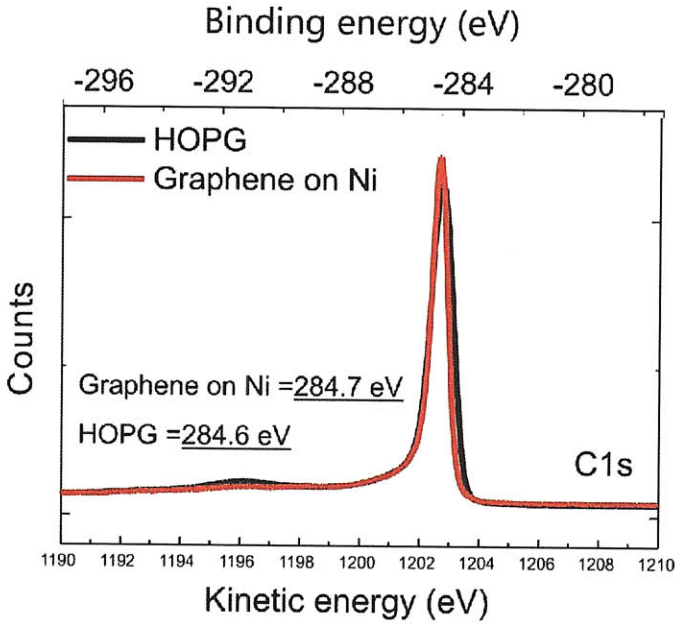

Figure 3-14: XPS spectra showing the C1s (284.7 eV) peak from the Ni surface. The C1s peak (284.6 eV) measured from an HOPG sample is shown as reference. Measurement by R. Koch at Technische Universitt Ilmenau, Germany.

atoms bonded in the sp^2 configuration. The C1s signal measured on the Ni surface is compared to that obtained from an HOPG sample. The shift towards higher C1s energy for the F-LG on Ni is explained by the thin nature of the film [69].

Transferring of F-LG films from their growth substrate is benefitial for further characterization of film thickness, transparency, structure and electrical properties. Furthermore, this would be desired if such materials are intended to be used on other substrates. In the following section, a process to accomplish such a transfer is described.

3.3.2 Transferring of Few-layer Graphene Films to other substrates

The isolation of the graphene films from the growth substrate relies on the chemical etching of the Ni film. This is done using a wet-etch process and there are different variations of how this can be done. One example is represented in Figure 3-15. Before

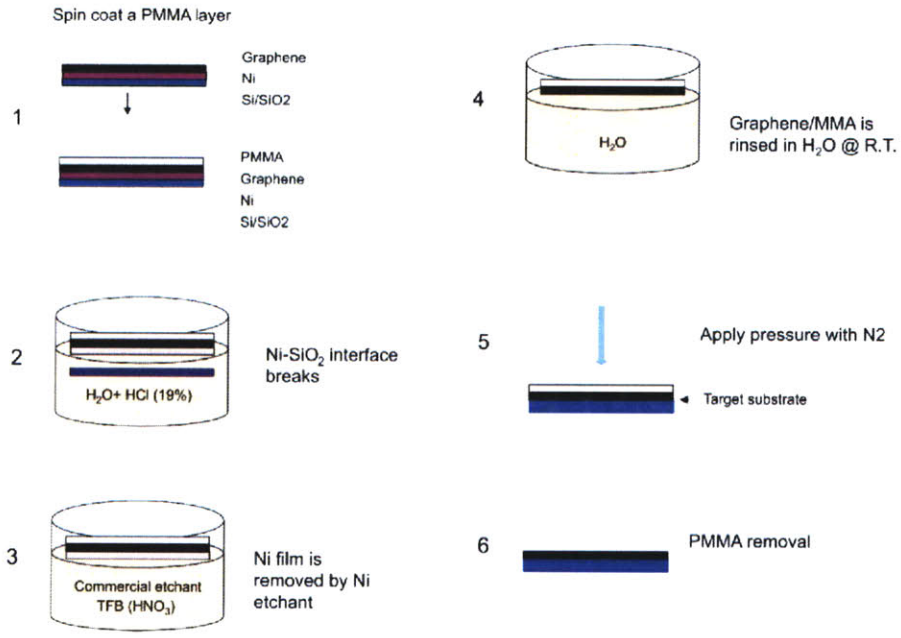

Figure 3-15: Steps involved in the isolation of the FLG films from Ni and their transfer to other substrates.

the etching of the Ni thin film, a support layer is adhered to the graphene side of the samples. The purpose of this layer is to give mechanical support to the graphene layer for handling after etching the Ni film. One requirement for this layer is that it is possible to remove it after the graphene film is transferred to another substrate. Most of the time this layer is poly(methyl methacrylate) (PMMA) and it has been used for similar purposes in the transfer of carbon nanotubes between different substrates [70]. PMMA is widely used as a positive ebeam resist in lithography and is dissolved by acetone. The PMMA layer is deposited on the graphene surface by spin-coating (3,000 rpm for 1 min.) a solution of such polymer (Microchem, 950,000 molecular weight, 9% in anisole). The polymer solution forms a thin PMMA film on the graphene surface with a thickness estimated to be around 1.5 μm under the spin-coating conditions listed in the appendix. The sample with the PMMA film is baked in order to evaporate the solvent contained in the PMMA film. This step helps in the hardening of the PMMA layer, thereby giving it mechanical stability.

After deposition of the support layer, the Ni thin film is detached from the SiO_2-Si

substrate at the Ni-SiO_2 interface. This is can be done by laying the whole substrate on an aqueous hydrochloric acid (HCl) solution. While the sample is suspended over the acid-air interface, the acid etches some of the Ni in contact with the SiO_2, releasing the Ni-graphene-PMMA assembly from the SiO_2/Si substrates. This typically occurs within 5 minutes after the sample is laid on the acid solution. After this, the released stack is transferred to water to rinse away any HCl residues. In the next step, the Ni-graphene-PMMA film is laid on top of a commercial Ni etchant which contains nitric acid (HNO_3). Here, the Ni side of the stack is put in direct contact with the etchant to maximize the etching rate. After etching of the Ni film, the graphene-PMMA membrane is suspended over deionized water in order to rinse any residues from the previous steps. The membrane can be handled with conventional tweezers and laid on top of the target substrate (graphene side contacting the surface). Conformation and adhesion of the graphene side to the new surface is induced by applying N_2 air pressure perpendicular to the surface of the membrane (PMMA side). Water from the previous step which is trapped between the graphene side and the substrate is driven towards the edges of the membrane and finally to the outside where it is dried. After 1 minute of this procedure, the graphene adheres to the target substrate fixing the position of the graphene-PMMA membrane on the substrate. Lastly, the PMMA is removed by exposing it to acetone vapor or to an Ar and H_2 gas mixture at elevated temperatures (450 °C).

Following the isolation of the films from the Ni growth substrate, it is possible to perform additional characterization of the films fabricated. In the next subsection preliminary characterization of the F-LG films produced is presented. This is aimed towards a determination of film thickness and morphology. Furthermore, this step also confirms carbon is mainly in sp^2 hybridization.

3.3.3 Preliminary characterization of single- and few-layer graphene films isolated from Ni

Film features are revealed by optical images when the films are on Si substrates with a 300 nm oxide layer (Figure 3-16). Variations in the film thickness are indicated by the change of color contrast in the optical images. This is due to light interference on the SiO_2 layer which is modulated by the number of graphene layers [11, 12]. The differences in thickness range from a monolayer to a few graphene layers. The lightest pink regions in the optical images (Figure 3-16(a)) have a thickness of roughly 1 nm, as measured by AFM (Figure 3-16(b-c)), which typically corresponds to a monolayer or bilayer of graphene. Purple regions correspond to 3.0 nm thickness (Figure 3-16(b)). Height measurements extracted from a series of AFM images along the film edge are shown in the inset of Figure 3-16(c). This figure shows that the thickness ranges from 1 to 5 nm corresponding to approximately 1-12 graphene layers. The average height measured is 2.8nm$\pm$0.3 corresponding to 6-7 graphene layers. By comparing optical images of as-grown graphene films on the Ni surface and their images after being transferred to SiO_2-Si (Figure 3-17), it is observed that the morphologies of the graphene film correlate qualitatively with the microstructure of the Ni films. This is due to the fact that regions with multilayer graphene precipitate preferentially at the grain boundaries. This will be further discussed in the next two chapters.

The APCVD grown films can be transferred by the same method to TEM lacey carbon coated grids (Figure 3-18(a)). TEM examination confirms that changes in film thickness correspond to only a few graphene layers. The edges of the suspended film always fold back, allowing for a cross-sectional view of the film. The observation of these edges by TEM provides an accurate way to measure the number of layers at multiple locations on the film (Figure 3-18(b-e)). Typically, sections of 1-8 layers are observed, in close agreement with the AFM data. Selective area electron diffraction (SAED) on the graphene film (inset of Figure 3-18(a)) reveals a hexagonal pattern confirming the three-fold symmetry of the arrangement of carbon atoms. When different regions of the film are inspected, well-defined diffraction spots (instead of

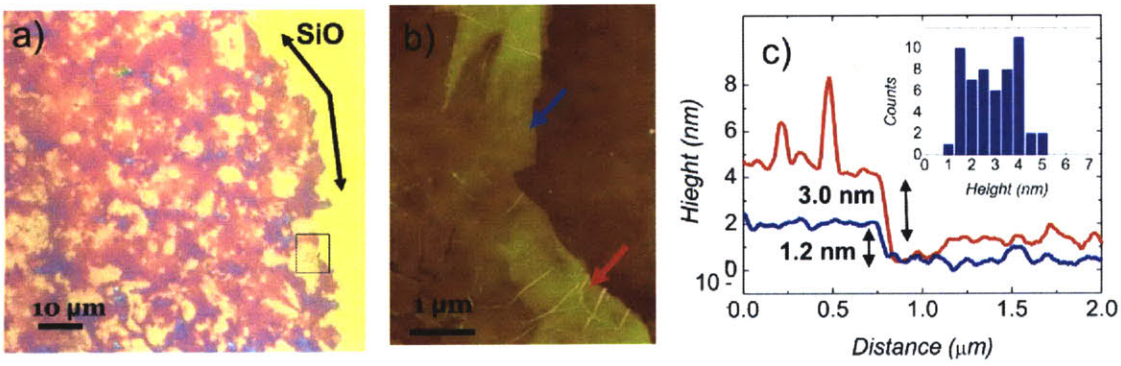

Figure 3-16: Thickness of the F-LG films as measured by AFM.
a)An optical image of an edge of a graphene film on a SiO_2-Si substrate. b)An AFM image of the region enclosed by the black square in a). The blue (red) arrow corresponds to the pink (purple) regions in the black square in a). c) Height measurements on the two positions indicated in b). The blue (red) curve corresponds to the region identified by the blue (red) arrow in b). The height distribution, measured from AFM images taken along the film edge in a), is shown as an inset.

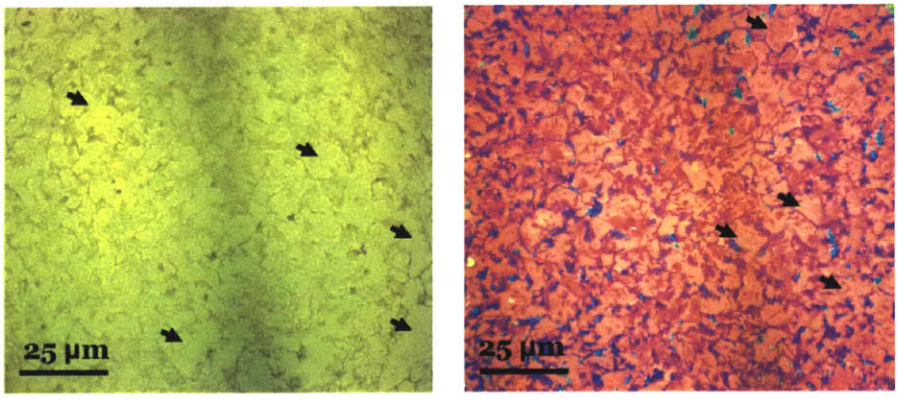

Figure 3-17: Optical images of F-LG films.
a) F-LG film on Ni. b) F-LG film after being transferred to a SiO_2-Si substrate.

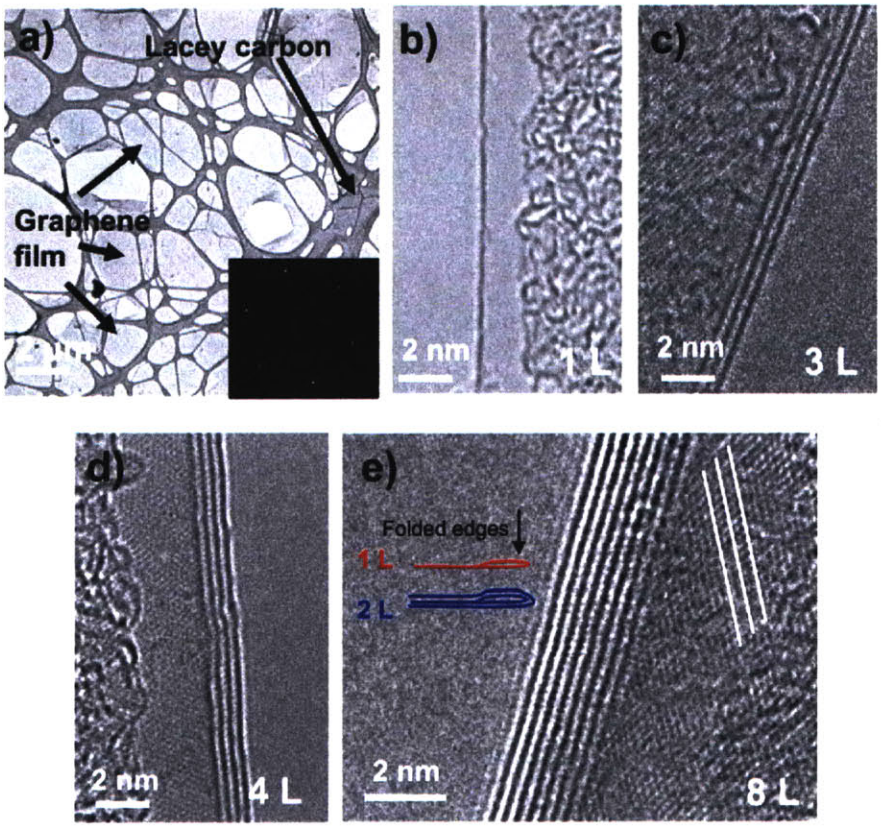

Figure 3-18: TEM of graphene and F-LG grown on Ni.
a) Low-magnification TEM image showing an APCVD-grown graphene film on a lacey carbon-coated grid. Electron diffraction on the graphene film is shown as an inset. b-e) High magnification TEM images showing the edges of film regions consisting of one b), three c), four d), and eight e) graphene layers. The cross-sectional view is enabled by the folding of the film edge as shown in e).

ring patterns) are always observed, indicating the crystallinity of all regions examined.

Figure 3-19 compares the Raman spectra of 1, 2 and 3 graphene layers derived from APCVD and HOPG (both types of materials on SiO_2-Si substrates). The G peak occurring around 1580 cm^{-1} corresponds to the stretching of C-C bonds [71, 72]. The D peak at 1350 cm^{-1} is due to disorder, symmetry-breaking effects [73]. The presence of a D band peak suggests the existence of grain boundaries or point defects. It also confirms the presence of sp^2 carbon [73] in agreement with XPS characterization. Spectra from the thinnest sections of the CVD graphene film, estimated to be 1-2 LG, show a sharp linewidth ($\approx$30 cm^{-1}) and a single Lorentzian profile of the G' band.

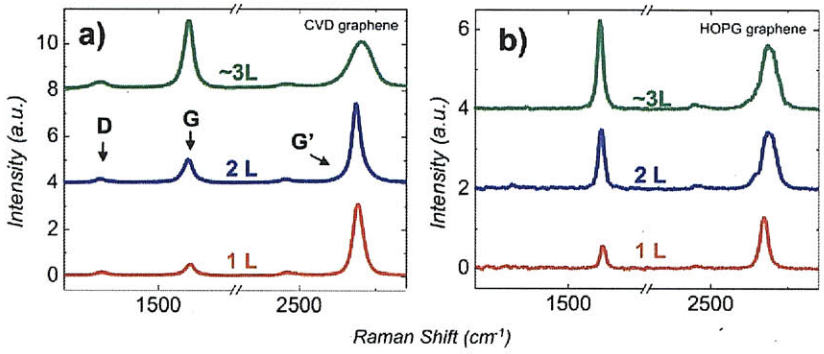

Figure 3-19: Raman spectroscopy of CVD-grown graphene films on SiO_2-Si. a) Raman spectra of 1 (red), 2 (blue), and ≈3 (green) graphene layers from an APCVD graphene film. (b) Raman spectra of 1 (red), 2 (blue), and 3 (green) graphene layers derived by the micromechanical cleaving of HOPG for comparison. The excitation wavelength is 532 nm.

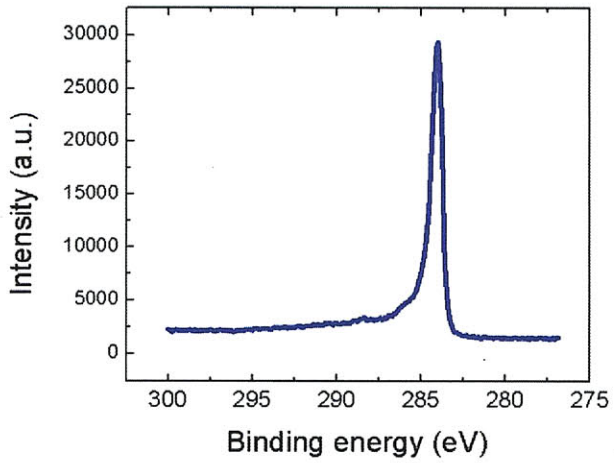

Figure 3-20: XPS spectra of the C1s region for a F-LG film transferred to SiO_2-Si. The C1s peak was measured to be 284 eV, in good agreement with the expected energy for the 1s electrons in the sp^2 carbon configuration.

These are characteristic of monolayer graphene [74]. The G' lineshape provides a good measure of the layer number in the case of HOPG-derived graphene. For graphene produced by APCVD, this is not the case. Sections of ≈2-3 LG regions very often show linewidths of ≈30 cm^{-1} and Lorentzian lineshapes. It is also observed that for regions with more than 3 graphene layers, there is a variation in the G' lineshape between sections with the same layer number. Determination of the number of layers in the CVD films will be discussed in more detail in chapter 5.

Lastly, XPS measurements confirm the existence of sp^2 bonded carbon on the films transferred to a secondary substrate. Figure 3-20 shows the C1s signal of one of the films after being deposited to a SiO_2-Si substrate. The position of the peak is shown at 284.05 eV in close agreement with the C1s peak for graphite (284.3 eV). The absence of strong deformations of the C1s peak shape compared to that taken before transferring (Figure 3-14) is an indication that the chemical structure of the film is on average preserved.

3.4 Summary

In this chapter, the fabrication of graphite and graphene using carbon segregation and CVD was discussed. A method to grow F-LG films on thin Ni films was presented. The process is enabled by APCVD using methane as the hydrocarbon source and the F-LG film grows via a carbon segregation mechanism. Such films can be isolated from the growth substrate by wet-etching the Ni and transferred to a variety of substrates. SiO_2-Si substrates were used as an example. The average thickness of the films is around 3.0 nm, as judged by AFM. Regions with a thickness estimated of 1-LG or 2-LG range from a few microns, to a few tens of microns as observed by optical microscopy. TEM images confirm the existence of regions between 1-8 layers in thickness, confirming the previous observations. Finally, electron diffraction, Raman spectroscopy and XPS analysis confirm the existence of a graphitic structure and the presence of sp^2 carbon in the films produced. In the following chapters, the effect of the Ni film properties and the cooling rate of the APCVD process will be discussed.

Chapter 4

Effect of the Ni Thin Film Microstructure

The use of Ni films with a few hundreds of nanometers in thickness for the growth and transfer of graphene is advantageous since these films are readily accessible and their thin thickness simplifies the transferring process. In the previous chapter, it was mentioned that the thickness uniformity across the F-LG films is influenced by the Ni grain size. Specifically, it is observed that the thinnest regions of the films, consisting of 1-LG and 2-LG, grow predominantly on top of the interior surface of the Ni grains away from the boundaries. Figure 4-1 shows the region of a film before (graphene on Ni) and after transferring (graphene on SiO_2-Si). The shape and area of regions with 1-LG or 2-LG correlate with the shape of the Ni grains (see appendix for an estimation of the number of layers). Ni thin films deposited on amorphous substrates (SiO_2 in the present case) are usually polycrystalline. They undergo grain growth at the temperatures of the CVD process. In order to control the morphology of the graphene films, it is necessary to control the morphology of the Ni grains. The next section focuses on the basis of grain growth. In the second part of this chapter, the effect of Ni grains on the grown F-LG films is discussed.

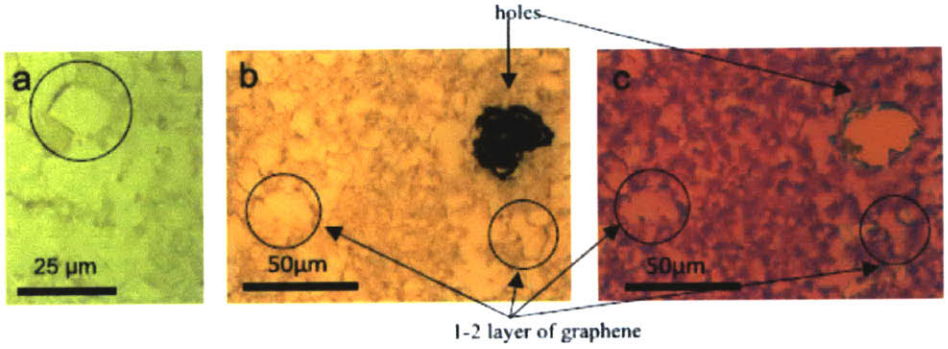

Figure 4-1: Comparison between the shapes of graphene regions with equal thickness and Ni grains.
a)Optical image of a Ni thin film after CVD. A Ni grain is circled. Thicker graphite (darker in the image) forms preferentially at the grain boundaries. Optical images of a F-LG film at the same location before (b) and after transferring to a SiO_2 substrate (c). The shape of regions with a constant number of layers in (c) (circled) follows the shape of the Ni grains in (b) (also circled).

4.1 Grain growth

4.1.1 Ideal grain growth in bulk materials

For the current purpose, a bulk system is one for which all dimensions are large compared to the average grain size. In these systems, grain growth is observed to behave according to the following relationship [75]:

$$\overline{D}^m - \overline{D}_o^m = t\alpha_o exp\left(\frac{-Q}{kT}\right), \tag{4.1}$$

where $\overline{D}$ and $\overline{D}_o$ are the average grain radius after a time t and the initial grain radius, respectively. The exponent m is usually expected to have a value of 2 [75]. The term α_o is a constant, Q is the activation energy for grain boundary motion, k is the Boltzmann constant and T the temperature.

This behavior in 8.1 is explained with a model in which the growth rate is proportional to the average boundary energy per unit volume, E [75]:

$$\frac{d\overline{D}}{dt} = ME, \tag{4.2}$$

where E is given by:

$$E = \beta \frac{\overline{\gamma}_{gb}}{\overline{D}} \tag{4.3}$$

and β is a geometric constant and $\overline{\gamma}_{gb}$ is the average grain boundary energy per unit area. The proportionality between the rate and average boundary energy is given by M, the temperature dependent mobility of grain boundary motion:

$$M = M_o exp\left(\frac{-Q}{kT}\right). \tag{4.4}$$

This description is usually referred to as normal grain growth. Its driving force is the minimization of interface energy at grain boundaries. In the following section, the description of grain growth of thin films will be discussed.

4.1.2 Grain Growth in Thin Films

The grain growth in metallic thin films has been studied before by Thompson et al. [75, 76, 77]. Normal grain growth as described above occurs in thin films, for which the average grain diameter is smaller than the film thickness [78]. Experimental evidence shows that once this growth results in an average grain size that is similar to the film thickness, growth slows down and finally stops [78]. Therefore there is a film thickness dependence on the final grain size after grain growth and this is also observed in our Ni films (discussion below). Typically, the grain structure of the film forms a columnar structure at this point(Figure 4-2). The final distribution of grain sizes usually follows a lognormal function [79]. The original assumption of the growth driving force should still hold at this stage because of boundary energy minimization. Therefore, it is necessary to account for other factors in the description of grain growth in thin films. The decrease in growth rate can be explained by factors such as the pinning of grain boundaries due to the formation of a thermal groove between them [80].

Mullins [80] proposed an explanation for the observed phenomenon of maximum grain size as a function of film thickness. First, let's consider a microstructure com-

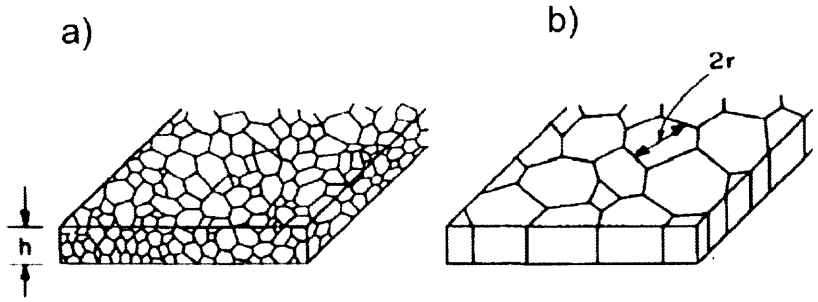

Figure 4-2: Schematic of the grains in a thin film during grain growth.
At the initial stages of grain growth (a) and after the formation of a columnar grain structure (b). From ref [75]

posed of grains in which the sides of each grain has a finite curvature (Figure 4-3(a)). The grain sides can therefore be thought of as arcs of circles (Figure 4-3(a)). Assuming that the equilibrium shape of a grain boundary is defined by minimizing its surface area, the interior of a boundary would adopt a catenoid shape. This is shown in the cross sectional view of grain boundaries in Figure 4-3(b). A catenoid shape is defined in cartesian coordinates as:

$$x = c\cosh(\frac{v}{c})\cos(u) \quad y = c\cosh(\frac{v}{c})\sin(u) \quad z = cv, \tag{4.5}$$

and in cylindrical coordinates as:

$$r = c\cosh(\frac{z}{c}). \tag{4.6}$$

With this shape, the mean curvature K also vanishes at all points of the boundary surface. The in-plane curvature balances the out-of-plane curvature. This is another equilibrium condition for the grain boundary using the Gibbs-Thompson treatment of the driving force of boundary movement which relates curvature to vapor pressure (p) and chemical potential(μ):

$$p = K\gamma_{gb} \tag{4.7}$$

where p is the vapor pressure, K the local curvature and γ_{gb} the boundary energy.

With these considerations, the angle θ (measured with respect to the surface normal) at which a grain boundary meets the surface depends solely on the ratio of the film thickness a to the radius of curvature r:

$$\theta = \frac{a}{2r}. \tag{4.8}$$

Furthermore, it is known that a groove is formed due to surface tension at the intersection of a grain boundary and the free surface. An ideal grain boundary groove is shown in Figure 4-3(c). The dashed line lies perpendicular to the surface and the rest of the lines stemming from the notch denote possible configurations of a grain boundary. Possible boundaries are denoted by the black solid lines and they intersect the free surfaces at an angle given by the above expression (equation 4.8). In order for a grain to grow, it is necessary to move the boundary with respect to the groove. There there is a critical angle θ_o below which a grain boundary will require an increase in its length and area in order to move. This is not the case when the grain boundary intersects the surface normal at an angle larger than θ_o, therefore, allowing the boundary to escape the anchoring.

If the angle of grain boundary intersection is $\theta = \frac{a}{2r} \leq \theta_o$, then all boundaries will be permanently stuck in their thermal grooves. On the other hand, if $\theta = \frac{a}{2r} \geq \theta_o$, the boundary can escape the anchoring from the groove. If it is assumed that the surface traces of the grains of the polycrystalline films used in this work can be approximate by circular arcs [79], the radius of curvature for a given grain is related to the grain diameter by $r \approx D/\sigma$ [79, 80] (where σ is a constant). Therefore, when the grain size in a thin film becomes large enough so that all boundaries have radii of curvature that exceed $\frac{a}{2\theta_o}$, grain growth must stop. From the above considerations, the maximum grain diameter is estimated by [80]:

$$\overline{D}_{max} = \frac{\overline{r}_{max}}{\sigma} \approx \frac{a}{2\theta_c\sigma} = \frac{3\gamma_s}{\sigma\gamma_{gb}}a, \tag{4.9}$$

where σ is a constant. Furthermore, the grain growth slows down as the grain size approaches its maximum [81]. This is usually expressed as a *drag* term in the growth

rate equations. Equation 8.2 then becomes:

$$\frac{d\overline{D}}{dt} = \beta\overline{\gamma}_{gb}M_o exp\left(\frac{-Q}{kT}\right)\left(\frac{1}{\overline{D}} - f\right), \tag{4.10}$$

where f is usually:

$$f \propto \frac{1}{\overline{D}_{max}}. \tag{4.11}$$

Figure 4-4 shows optical images of the surface of Ni films with thickness between 200-500 nm and annealed at 1000 °C for 20 minutes under Ar and H_2. This temperature will be used since most of the F-LG growth processes occurred at this temperature. As expected, the grain size $\overline{D}$ increases with increasing Ni thickness for the same annealing conditions (Figure 4-5(a)). The mean growth rate of the grains also depends on the Ni film thickness (slope in Figure 4-5(b)). Furthermore, the existence of a bimodal distribution of grain sizes is noticed from the optical images and size distributions as a function of annealing time (Figure 4-6). To explain this, it is necessary to invoke the role of surface energy minimization besides that of boundary energy minimization. A bimodal distribution arises from the preferential growth of a subpopulation of grains due to the anisotropy of the free surface energies [75]. The preferential growth of some grains is referred to as a secondary or an abnormal grain growth. The change in energy per unit volume due to surface and interface energy change in grain growth is determined by:

$$\Delta F_{\frac{s}{i}} = \frac{\Delta\overline{\gamma}}{a}, \tag{4.12}$$

where

$$\Delta\overline{\gamma} = [\overline{\gamma}_s - (\overline{\gamma}_s)_o] - [\overline{\gamma}_i - (\overline{\gamma}_i)_o] \tag{4.13}$$

, and $\overline{\gamma}$, $(\overline{\gamma})_o$ and a are the final, initial average energies and film thickness, respectively. Because the change in surface energy scales with thickness, it becomes an important factor governing grain growth in thin films(eq. 8.5). Abnormal growth can

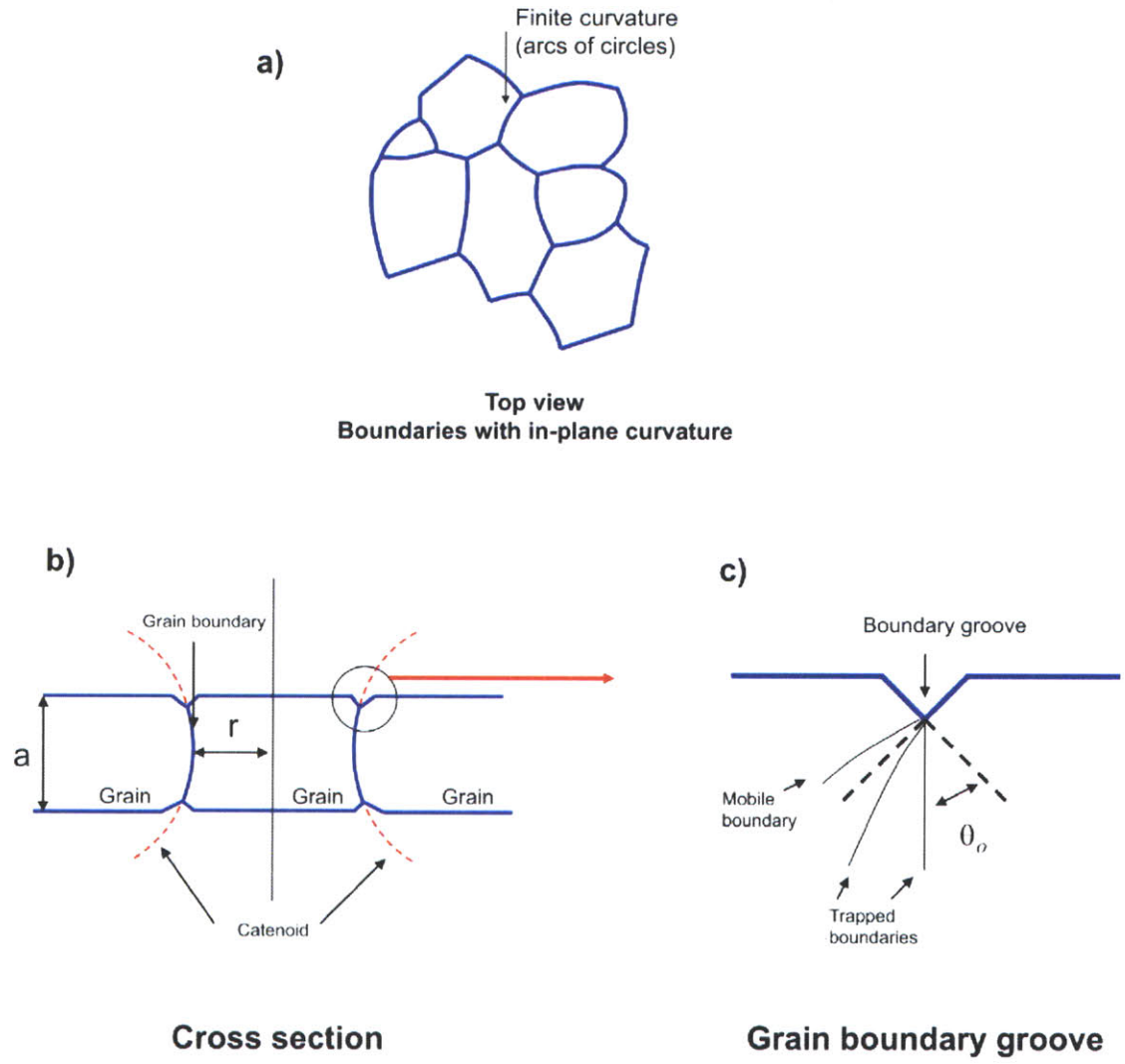

Figure 4-3: Pinning of grain boundaries by boundary grooves.
a) Top view of a collection of grains. The sides of the grains are assumed to have finite in-plane curvature they can be thought of as arcs of circles. b) Representation of the cross section of a film composed of columnar grains and grain boundaries spanning the thickness of the film. The interior of the grains will adopt a catenoid shape (red, dashed curve) in order to minimize the interface surface. With the catenoid shape, the curvature at every point on the boundary surface equals zero. The in plane and out of plane curvature at each point of the catenoid will have an equal magnitude but opposite sign [80]. c) Idealization of a grain boundary groove. If the grain boundary makes an angle greater than θ_o with the surface normal, the boundary can move and escape the anchoring of the groove. Otherwise, it should be remain pinned by the groove.

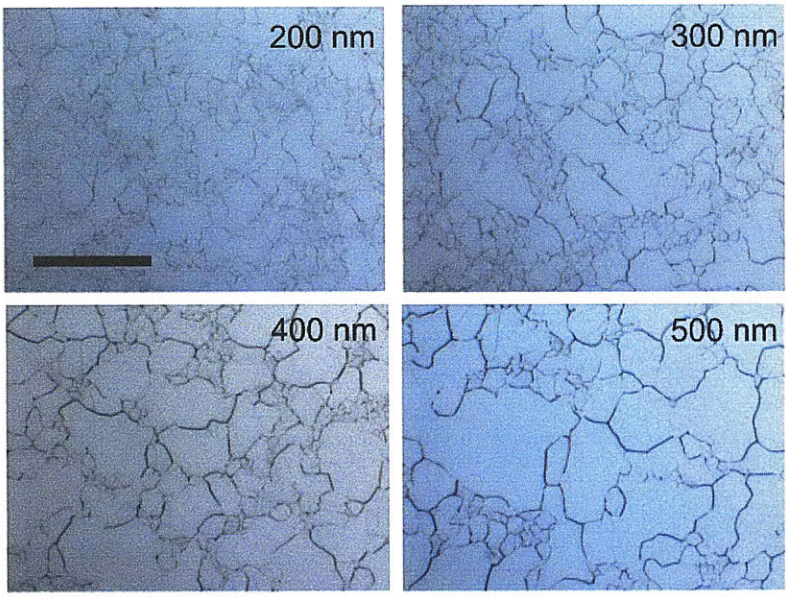

Figure 4-4: Optical images of Ni thin films after being annealed in H_2 and Ar at 1000 ^oC for 20 minutes. Scale bar is 20 μm.

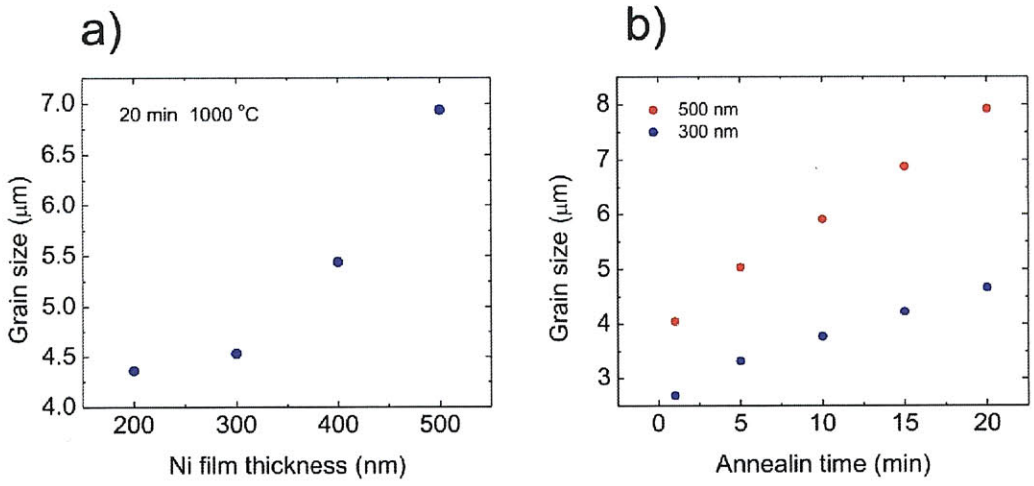

Figure 4-5: Average grain size as a function of film thickness and annealing time. a) Average grain size as a function of the Ni film thickness. b) Average grain size as a function of annealing time for 500 nm and 300 nm Ni films. The grain size increases with the film thickness and annealing time. As observed from b), the grain growth is constant and does not stagnate during the annealing times used.

cause bimodal grain size distributions in two ways. First, the growth rate of abnormal grains could be higher than that of normal grains. Second, abnormal growth could proceed even after the stagnation which Mullins proposed [75] for normal growth. This is the case when macroscopic energetic arguments are considered rather than only those involving the grain boundaries [75, 77]. Under the above considerations, the growth rate of secondary grains can be described by:

$$\frac{dD_s}{dt} = M\left[2\frac{(\overline{\gamma_s} - \gamma s)}{a} + \overline{\gamma}_{gb}\left(\frac{1}{\overline{D_n}} - \frac{1}{D_s}\right)\right], \tag{4.14}$$

where $\overline{\gamma_s}$ is the average surface energy of the system, D_s is the diameter of the secondary grain, and $\overline{D_n}$ is the mean diameter of normal grains. The growth rate of secondary grains is expected to be higher than the rest of the grains due to the addition of surface energy terms in the growth equation. In fcc metals like nickel, the (111) orientation is the closest packed face and therefore one with the lowest surface energy [77]. Therefore, the largest grains observed in Figure 4-4, with dimensions greater than the film thickness, are assumed to result from abnormal grain growth and to have a (111) surface orientation. XRD data (Figure 4-7) of the Ni thin films before and after annealing suggests the texturing towards the (111) orientation as expected. This is relevant since the growth of single layer graphene is energetically favorable on Ni(111) during the segregation of carbon atoms (see chapter 6).

Typically, grain growth in free standing thin films or thin films deposited on amorphous substrates leads to a preferential texture of the film. However, grains developed with the preferred surface orientation will have a random in-plane orientation (Figure 4-8(a)). For films deposited on single crystal substrates, the interface energy γ_i will also play a role in the system's energy minimization. In such a case, it is expected that the film will develop a particular in-plane orientation as well, that is, epitaxial to the underlying substrate (Figure 4-8(b)). Since the films used in this work were deposited on amorphous SiO_2 it is expected that the (111) grains have random in plane orientations.

The above discussion explains the grain structure observed for the Ni films used in

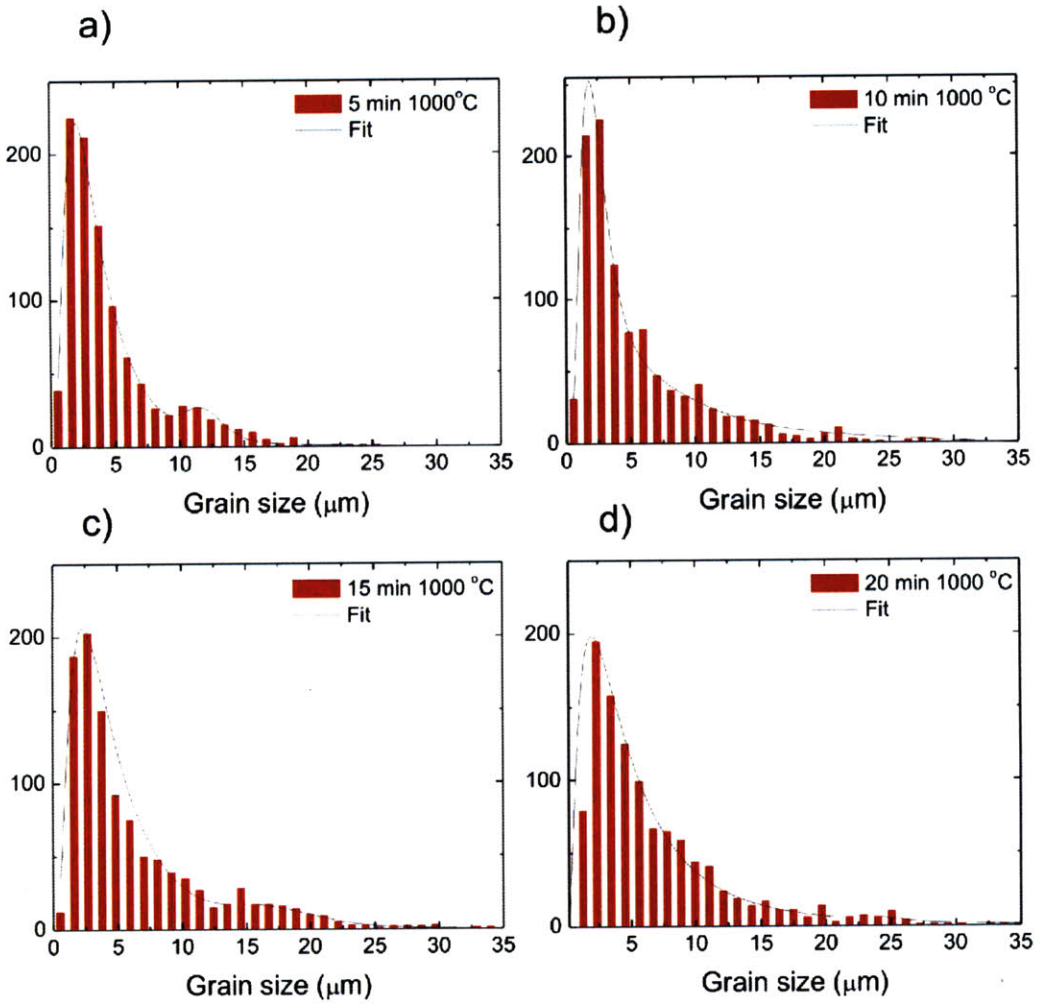

Figure 4-6: Grain size distributions as a function of annealing time.
Grain size distributions of the microstructure obtained with 300 nm after being annealed with H_2 and Ar at 1000 °C for 1 to 20 minutes. The distribution widens with annealing time due to grain growth. The data also reflects bimodal distributions for intermediate times. This is seen more clearly for data for the 5 and 15 minutes annealing times. A subset of grains grows larger grain sizes than the rest in order to minimize the film surface energy. For the longest annealing times, only one lognormal distribution is expected due to the homogenization of grain sizes. Fits of the distribution are made with two lognormal functions.

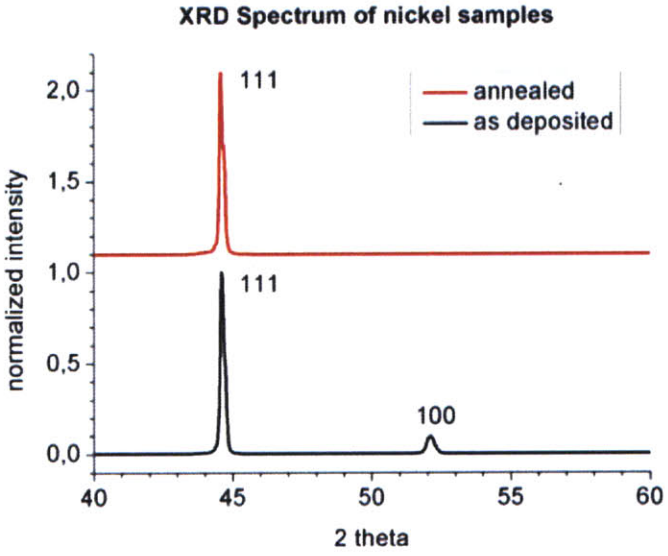

Figure 4-7: XRD peaks of 500 nm Ni films before and after annealing. The increase in the diffraction peak from (111) planes and the attenuation of that from (100) planes suggests the film texturing in the (111) orientations. This is in agreement with a grain growth process which is driven by surface energy minimization.

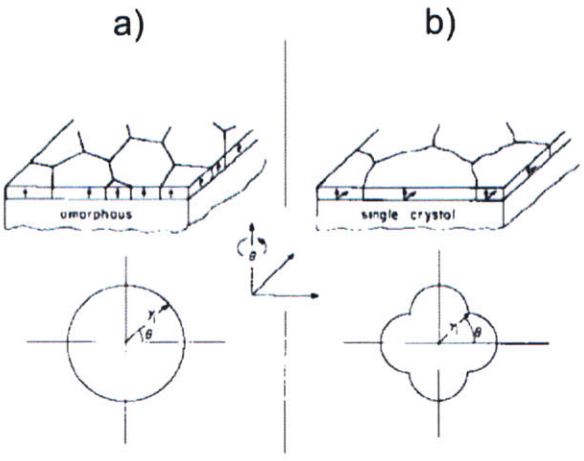

Figure 4-8: Effect of substrate crystallinity on the grain in-plane orientation. Grain structure and grain orientations for thin films deposited on amorphous (a) and crystalline (b) substrates after grain growth. Vertical arrows denote the surface orientation in (a). Horizontal arrows denote the in-plane orientation of grains in b). From ref. [75]

F-LG growth. This serves as a starting point in the understanding of the morphology change in F-LG films caused by the Ni grain structure.

4.2 Effect of Ni grain size: Ni film thickness and annealing time

The average Ni grain size during growth has an effect on the F-LG film morphology and thickness uniformity. Understanding this effect is relevant to some of the film properties such as optical transparency and electrical conductivity. In the present section, the effect of the Ni grain size on the film thickness uniformity, transparency and sheet resistance is discussed. Two factors affecting the Ni grain size, annealing time and Ni film thickness, are considered.

4.2.1 Ni film thickness

The use of various Ni thicknesses has an effect on the thickness uniformity of the F-LG grown (Figure 4-9). The size of the regions with 1-2 LG is a function of the Ni film thickness. This is due to the increase in the mean Ni grain size as shown in Figure 4-9(b). The correlation between the size of 1- and 2-LG and the Ni grains is also attributed to the preferential formation of multilayer graphene (+3 LG) at the grain boundaries. This is observed for cases with fast cooling rates during the F-LG formation (100-200 ^{o}C min^{-1}, see chapter 5). The transparency of the films across the visible range decreases with Ni film thickness (Figure 4-10(a)) even though the average size of the 1- and 2- LG regions increases (Figure 4-9(b)). From these measurements, the estimated average thickness of the F-LG films increases with the Ni thickness (Figure 4-10(b)). Figure 4-10(b) shows the transparency measured through 1, 2 ,3 and 4 F-LG films grown with 200nm and 300nm Ni. For these measurements, F-LG films where deposited on top of each other to form stacks of 1-4 F-LG films on a transparent substrate. The transmission through a single graphene layer is:

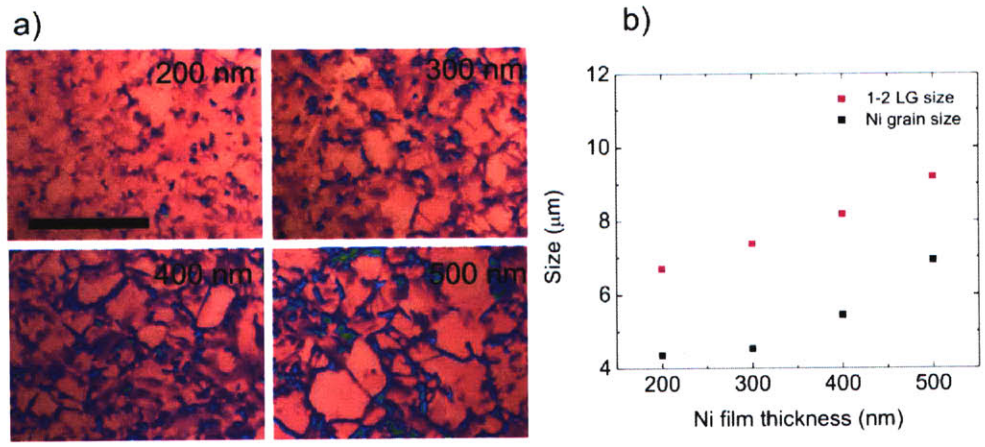

Figure 4-9: Effect of Ni film thickness.
a) F-LG films transferred to a SiO_2 substrate after grown from Ni films of various thicknesses. b)Average size of 1-2 LG sites and Ni grain size versus Ni thickness. Both increase in size in similar proportion as a function of Ni thickness.

$$T = (1 - \alpha\pi), \tag{4.15}$$

where $\alpha\pi = 0.023$ is the opacity of each graphene layer as found in ref. [9]. Treating each film and stack as the addition of discrete graphene layers [9] and neglecting reflectance between them, the transparency of each stack can be described by:

$$T = 100 \times (1 - \alpha\pi)^{nN} \tag{4.16}$$

where N is the number of films stacked and n is the average number of graphene layers per film. By fitting the plot in Figure 4-10(b) to the expression in 8.5, the estimated n is 4 and 7 layers per film for the cases of 200 and 300 nm Ni, respectively. These numbers are in agreement with the AFM data presented before in chapter 3. The sheet resistance (R_s) of F-LG grown with 200-500 nm Ni is shown in Figure 4-10(c). No clear trend is observed and the films stay in the range of 150-750 Ω/sq. This may be due to the effect of uneven doping on the films or non-optimized transferring conditions.

The increase in the average film thickness despite the enlargement of the 1-2 LG

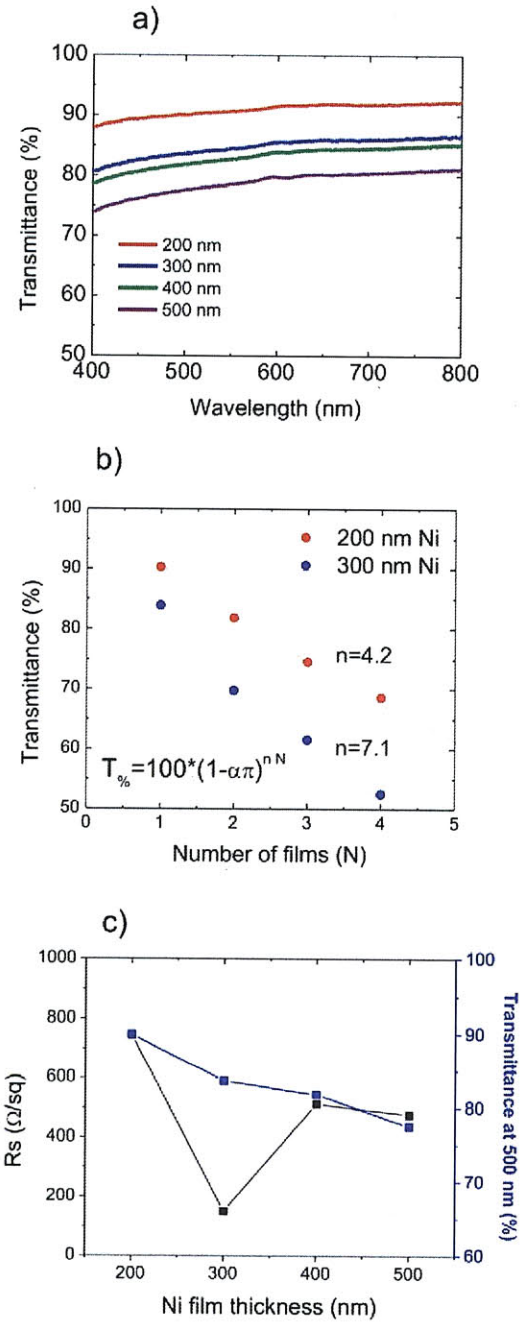

Figure 4-10: Properties of F-LG films as a function of Ni film thickness. a) Transparency across the visible range of F-LG films. b) Plot of the transparency of stacks of F-LG films. The stacks were fabricated by depositing various F-LG films fabricated under the same CVD conditions on top of each other. From the transparency vs. number of F-LG films, it is possible to estimate the average number of layers per film. F-LG films grown from 200 and 300 nm Ni have 4 and 7 graphene layers on average. c)Sheet resistance and film opticla transmittance as a function of Ni film thickness.

domains is explained by measuring the effective area coverage. This effect is observed to be reduced with increasing Ni thickness. That is, the average size of the domains is increased with increasing Ni thickness but their population per area falls significantly, thereby affecting the film transparency. Optical images of F-LG films are shown in Figure 4-11. Regions consisting of different number of layers are identified by different colors. The area fraction corresponding to these ranges of layer numbers is plotted in Figure 4-12(a). Estimation of the area fractions is possible due to the color contrast created by the FLG on the SiO_2-Si substrate. Such contrast depends on the local graphene film thickness. For the assignment of each color to an approximate range of number of layers see [11]. As shown in Figure 4-12(a), regions with larger number of layers increase in area with Ni thickness (10-15 and + 15 LG), while the lowest number of layers decrease their area fraction (1-2 and 3-9 LG). Sections with +3 LG appear to be located predominantly at the Ni grain boundaries. Therefore, it is thought that a larger amount of carbon segregates at the grain boundaries with larger Ni thickness (see chapter 5 for more discussion), increasing the average number of graphene layers per F-LG film.

In summary, the effect of the Ni film thickness is two-fold. On one hand, incrementing the Ni thickness helps in obtaining larger domains of monolayer and bilayer graphene due to an enlargement of the Ni grain size. On the other hand, the use of thicker Ni increases the average thickness of the F-LG that is forming at the grain boundaries. This causes an increment of the average film thickness and a reduction of the film's transparency. In the next section, the film uniformity is analyzed as a function of annealing time.

4.2.2 Ni film annealing time

The Ni grain size also depends on the annealing time. Figure 4-13(a) shows optical images of F-LG films on SiO_2-Si substrates grown with Ni films having different annealing times. All other growth parameters are the same. The size of the 1-2 LG domains grows slightly with annealing time. This is plotted for the average Ni grain size as a function of annealing time in Figure 4-13(b). Assuming a linear relationship

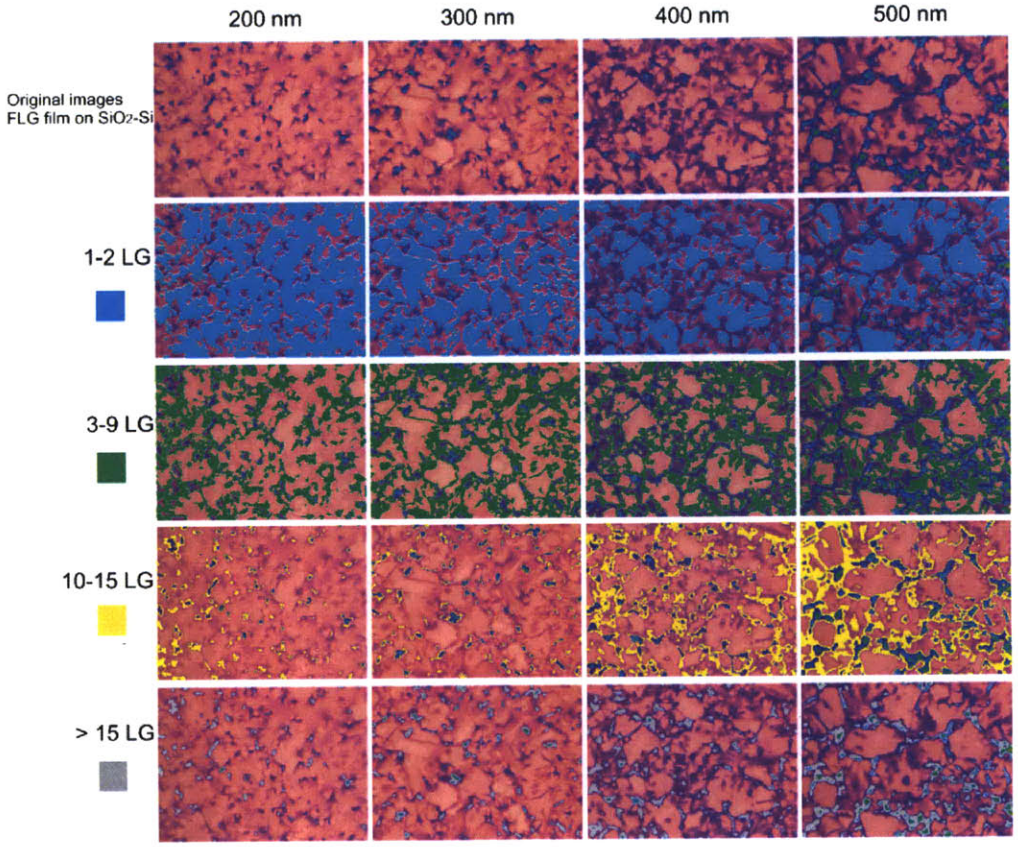

Figure 4-11: The area coverage of regions with different number of graphene layers. Optical images of F-LG films on SiO_2-Si grown on 200, 300, 400 and 500 nm Ni (top row, from left to right). The same optical images are shown below in separate rows. Each row corresponds to the same set of images. The images are tagged with different colors to indicate regions corresponding to 1-2 LG (cyan), 3-9 LG (green), 10-15 LG (yellow) and +15 LG (gray). The area occupied by 1-2 LG decreases with increasing Ni thickness. The abundance of graphene with a larger number of layers grows as Ni thickness increases. Regions with 3 or more graphene layers typically grow on Ni grain boundaries.

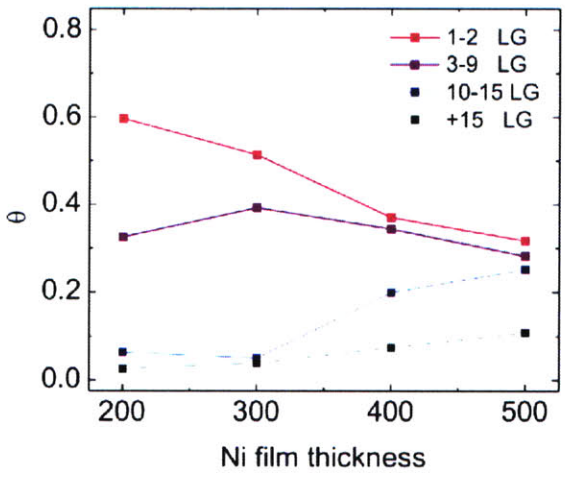

Figure 4-12: Area coverage θ as a function of Ni film thickness
a) Plot of the area fraction θ corresponding to sections with 1-2, 3-9, 10-15 and +15 LG. The area fraction with 10-15 LG and +15 LG increase with thicker Ni, while those of 1-2 and 3-9 LG decrease. The increase of the area occupied by larger layer numbers causes a lowering of the film transparency.

with annealing time, the estimated size increase rate for the 1-2 LG regions and Ni grains are 0.090 and 0.101 μm/min, respectively. The similarity in the magnitude of the rates suggests the influence of the Ni grain diameter on that of the 1-2 LG domains.

Transparency measurements show a very small increase in light absorbance in the visible range with changing annealing time (Figure 4-14(a)). No clear trend is observed again for the sheet resistance (R_s) as a function of annealing time (Figure 4-14(c)). The films stay in the range of 300-600 Ω/sq. Changes in sheet resistance can not be discriminated from other effects such as doping or changes in the transferring conditions. Quantification of the area covered by different ranges of layer numbers (Figure 4-14(b)) show a small increase of 0.011 min^{-1} in θ_{1-2LG} . This occurs together with a small decrease of 0.011 min^{-1} in $\theta_{10-15LG}$. No clear trend can be determined for the rest of the area fractions. This may explain the small change in transparency as a function of annealing time. These data are in contrast with the measurements

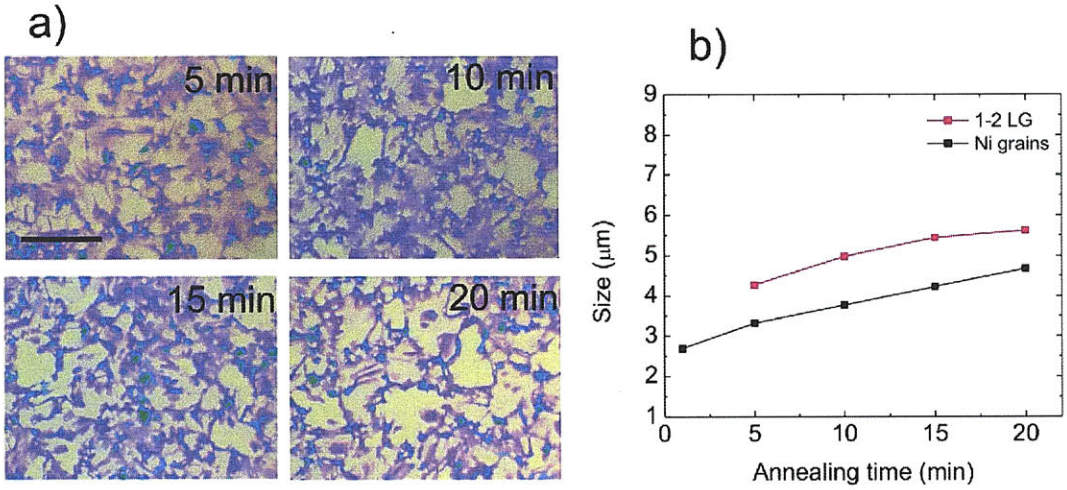

Figure 4-13: Effect of annealing time.
a) F-LG films grown with increasing annealing time and a constant Ni thickness of 300 nm. b) 1-2 LG and Ni grain sizes as a function of annealing time.

made as a function of Ni film thickness where a strong decrement in transparency is caused by a strong increment in $\theta_{10-15LG}$ and θ_{+15LG}. The average number of graphene layers per F-LG film remains close to 7 graphene layers for the annealing times used. Following the analysis for equation 8.6, the average number of layers forming at the boundaries is estimated to remain constant and close to 10 layers.

4.3 Summary

The size of the Ni grains has a strong effect on the properties and morphology of the F-LG. Regions composed of 1-2 LG were shown to form on top of the surface of Ni grains away from grain boundaries. On the other hand, F-LG with 3 or more layers precipitates on grain boundary locations. Changes in grain size and boundary population caused by the Ni film thickness and annealing times are expected to change the F-LG properties. Reasons for the precipitation of a larger amount of graphene layers on grain boundaries will be addressed in more detail in the next chapter where the segregation kinetics are considered.

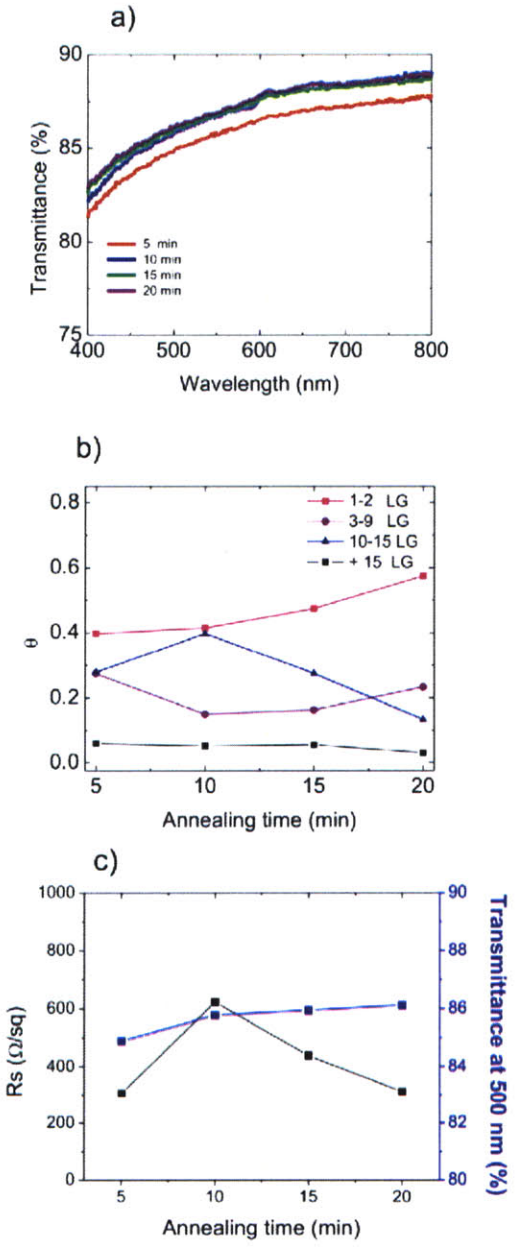

Figure 4-14: Transparency dependence with annealing time.
a) Transparency across the visible range of F-LG films as a function of annealing time. b) Area fraction θ occupied by 1-2, 3-9, 10-15 and +15 LG as a function of annealing time.

Chapter 5

The effect of cooling rate

In the first section of this chapter, the cooling rate during the CVD process is used to improve the thickness uniformity of the F-LG films. In the previous chapter, the cooling rates used to saturate the Ni film were relatively fast (¿100 ^{o}C min^{-1}). The morphology of the films obtained with fast cooling rates is contrasted against that obtained with cooling rates below 25^{o}C min^{-1}). The most important effect of lower cooling rates is an improvement of the area covered by 1-LG and 2-LG. Also a combined improvement of sheet resistance and optical transparency is found. In the last section of this chapter, a discussion is included on possible kinetic effects taking place during the segregation of carbon and graphene precipitation which may help understand the results obtained.

5.1 F-LG films produced with varying cooling rates on Ni thin films

In the CVD process, carbon is introduced into the bulk of Ni films (200-500 nm thick) due to the decomposition of CH_4. Graphene precipitation is induced during the cooling of the Ni-C solid solution formed. This is the expected mechanism of growth due to the following reasons. The temperatures at which the process operates are high enough to allow diffusion of carbon inside the Ni film (see chapter 3). This

was confirmed by measurements of the carbon concentration profile of some of the Ni films after growth (see appendix). The growth of graphene during the cooling stage is evident due to the strong dependence of the results on the variation of the process parameters during this stage. A detailed description of the steps of the CVD process is included in chapter 3. In this chapter, only the effect of the average cooling rate ($\overline{\frac{dT}{dt}}$ will be analyzed. The rest of the parameters are constant.

5.1.1 Two graphene morphologies

Two types of graphene films (A and B, shown in Figure 5-1) with contrasting thickness variations can be obtained by two cooling rate regimes. Films A consist mostly of graphene with more than 2 graphene layers and they are grown with fast cooling rates ($\geq$100 ^{o}C min^{-1}). It is observed that the Ni grain size plays a critical role in the thickness variation of the film, as explained in the last chapter. Multilayer graphene with more than 2 graphene layers (2+ LG) grows around the grain boundaries of the polycrystalline Ni film. Single layer and bilayer graphene grows at the center of the large Ni grains of the catalytic Ni film. These observations suggest that Ni grain boundaries act as preferential nucleation sites for multilayer graphene or graphite. Therefore, Ni films with different average grain sizes produce 1-2 LG regions of different sizes. In the second section of this chapter a discussion will be given in order to understand this observation.

Graphene films with their area consisting mostly of 1 and 2 LG (type B in Figure 5-1) are grown by using low cooling rates ($\overline{\frac{dT}{dt}}$ $\leq$25 ^{o} C min $^{-1}$). It is observed that not all grain boundaries on the polycrystalline Ni show the nucleation of multilayers, resulting in an increase of the area fraction covered by 1 and 2 LG. AFM, TEM, Raman spectroscopy and optical microscopy are used to characterize these films. The heights of 1 and 2 LG on SiO_2-Si as measured by AFM are 0.72 and 1.16 nm, respectively (Figure 5-2(a)). TEM confirmed that most of the film area consists of 1 and 2 LG (Figure 5-2(b)). The Raman G' band (2700 cm^{-1}) of 1 and 2 LG always has a single Lorentzian lineshape(Figure 5-3). For both cases, the linewidth usually lies between 30 and 40 cm^{-1}, suggesting the absence of interlayer coupling. Therefore,

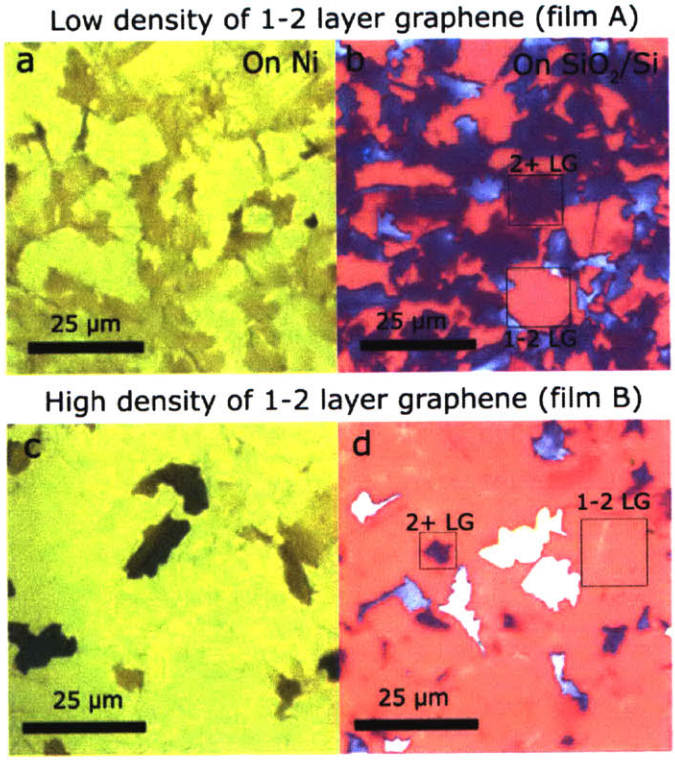

Figure 5-1: The effect of cooling rate.
Optical images of F-LG films grown with fast ($\geq$100 ^{o}C min^{-1}) (a-b) and slow ($\leq$25 ^{o}C min^{-1}) (c-d) cooling rates before (a,c) and after transferring (b,d) to SiO_2-Si. With fast cooling rates, multilayer graphene with more than 2 layers forms around the grain boundaries of the Ni film. With slow cooling rates, multilayer graphene precipitates on isolated islands randomly distributed across the Ni film. Regions between the islands are formed by 1 or 2 LG.

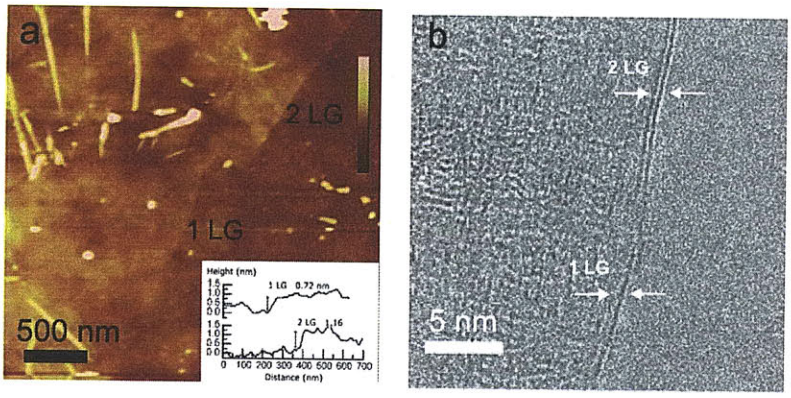

Figure 5-2: 1-LG and 2-LG from films grown with slow cooling rates ($\leq$25 ^{o}C min^{-1}). a) AFM image on the edge of a F-LG film showing regions with 1 or 2 LG. The cross section height measurements for both cases are 0.72 nm and 1.36 nm, respectively. b) TEM images showing the folded edge or regions with 1 and 2 LG.

the distinction between 1 and 2 LG is not possible using Raman spectroscopy by itself. The Raman spectra of the films will be discussed further in chapter 8. This identification is better done by optical microscopy (see appendix) or direct observation in a TEM.

Having defined the main differences in morphology between two cooling rate regimes, in the following subsection, the effect of $\overline{\frac{dT}{dt}}$ on the film thickness uniformity is discussed further. Observations regarding area fractions, transparency and sheet resistance are presented as a function of the cooling rate.

5.1.2 Thickness uniformity as function of cooling rate

It was found that in type B films, the area covered by 1-2 LG (θ_{1-2LG}) is dependent on the cooling rate in the regime of $\overline{\frac{dT}{dt}}$ $\leq$25 ^{o} C min $^{-1}$. Figure 5-4 shows that decreasing the cooling rate below 25 ^{o} C min $^{-1}$ during the segregation step further increases the area fraction of 1-2 LG (pink background). In addition, the slower the cooling rate, the fewer are the nucleation sites of multilayer graphene (ρ_{+2-LG}). The decrease in the density of multilayer sites can be also attributed to a reduction of the rate of arrival of carbon atoms at the surface caused by the lowering of $\overline{\frac{dT}{dt}}$. At low segregation rates, carbon atoms could diffuse for longer times before they coalesce

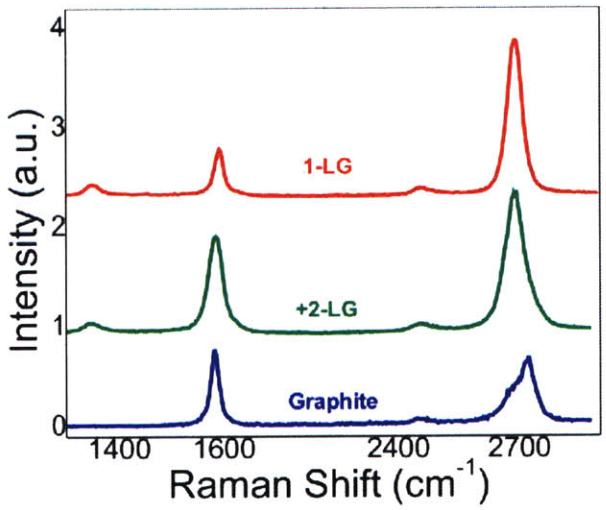

Figure 5-3: Raman spectra from F-LG films fabricated with cooling rate of 4 ^{o}C min^{-1}.
1 and 2 LG are shown in red, multilayers with more than 2 LG and less than 20 LG in green and graphite islands in blue. The laser wavelength is 532 nm.

to form graphene (diffusion limited nucleation). The cooling rate of the Ni film during graphene precipitation was used to obtain films with up to 87% of their area (θ_{1-2LG}= 0.87) composed of no more than 2 layers of graphene. The area fractions θ_{1-2LG} increase as the cooling rate is decreased and they can be tuned from 0.6 to 0.87 with the cooling rate (Figure 5-5(a)). The area covered by 1 and 2 LG is plotted together since this is the area fraction changing noticeably with the cooling rate. This area corresponds to the background between multilayer graphene islands (see optical images in Figure 5-4). The area with 1 LG is estimated to remain constant close to 0.1-0.15. The density of sites consisting of multilayer graphene with more than 2 layers, θ_{+2LG}, can be decreased by 50% from the highest to the lowest cooling rate tested (Figure 5-5(b)). No significant change in ρ_{+2LG} or θ_{1-2LG} was observed if Ni thin films with different grain sizes are used. Blue and orange data points in Figure 5-5(a) and (b) correspond to grain sizes L_1 and L_2 which are shown in Figure 5-5(c) and (d). Optical images of graphene films grown with 4^{o} min^{-1} on these two Ni grin sizes before and after transferring to SiO_2-Si are shown in Figure 5-5(e-f) and (g-h),

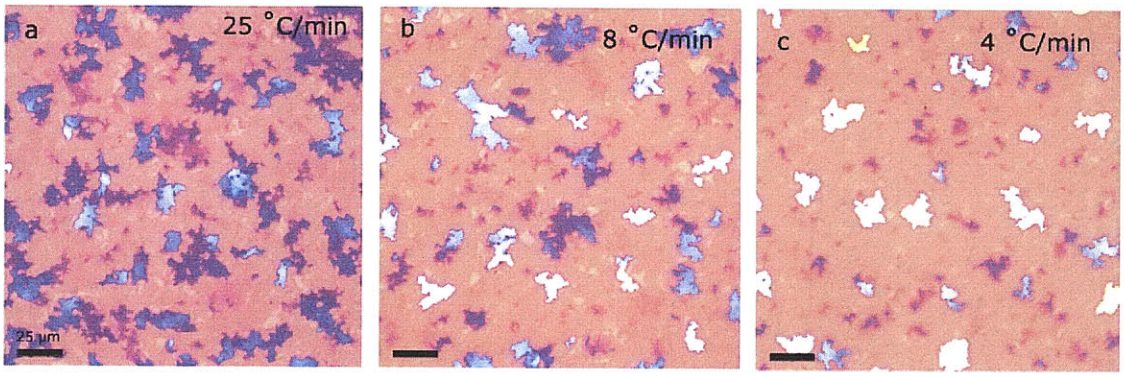

Figure 5-4: F-LG films transferred to SiO_2-Si and grown with three cooling rates. Decreasing cooling rates are shown from left to right. The density of multilayer islands decreases with decreasing cooling rates. Regions between the islands consisting of 1 and 2 LG increase in area fraction with decreasing cooling rates.

respectively.

The quantification of the area percentage plotted in Figure 4 was done comparing optical images of the graphene films on SiO_2-Si and bare SiO_2-Si substrates and measuring the optical contrast created by the graphene film (see appendix). Since the contrast depends on the number of layers, it enables the identification of regions with down to 1- and 2-LG in an automatic way (see appendix). The area fractions plotted in Figure 4b represent the fraction of pixels identified as containing 1-, 2-, 3- and 4-LG. Optical images at 50× magnification, with 3900 by 3090 pixels (289 by 229 μm^2), were used for this analysis. These films are also transferable to any other substrate material similar to the way described in chapter 3. Graphene films of up to 1 in^2 in size and high area fractions of 1-2 LG can be fabricated. Their sizes only depend on the Ni film used and the CVD chamber size.

5.1.3 Properties as a function of cooling rate

Optical transmission and sheet resistance measurements were performed on as transferred films with various cooling rates. Although the density of multilayer graphene changes with cooling rate, transmission measurements show a negligible change in transparency (Figure 5-6 (a-b)). Sheet resistance measurements show an order of

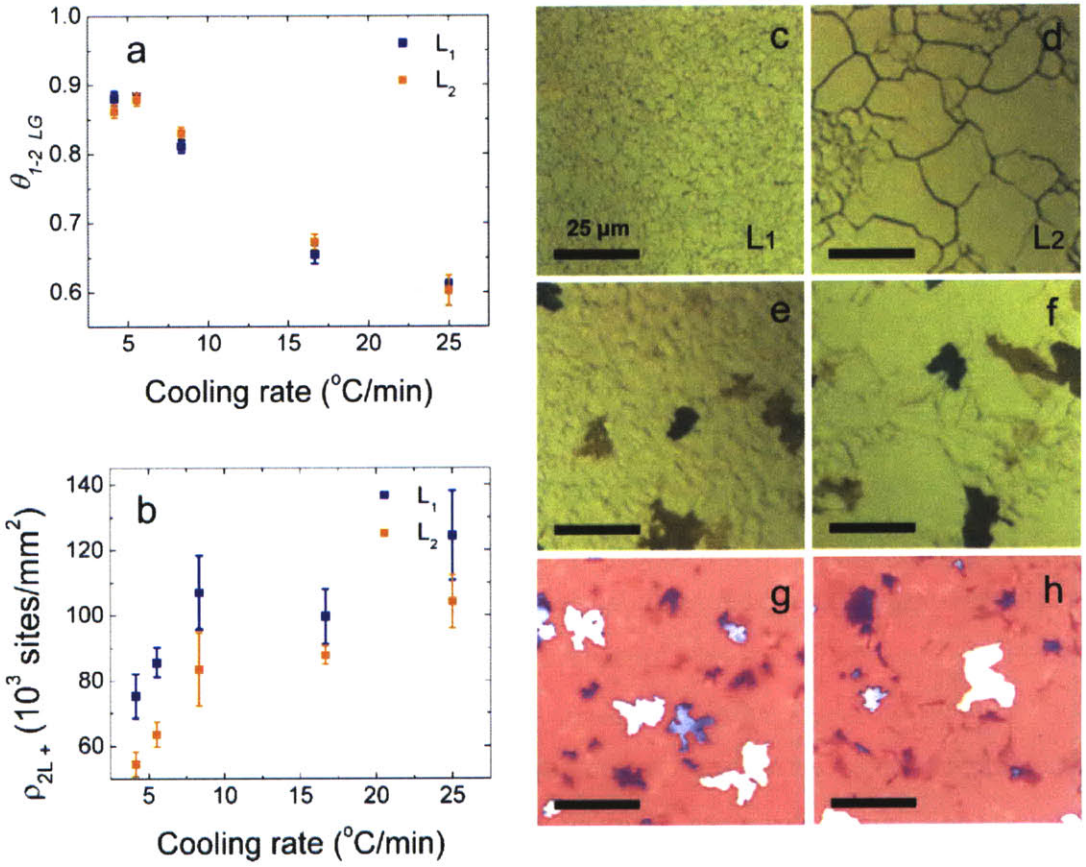

Figure 5-5: Area fraction of regions with 1 and 2-LG.
a) Area fraction occupied by 1 and 2 LG as a function of cooling rate. b) Density of multilayer islands (+2 LG) as a function of cooling rate. a) and b) includes data for two Ni grain sizes (L_1 and L_2 in blue and orange, respectively). c-d) Optical images of pristine Ni films with grain sizes L_1 and L_2, respectively. e-f) Optical images of Ni films with the same grain sizes after the CVD process. g-h) F-LG transferred to SiO_2-Si and grown on Ni films with L_1 and L_2, respectively.

magnitude decrease with increasing cooling rates (Figure 5-6 (b)). It was expected that the sheet resistance would remain constant as a function of cooling rate since the multilayer islands on the films are not connected. The electrical conduction is expected to occur through the 1 and 2 LG regions only, therefore, any change in the multilayer island density would not affect the amount of current carried by the film. Further work and analysis is needed to explain this observation. Finally, transmission measurements suggest an average thickness of 5 graphene layers for films fabricated with a cooling rate of 4 ^{o}C min^{-1} ((Figure 5-6 (c)). This estimation is done also by measuring the transmission from stacks with increasing number of F-LG film (see last chapter).

5.2 Summary

The rate at which Ni films are cooled affects the morphology of the F-LG films. Cooling rates $\geq$100 ^{o}C min^{-1} show multilayer graphene with more than 2 layers precipitated around the grain boundaries of the thin Ni film. In this case, the area fraction of 1 and 2 LG depends strongly on the grain size of the Ni film. However, if slow cooling of $\leq$25 ^{o}C min^{-1} are used, multilayer graphene (+2 LG) precipitates at random locations across the Ni film, therefore, increasing the area occupied by monolayer and bilayer graphene. Regions between isolated multilayer islands consist of 2 LG or 1 LG. If the cooling rate is decreased further, the density of multilayer islands continues to decrease maximizing the area occupied by 1 and 2 LG. The largest area fraction obtained for 1 and 2 LG together is $\approx$0.87. The area occupied by 1 LG is close to 0.15 and remains close to this value for the cooling rates used.

In the last two chapters, F-LG has been produced on polycrystalline Ni. It was observed that the Ni microstructure affects the film uniformity. Grain boundaries may play an important role in the formation of multilayer graphene. The next chapter considers the use of single crystal Ni pieces for the fabrication of graphene.

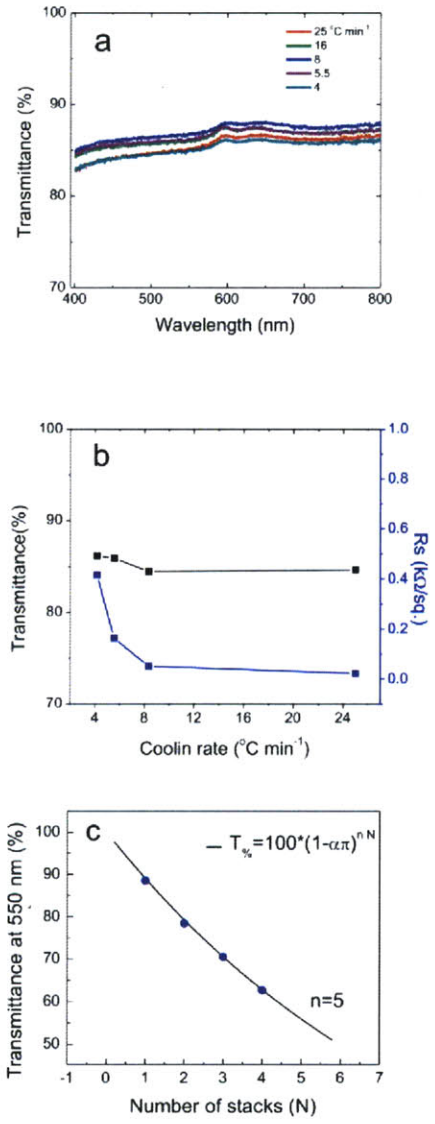

Figure 5-6: Transmittance and average F-LG film thickness.
a) Transmittance across the visible range for F-LG produced with various cooling rates. No trend is observed for the transmittance as a function of cooling rate. b) Transmittance (at 500 nm) and sheet resistance (R_s) of films as a function of cooling rates. R_s decreases an order or magnitude for increasing cooling rates. c) Transmittance as a function of number of F-LG films stacked over one another. From the fitted transmittance curve, an average thickness of 5 graphene layers per film is estimated.

Chapter 6

Growth on Ni Single Crystal Substrates

In the previous chapters, the growth of F-LG films on Ni thin films (200-500 nm thick) was presented. The choice of these films was based on their accessibility in many laboratories and the fact that their thickness facilitates the transferring of the graphene. However, these films are usually polycrystalline and the microstructure of the film, i.e. the grain size and grain boundary density, influences the thickness uniformity of the F-LG film. In this chapter, the use of single crystal substrates is considered. The work presented here was done with the expectation of improving the thickness uniformity of the graphene grown on Ni. This was expected to occur since single crystals would present a decreased grain boundary density for multi-layer graphene precipitates. Three surface orientations of Ni are considered; Ni(111), Ni(100) and Ni(110). Each case is discussed in a different section. The segregation of carbon atoms to these Ni surfaces has been explored before by Blakeley et al. in the 1970s [47, 82, 83, 84, 85]. This was done by fixing the carbon concentration inside a single crystal piece of Ni and cooling it under UHV conditions. In the work presented in this chapter, the approach is different to that from Blakely et al. The same procedure used in chapter 3, involving CVD under ambient pressures, is used. Carbon is incorporated into the Ni piece by the catalytic decomposition of CH_4 during a CVD process and the segregation is done by a cooling of the Ni piece.

6.1 Growth on Ni(111)

The Ni(111) surface has been of interest to researchers for growing graphite and graphene due to the close lattice matching between the two (a_{Ni}=2.44 Å and a_g=2.46 Å) [58, 59, 86, 87]. In the case of carbon segregation to Ni surfaces, the case of Ni(111) is unique since a graphene monolayer on Ni(111) is one of the surface's equilibrium phases during carbon segregation. That is, during the segregation of carbon atoms to the surface of Ni(111), one graphene monolayer forms a stable phase with a lower enthalpy of segregation compared to that of the graphite precipitate phase. The difference between them is about 0.06 eV. Blakely et al. showed these effects during equilibrium segregation studies of carbon impurities to different crystallographic faces of Ni [47, 82, 83, 84, 85].

The observations of Blakely et al. are helpful in the understanding of the results obtained using the APCVD process in chapter 3 and single crystal Ni(111) pieces. In the next subsection, the main findings of Blakely et al. are reviewed followed by the results obtained using ambient pressure APCVD.

6.1.1 Equilibrium segregation of carbon to a Ni(111) surface

The study of the segregation of impurities to free surfaces and grain boundaries was mainly geared towards an understanding of the role of grain boundaries in the mechanical properties of metallic alloys [88]. In these studies, surface characterization tools such as Auger, XPS and LEED are used to monitor the coverage of the segregating atoms on the surface of a solid. A typical experiment would involve fixing the concentration of the impurities of interest in the bulk of a crystal and monitoring the crystal's surface with the techniques mentioned above. This was done during cycles of cooling and heating. The temperature change rates are slow enough to ensure that the system equilibrates after each small change of temperature (equilibrium segregation).

Blakely et al. found that segregating carbon atoms formed three distinct stable phases on a Ni(111) surface at different temperature ranges and at bulk carbon con-

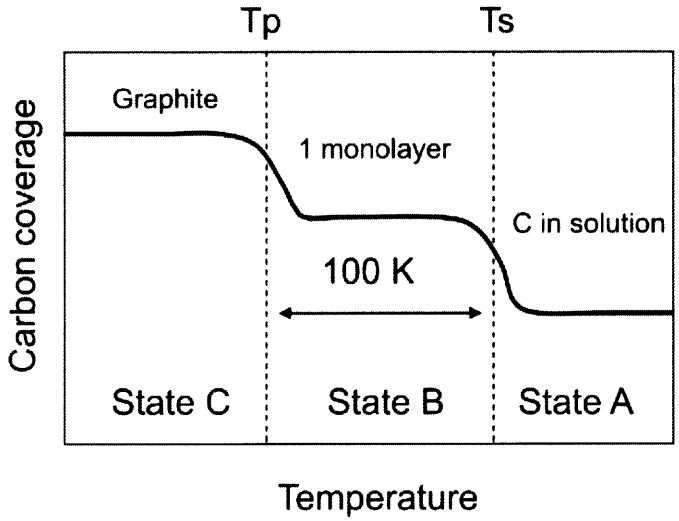

Figure 6-1: Schematic view of the surface segregation phases on the Ni(111)-C system. The vertical axis represents the amount of carbon segregated on the surface and the horizontal axis represents temperature.

centrations of 1% at. The three observed phases are the following (Figure 6-1). 1) A high temperature phase ($T \geq T_s$) consisting of diluted carbon atoms on the surface. 2) An intermediate phase ($T_p \leq T \leq T_s$) where the segregating carbon atoms form a monolayer of graphite on the Ni(111) surface. 3) A low temperature phase ($T \leq T_p$) in which precipitation of graphite occurred. These observations [47] were the first reports of distinct transitions between phases of segregations. The intermediate phase exists for a range of 100 K before the graphite precipitate appears. Blakely et al. differentiate between equilibrium segregation and precipitation. The former refers to the accumulation of impurities at a surface during compositional homogeneity in thermal equilibrium, that is, while the system is at the one-phase field of the phase diagram. This description is assigned to the first transition (T_s). Equilibrium precipitation refers to inhomogeneities which arise due to equilibrium phase separation. This is assigned to the second transition (T_p) and is thought of as the normal precipitation of graphite that occurs from saturated transition metals.

The existence of an intermediate phase between slowly segregating carbon atoms (phase 1) and the graphite precipitate (phase 3) is explain by a higher binding energy of a monolayer of carbon atoms on the Ni(111) surface with respect to that of the

graphite precipitate (0.06 eV). This higher binding energy also explains why the formation of the monolayer occurs at a temperature above the precipitation temperature (100 K).

The heat of segregation can be estimated by equating the chemical potential of the carbon atoms in solution to the chemical potential of the monolayer at T_s:

$$\mu_{sol}(T_s) = \overline{G}(T_s) + kT_s \ln \chi = \mu_{mono}, \tag{6.1}$$

and to the chemical potential of graphite at T_p:

$$\mu_{sol}(T_p) = \overline{G}(T_p) + kT_p \ln \chi = \mu_{graphite} \tag{6.2}$$

where $\overline{G}$ is the partial atomic free energy of solution and χ is the fraction of available interstitial sites occupied by carbon atoms in the bulk. The chemical potential of graphite is set as the reference point and set to zero. The free energy of solution can be expanded to its enthalpy and entropy terms as found in reference [89]:

$$\overline{G}(T) = \overline{H}_{sol} - T\overline{S}_{sol} = 0.49eV + 0.2kT. \tag{6.3}$$

With this and equation 6.2, the carbon solubility is obtained:

$$\ln \chi = -0.2 - \frac{0.49}{kT_p}. \tag{6.4}$$

Figure 6-2 shows T_p as a function of the carbon concentration used for different Ni crystals (χ). Notice the data fits well to the expression in 6.4. To obtain the relationship between T_s and carbon concentration χ, equations 6.1 and 6.3 are used so:

$$\ln \chi = \frac{\left(\overline{H}_{mono} - \overline{H}_{sol}\right)}{kT_s} - \frac{\left(\overline{S}_{mono} - \overline{S}_{sol}\right)}{k} = \frac{\Delta\overline{H}_{seg}}{kT_s} - \frac{\Delta\overline{S}_{seg}}{k}, \tag{6.5}$$

where $\Delta\overline{H}_{seg}$ and $\Delta\overline{S}_{seg}$ are the enthalpy and entropy of segregation, respectively.

By fitting the experimental values of Ts (Figure 6-2), Blakely et al. obtained a value of 0.55 eV for $\Delta\overline{H}_{seg}$. The binding energy per carbon atom on for the monolayer

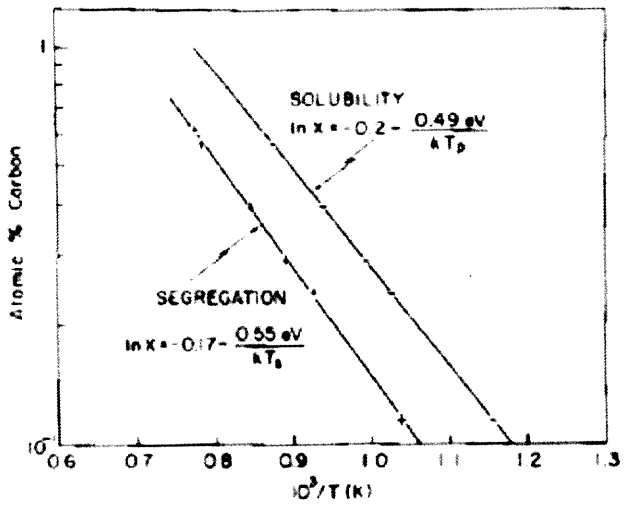

Figure 6-2: Arrhenius plot of the carbon concentration in Ni versus T_s and T_p. The precipitation of graphite occurs at lower temperatures with a lower enthalpy of segregation. From ref [47].

on the Ni(111) surface is 0.55 eV. For the graphite phase it was found to be 0.49 eV. Figure 6-3 shows an energy diagram describing the observations made by Blakely at al.

In the next subsection, it is shown that by using the APCVD process presented in chapter 3 it is possible to grow only one monolayer of graphene on the entire surface of Ni(111). It is argued that this occurs since one monolayer is a thermodynamic phase distinct from the graphite one as described by Blakely et al. The graphite precipitation is avoided by quenching the Ni-C solid solution at high cooling rates ($\geq$ 100 ^{o}C), therefore, freezing the equilibrium phase of 1 LG on Ni(111).

6.1.2 Graphene monolayer by CVD-enabled segregation

It is possible to grow only one monolayer of graphene using the process described in chapter 2 on single crystal pieces of Ni(111). After transferring, it is possible to observe the existence of 1-LG across areas as large as the size of the Ni substrate. The fabrication process is described in Figure 6-4. Round Ni pieces of 1 cm in diameter and 1mm thick were acquired from Marketech International. The surface of the pieces was polished with colloidal silica and a Politex pad (Eminess technologies) to a roughness

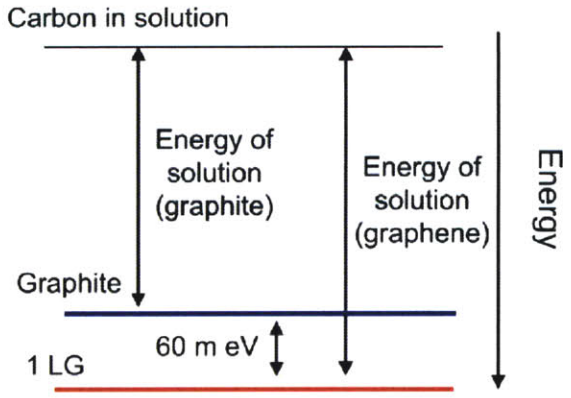

Figure 6-3: Single atom energy diagram for carbon in Ni(111).
The diagram shows the binding energies for the monolayer and graphite phase during carbon segregation to a Ni(111) surface.

close to 0.5 nm (rms). AFM images of the samples as received and after the samples are polished are shown in Figure 6-5. The polishing step was crucial in order to grow 1-LG homogenously across the whole Ni surface. Excessive roughness is thought to lower the nucleation barrier for multilayer graphene as discussed in previous chapters. The CVD process is the same as that presented in chapter 3. However, there are two differences. One is the absence of an annealing step. The other is that the amount of methane utilized is significantly higher. Now a concentration of 10% vol. is used instead of 0.5%. Moreover, cooling rates above 100^{o}C min^{-1} are used. Fast cooling rates were also essential in the growth of a monolayer of graphene by this process and its role will be discussed below. Figure 6-5 also shows AFM images of the Ni(111) surface after graphene growth. Wrinkles formed due to the expansion of graphene during cooling which are visible on the surface by AFM.

The transferring steps used are similar to those used for Ni thin films (Figure 6-4). However, only a mild aqueous solution of hydrochloric acid is used (3 % wt.). The etching occurs only at the interface between the graphene and the Ni surface allowing the detachment of the PMMA/graphene stack without destroying the entire Ni sample. This also enables the reuse of the Ni pieces. After each transfer the Ni pieces are polished again and used for graphene growth iteratively. This has been confirmed by using the same Ni crystal up to four times. Figure 6-6 shows optical and

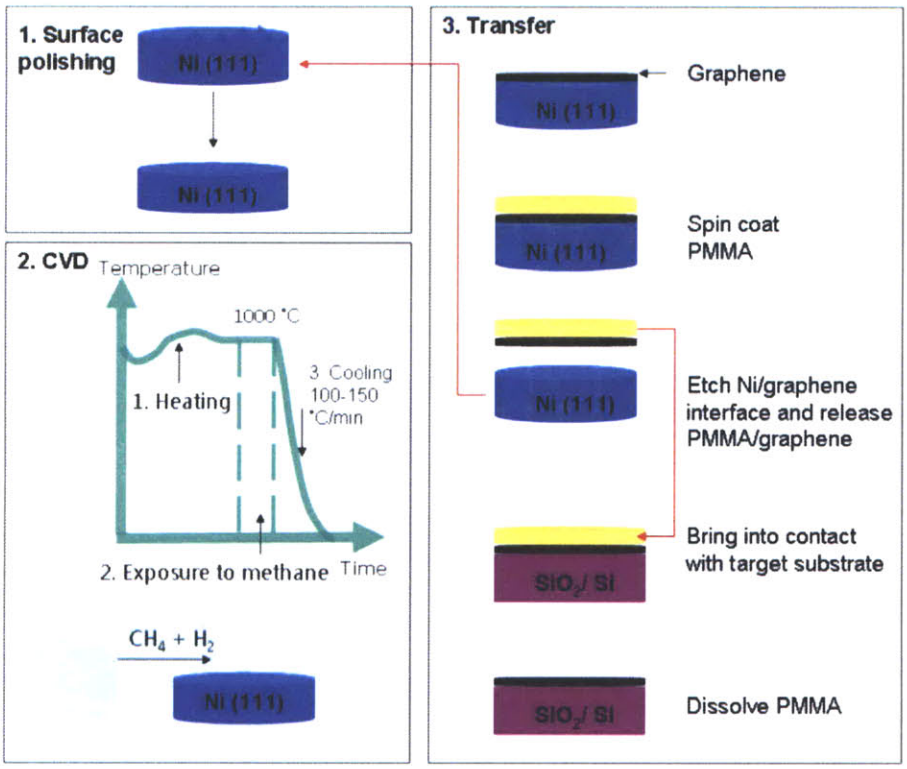

Figure 6-4: Processing steps for the fabrication of uniform 1-LG from Ni(111). First, the Ni substrates are polished with colloidal silica to an rms roughness of ≈0.50 nm. A CVD process with similar steps that are described in chapter 3 is used to grow a monolayer of graphene. In this case, there is no annealing step. The temperature of the furnace is stabilized after introduction of the sample (1). A flow rate of 1000 sccm of H_2 is used. After this, 100 sccm of CH_4 is introduced with no change in the H_2 flow rate (2). After five minutes of methane exposure, the sample is quenched by taking the silica tube with the Ni sample out of the furnace to ambient temperature. The estimated cooling rate is $\geq$100 ^oC min^{-1}. Transferring of the graphene is done by etching the Ni-graphene interface with a mild HCl aqueous solution. A PMMA layer is also spin coated previous to the etching. The released PMMA/graphene membrane is laid on the target substrate and the PMMA is dissolved with acetone or annealing under Ar and H_2 gas.

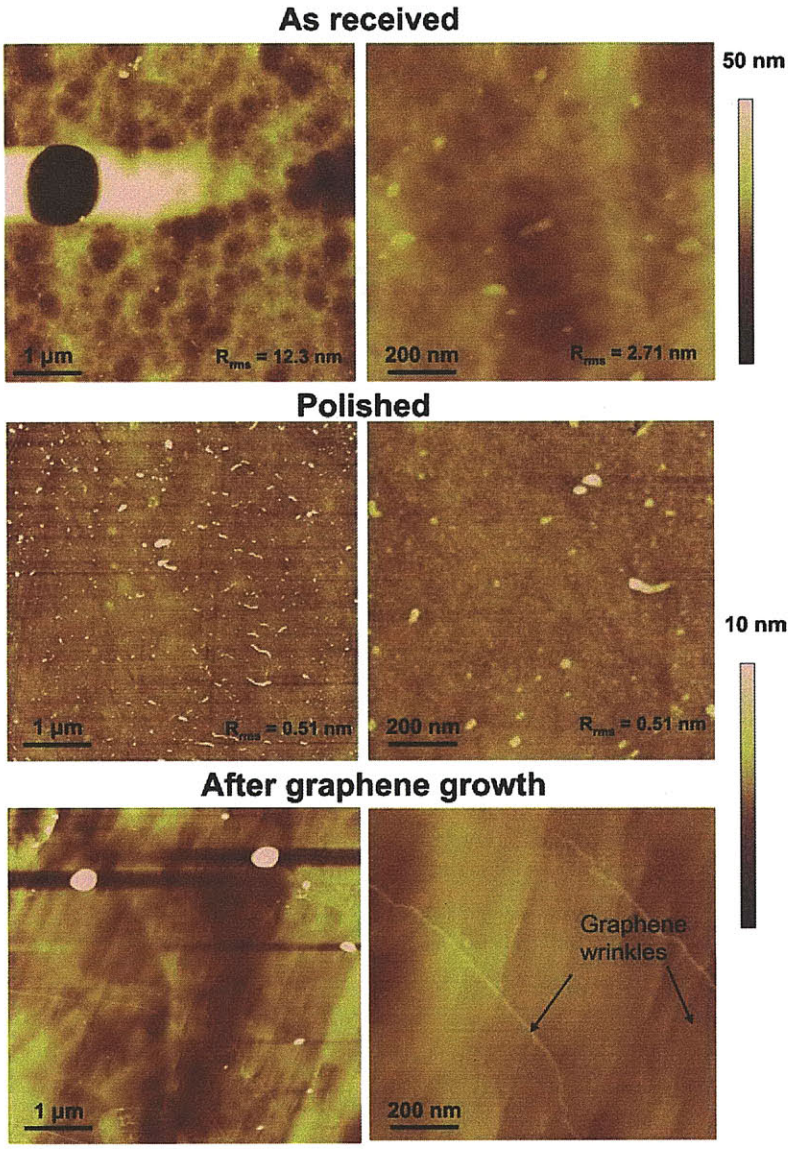

Figure 6-5: AFM images of the Ni(111) substrates.
Images for Ni(111) as received, after polishing and after CVD are shown. Two images with different magnifications ($5\times5\mu m^2$ and $1\times1\mu m^2$, left and right, respectively) are shown for each case. The roughness is reduced to 0.51 nm (rms) after polishing. The surface roughness below 1 nm was crucial for the growth of a uniform graphene monolayer.

AFM images of 1-LG after transferring to SiO_2-Si. Notice that islands of multilayer, which are noticeable in the optical microscopy for samples of previous chapters, are no longer present. The Raman spectra of the grown 1-LG is similar to the one of 1-LG from polycrystalline Ni and from natural graphite (Figure 6-6(d)). The G′ shows a linewidth of 42±6 cm^{-1}. However, the determination that 1-LG has been grown is done by measuring the optical contrast that the graphene layer creates with respect to the SiO_2-Si substrate. The same procedure used in chapter 5 is implemented for the determination of the layer number. The change in the green chanel intensity of the optical image at a graphene edge on SiO_2 is shown in Figure 6-7(a). The expected green intensity for 1-LG on the substrate at the corresponding illumination conditions is included and is in agreement with the measurement. A 97% coverage with 1-LG is estimated by analyzing the color contrast of 200×200 μm optical images. Figure 6-7(b) shows one of the images analyzed and Figure 6-7(c) shows the same image with the pixels identified with 1-LG set to white.

Ni(111) single crystals can be used with ambient pressure CVD in order to grow 1-LG across large areas on the order of cm^2. This is probably possible due to the polishing of the surface which helps in decreasing the abundance of crystal steps and the fast cooling rates used during carbon segregation. It is thought that by cooling the Ni(111) piece fast enough, it is possible to allow enough time for segregation to form 1 LG on Ni(111) but not enough time to allow the precipitation of the graphitic phase. The 1-LG phase is stable at temperatures 100 °C higher than the temperature at which graphite precipitates during the segregation process. By quenching the Ni(111) crystal, the surface may freeze at the 1-LG phase before graphite precipitation.

The next sections will discuss the segregation of carbon on the other two Ni surface orientations, Ni(100) and Ni(110). This will be done in order to understand better the selective growth of 1-LG on Ni(111) and make predictions on the feasibility of graphene growth on other crystal orientations.

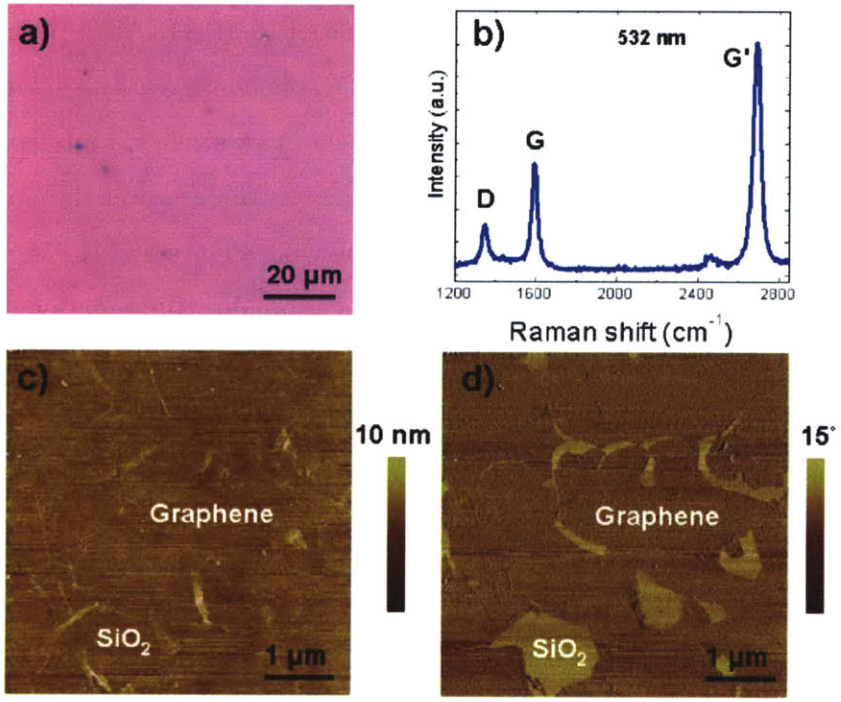

Figure 6-6: 1-LG grown on Ni(111) after transferring to SiO_2.
a) Optical image (100×) of the grown 1-LG transferred to a SiO_2-Si substrate. The uniform color of the image suggests the abundance of 1-LG over the whole surface. b) Representative Raman spectra obtained from 1-LG produced this way. The presence of the D band suggests the existence of defects. The G′ band lineshape is similar to that from the 1-LG obtained from polycrystal Ni (chapters 3, 5 and 8) with an average linewidth of 42± 6 cm^{-1}. AFM height (c) and phase (d) images taken at the same spot on the 1-LG surface after transferring to SiO_2-Si confirming the existence of graphene on the SiO_2 surface. The phase image usually creates a larger contrast with respect to bare SiO_2-Si allowing the identification of the graphene deposited. Breaks on the 1-LG are observed. These are thought to arise from an imperfect transferring process.

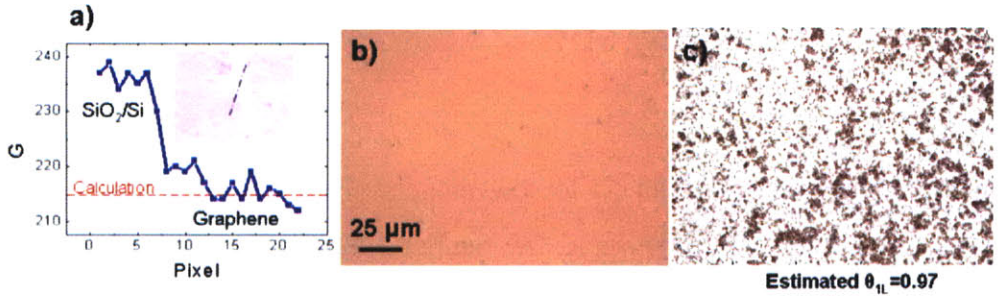

Figure 6-7: Quantification of the area covered by 1-LG after transferring to SiO_2. a) Green component values (G) taken from a cross section of a 1-LG edge next to bare SiO_2-Si. The cross section is taken from an optical image with the RGB format. The change in the G value corresponds to that expected for 1-LG based on the identification method described in the appendix (see also chapter 5). b) An optical image used to implement the identification of 1-LG across the surface. c) Image in b) after identification of pixels corresponding to 1-LG (tagged with white). An estimation of 97% coverage of a monolayer of graphene is obtained. Most of the untagged parts of the image are identified as bare SiO_2-Si due to breakings of the 1-LG during transferring.

6.2 Equilibrium segregation of carbon to other Ni surface orientations

6.2.1 The Ni(100) surface

The segregation of carbon impurities to Ni(100) surfaces was also studied by Blakely et al in references [83, 84, 85]. There are important differences between the segregation behavior of carbon on this surface when compared to Ni(111). The equilibrium coverage as a function of temperature follows a Langmuir model such that:

$$\frac{\theta}{1-\theta} = \frac{X_{sol}}{1-X_{sol}} \exp\left(\frac{\Delta\overline{G}_{seg}}{kT}\right), \tag{6.6}$$

where X_{sol} is the concentration of carbon in solution relative to the bulk and $\Delta\overline{G}_{seg} = \overline{G}_{surf} - \overline{G}_{sol}$, the free energy difference of the segregation reaction. This is the simplest model of segregation of impurities because it is limited to one monolayer of segregating species. It assumes a finite number of localized non-interacting sites provided by the

first monolayer of the bulk lattice, therefore, it has the form of a Fermi distribution function.

The surface coverage on Ni(111) for the monolayer phase as a function of temperature occurs in a sharp transtion at the temperature T_s. In order to fit it with a Langmuir model, it would require a $\Delta\overline{G}_{seg}$ of 65 eV which is unrealistic. Usually the coverage on Ni(111) is modeled taking in consideration interacting carbon sites [47]. For the case of Ni(100), the segregation phase transitions observed are carbon arrangements with p(1×1) and c(2×2) symmetries(Figure 6-8) with respect to the Ni surface (following the Woods notation). The letters p and c denote a primitive and centered unit cell, respectively. The numbers specify how many unit cells of the underlying substrate correspond to the unit cell of the arrangement formed by the segregating atoms. The surface coverage (θ) of carbon with the symmetries above on the Ni(100) surface fits well to a Langmiur model, in contrast with the Ni(111) case. After the two surface phase transitions mentioned above, the graphite precipitate is observed. Figure 6-9 shows a Langmuir plot of the surface coverage of carbon as a function of temperature. The high temperature section of the plot corresponds to a p(1×1) arrangement of segregating carbon at the Ni(100) surface. The intermediate section corresponds to the c(2×2) arrangement. Tp is the temperature at which the graphite precipitate was observed. The identification of the different symmetries of the carbon arrangements was done by LEED. The same for the identification of the graphite phase. Using the same thermodynamic approach used for the Ni(111) case, the segregation enthalpy for the p(1×1) and c(2×2) are fround to be 0.47 and 0.23 eV, respectively. A one atom energy diagram including the Ni(100) and Ni(111) segregation phases is shown in Figure 6-10.

Based on Blakely's observations, it should not be expected that a graphene monolayer grows uniformly on Ni(100) under similar conditions are presented in the last section. The case of Ni(110) is not much different to Ni(100) and it will be briefly discussed next.

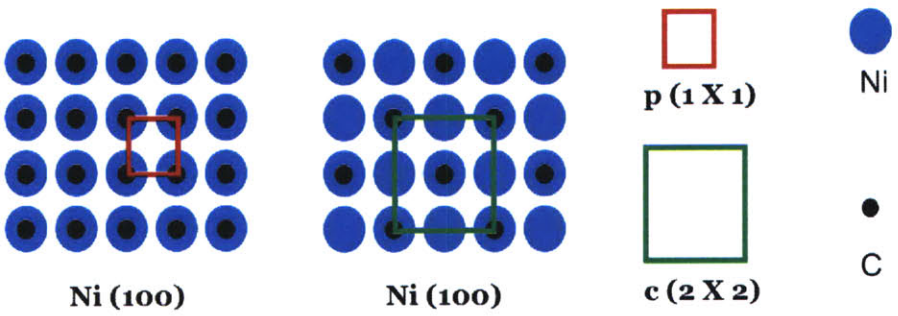

Figure 6-8: Representation of the p(1×1) and c(2×2) arrangements of carbon atoms segregated to a Ni(100) surface.

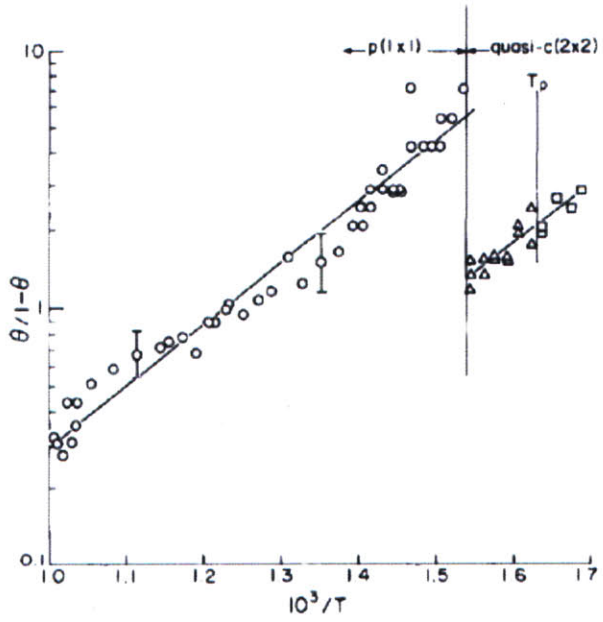

Figure 6-9: Plots of the surface coverage θ of carbon atoms on a Ni(100) surface. For the section with the p(1×1) symmetry, θ=1 is set to be a complete p(2×2) monolayer (1 carbon atom per 4 Ni atoms). For the section with the c(2×2) symmetry, θ=1 is set to be a complete c(2×2) monolayer (1 carbon atom per 2 Ni atoms). From Blakely et al. [84].

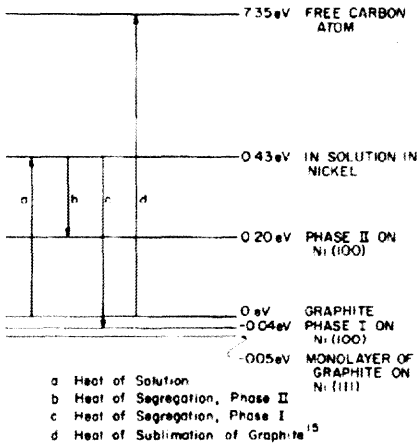

Figure 6-10: Single atom energy diagram showing the binding energies for the phases observed during the segregation of carbon atoms to the Ni(111) and Ni(100) surfaces. From ref [84].

6.2.2 The Ni(110) surface

Blakely mentions that during equilibrium segregation experiments no carbon phase is observad on the Ni(110) surface during cooling or heating of the Ni-C solution. It is expected that the free energy of segregation at this surface is positive and therefore does not occur. However, the precipitation of graphite at the expected T_p is observed [85]. Therefore, no uniform monolayer growth should be expected during the APCVD process applied for Ni(110). Only graphite precipitates should result from the growth procedure. Experimental results for the Ni(110) and Ni(100) crystal orientations using the APCVD process are not yet performed, therefore, no experimental data is included. It is hoped that this will be one of the future steps to take on this research project.

6.3 Summary

In this chapter, single crystal Ni was used as an attempt to improve the thickness uniformity of the graphene films. Ni(111) was used successfully to produce 1 LG over large areas on a dielectric substrate. This is thought to be possible due to the

thermodynamic distinction between a graphene monolayer and graphite on Ni(111) during segregation. Quenching of the Ni(111) surface during segregation allows freezing the surface with 1 LG before the nucleation of graphite. Other crystal orientations are expected to grow only multilayer graphene based on the observations made by Blakely et al. [47, 82, 83, 84, 85] where no phase separation exists between one layer and graphite. However, confirmation of this hypothesis should be undertaken experimentally in the future.

Chapter 7

Discussion on the effect of grain boundaries, surface roughness and cooling rate on F-LG precipitation

A complete description of the formation of the F-LG films would require the determination of the nucleation rate of 1-LG and F-LG at each location on the Ni surface and the growth rate of each nucleus. The two of these variables should also be known as a function of time during the cooling process. However, the lack of in-situ tools compatible with ambient pressure processes limits the current analysis to theoretical considerations.

For simplicity purposes this analysis is first focused on the effect of grain boundaries and surface roughness on the nucleation rate of islands of graphene layers. The dependence of nucleation rate on surface roughness and grain boundaries is considered in the first section of this chapter. Growth rate of 1-LG and F-LG islands and the effect of cooling rate are considered in the following section.

7.1 Grain boundaries, roughness and their role in F-LG nucleation rate

Nucleation rate can be defined as the number of graphene islands forming per unit time and per unit area on the surface of the Ni film. In chapter 4 it was shown that F-LG grows preferentially at grain boundaries. Furthermore, on single crystal Ni(111), F-LG also grows only at scratches left by polishing of the surface. This occurs at conditions where the Ni-C solution is quenched from 1000 ^{o}C at fast cooling rates of $\geq$100 ^{o}C min^{-1}. Considering such observations, the surface of the Ni film can be viewed to be formed by steps and terraces. Here, the Ni surface roughness and curvature is considered to be composed of steps and terraces due to the crystallinity of the Ni films and substrates (Figure 7-1(a-b)). Under this picture, the density of steps should change with local changes of curvature and roughness which characterize grain boundary grooves (Figure 7-1(c-d)). Under this simple surface picture, there would be more free energy available for nucleation of graphene islands at the edges of the Ni steps, therefore, enhancing the nucleation rate of graphene islands at grain boundaries and scratches. Sites such as free step edges enhance primarily the nucleation of graphene islands during growth. The following analysis is aimed towards giving a qualitative description of the role of the preferential nucleation of graphene at the Ni surface steps in the formation of F-LG on the Ni surface.

The nucleation rate in classic nucleation theory can be expressed by [90]:

$$\dot{N} = fn\exp(-\frac{\Delta G^*}{kT}), \tag{7.1}$$

where f is the atomic jump frequency (time^{-1}), n is the density of nucleation sites (sites$\times$area^{-1}) and ΔG^* is the nucleation barrier, or the energy required to creat a stable nucleus. Two nucleation events are considered, one refers to the creation of a graphene island on the free surface of Ni and the second refers to the creation of a graphene island at the edge of a Ni step (Figure 7-2). The ratio of the nucleation barrier is estimated in the following analysis and the preferential nucleation of graphene

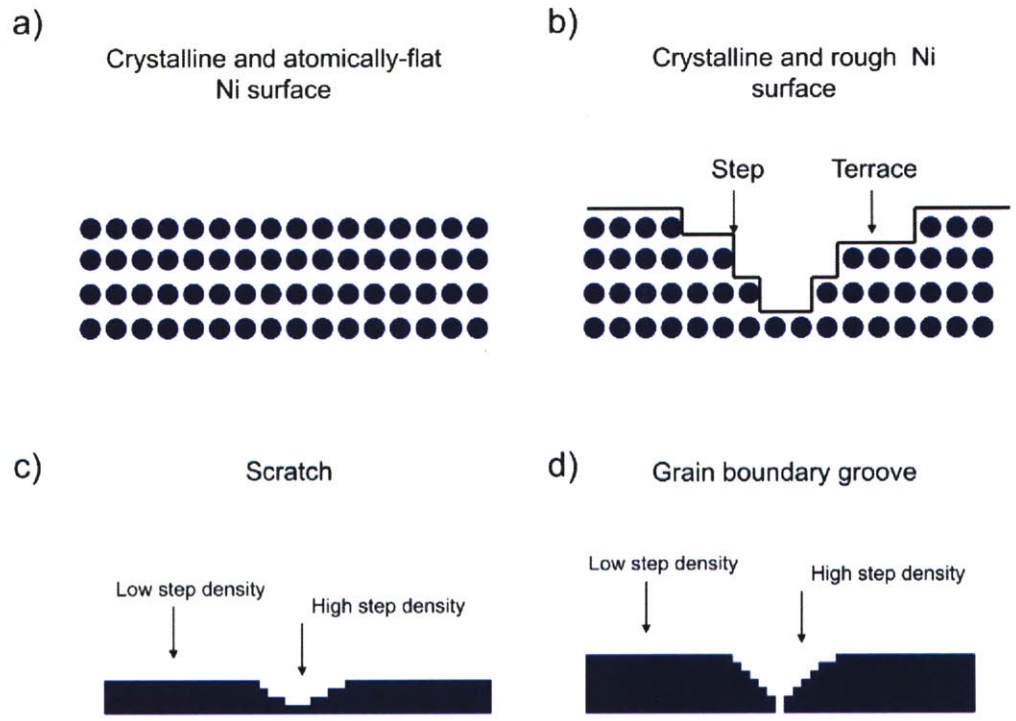

Figure 7-1: Surface of atomically flat and rough crystalline surfaces.
a) Atomically flat surface. b)Roughness on a crystalline surface. Steps and terraces compose the rough crystalline surface. c)Steps near a scratch on a crystalline surface. d) Steps near the grain boundary of a polycrystalline surface.

on a Ni step should be reflected by a lower nucleation barrier on the step.

The difference in Gibbs free energy of the precipitation of a graphene layer on the graphene surface can be divided into two terms. One of them is the change of free energy related to the transformation of the graphite phase and the second is related to the energy spent by creating new interfaces and free edges due to the new nucleus:

$$\Delta G = \Delta G_t + \Delta G_i, \tag{7.2}$$

where ΔG_t and ΔG_i are the transformation and interface free energy change. This former term is negative since for a given undercooling of the Ni-C solution (how much the solution is cooled below the carbon saturation temperature), the system. The latter is positive due to the creation of a new nucleus interface or edge. Graphene islands are approximated by circles and half circles for the free surface and step edge nucleation cases, respectively(Figure 7-2). For the free surface nucleation event (Figure 7-2(b)), away from any step edge, the change in total free energy is:

$$\Delta G_{surface} = \Delta G_p(\pi r^2) + \gamma_g(2\pi r). \tag{7.3}$$

where ΔG_p is the change in Gibbs free energy per unit area of a nuclei and γ_g is the free energy of the graphene island. For the step edge nucleation event (Figure 7-2(c)), the change in total free energy is described by:

$$\Delta G_{step} = \Delta G_p(\frac{\pi r^2}{2}) + \gamma_g(\pi r) + \Delta\gamma_{Ni-g}(2r), \tag{7.4}$$

where $\Delta\gamma_{Ni-g}$ is the difference energy of the Ni step edge and the energy of the Ni-C interface created. Notice that the difference between the two cases is the energy of the graphene edge being formed at the Ni step and which is represented by $\gamma_{Ni-g}(2r)$. The energy required to form the Ni-graphene interface is expected to be lower than the energy required to form a free Ni edge. This is due to the stabilization of both carbon and nickel dangling bonds [91]. The total free energy of a nucleus of a given radius is dependent on two competing phenomena, the energy gained due to the precipitation process ($\Delta G_p \times Area \leq 0$) and the formation of edges ($\gamma \times$perimeter≥ 0). Plotting the

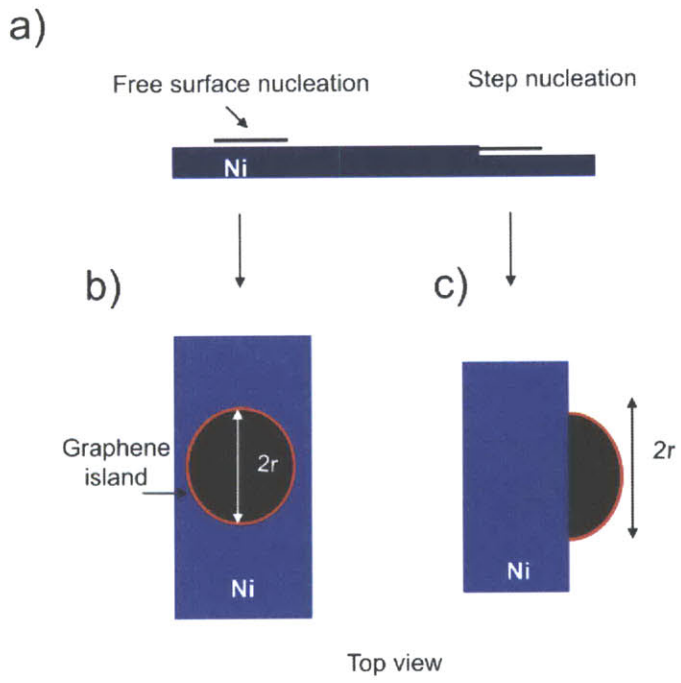

Figure 7-2: Two nucleation events.
a)Cross-sectional view of graphene islands nucleating at a free Ni surface and at a Ni step. b-c) Top view of the two types of nucleation events.

total energy for both cases as a function of the radius of the nuclei results in plot such as that shown in Figure 7-3. At small values of r, the change in energy is positive and after a critical value of r, the total energy decreases with increasing radius. Only nuclei with radius larger than this critical radius (r^*) can therefore grow and these are referred to as critical nuclei. The critical radius is the radius value at which $\frac{d\Delta G}{dr} = 0$. The energy barrier for nucleation is the change in energy corresponding to the formation of a critical nucleus ($\Delta G^* = \Delta G(r^*)$). Deriving equations 7.3 and 7.4, it is possible to obtain the critical radius for both cases:

$$r^*_{surface} = -\frac{\pi\gamma_g}{\Delta G_p} \qquad r^*_{step} = -\frac{\pi\gamma_g + 2\gamma_{Ni-g}}{\pi\Delta G_p}, \tag{7.5}$$

and substituting these in equations 7.3 and 7.4, the corresponding nucleation barriers are:

$$\Delta G^*_{surface} = -\frac{(\pi\gamma_g)^2}{\Delta G_p} \qquad \Delta G^*_{step} = -\frac{(\pi\gamma_g + 2\gamma_{Ni-g})^2}{\pi\Delta G_p}, \tag{7.6}$$

and the ratio between the two nucleation barriers becomes:

$$\frac{\Delta G^*_{edge}}{\Delta G^*_{surface}} = \frac{\pi\gamma_g + 2\gamma_{Ni-g}}{\pi^3\gamma_g^2}. \tag{7.7}$$

Using theoretical values for the free graphene edges and graphene-Ni interface, it is found that $\frac{\Delta G^*_{step}}{\Delta G^*_{surface}} \approx 0.42$, confirming that under the above treatment nucleation of graphene at the edge of Ni steps will always be more favorable. Using, equation 7.1, the expression relating the relative nucleation between the two cases is:

$$\frac{\dot{N}_{step}}{\dot{N}_{surface}} = \frac{n_{edge}}{n_{surface}} \exp\left(\frac{\Delta G^*_{surface} - \Delta G^*_{step}}{kT}\right). \tag{7.8}$$

Now, the density of nucleation sites is considered for both cases. Consider the surface near a grain boundary which shows certain curvature so that an angle is formed between the surface normal and the normal of the terraces (consider the terraces to be the Ni(111) direction). Such a surface is shown in Figure 7-4(a). Closer to the center of the boundary, the surface curvature increases as well as the angle between

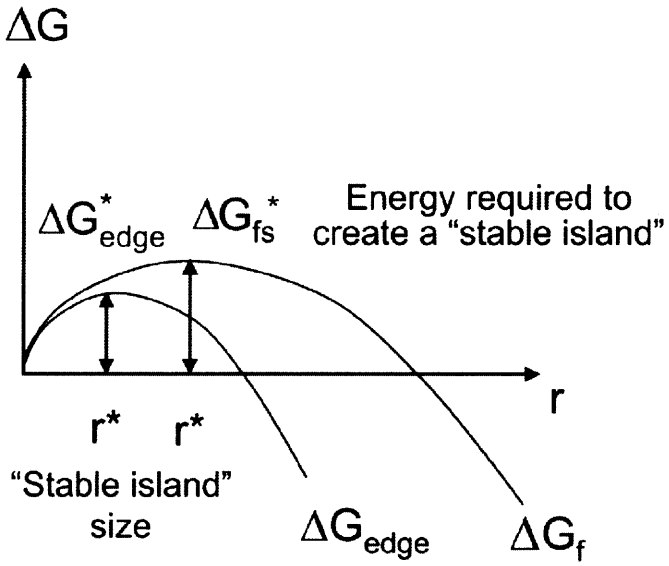

$$\Delta G^*_{edge} < \Delta G^*_{fs}$$

Figure 7-3: ΔG as a function of the graphene island radius for nucleation events at the free Ni surface or at a Ni step.

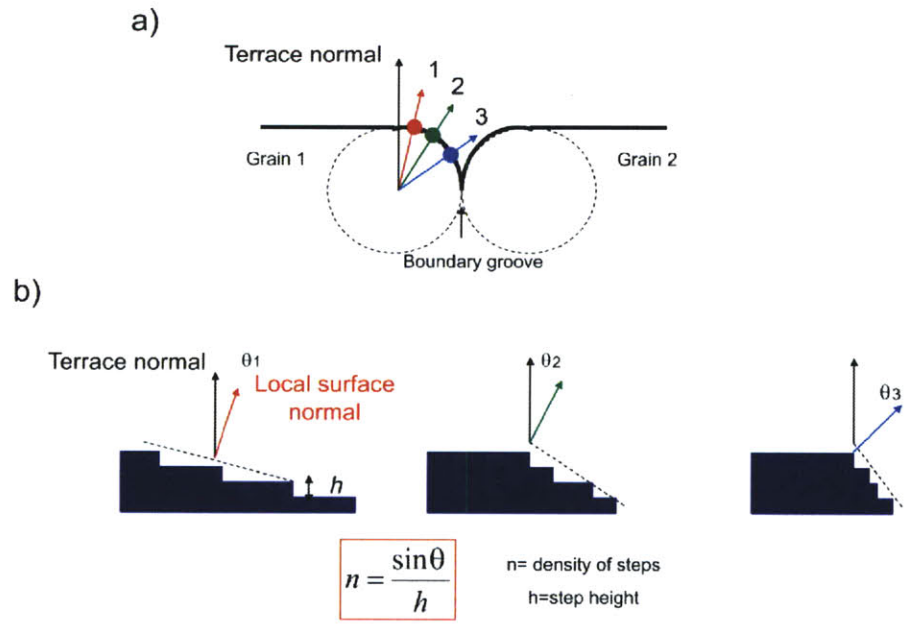

Figure 7-4: Change in step density with curvature close to a grain boundary a)Cross-sectional view of a grain boundary. The black arrow represents the normal of the terraces. Colored arrows represent the local surface normal. b)Illustration of the changes in step density. Closer to the grain boundary, the angle between the local surface normal and the terrace normal (θ) increases. The density of steps is a function of θ and increases closer to the grain boundary as illustrated.

the surface normal and the normal of the terraces (Figure 7-4(b)). It is possible to show that the local step density per unit length is proportional to:

$$n_{step} = \frac{\sin\theta}{h}, \tag{7.9}$$

where h is the Ni step height.

Here, the density of nucleation sites is defined with units of inverse length instead of inverse area. This unit convention will be adopted for simplicity and in order to be compatible with a cross-sectional view of the Ni surface.

So far, two considerations have been made; one is the preferential nucleation of graphene on Ni steps and the increased density of steps close to a grain boundary. The implications of these two factors on the growth of F-LG can be understood after considering the Ni surface after a time t of island growth on the stepped surface near

the boundary. This is depicted in Figure 7-5. After nucleation of stable islands has started, it is expected that a higher density of sable islands will be available close to the grain boundary (Figure 7-5(a)). The density of steps increases, therefore, for a constant nucleation barrier at the Ni edges, a higher density of stable nuclei should be found near the grain boundary. Therefore, the mean distance between stable islands increases near the boundary. In order to appreciate the effect of an increased nucleation rate near the boundary, let's assume a constant growth rate for each of the islands and neglect the time scale for which the growth rate can be maintained. The fact that the mean distance between islands decreases close to the boundary could lead to the overlap of each graphene layer growing after a time t, resulting in the formation of F-LG near the boundary (Figure 7-5(b)). The probability of two islands overlapping depends on the distance between them, which is inversely proportional to the density of nucleation sites.

In the following sections, the temperature dependence of nucleation rate and growth rate is considered. This is relevant in order to begin to consider the effect of the amount of cooling during the graphene growth process. This again is only an attempt to qualitatively describe the growth of graphene near the Ni grain boundaries.

7.2 The temperature dependence of nucleation rate

To consider the temperature dependence of nucleation rate, it is necessary to analyze each term in equation 7.1; the atomic jump frequency, the density of nucleation sites and the exponential term which depends on the nucleation barrier. Assuming that the density of nucleation sites is independent of temperature, the following analysis will focus on the nucleation barrier and the atomic jump frequency.

The nucleation barrier for step nucleation (equation 7.6) is inversely proportional to the change in the Gibbs free energy due to the graphene formation. This change in free energy is temperature dependent. It is possible to estimate this change in energy as a function of the undercooling below the solubility limit of carbon in Ni.

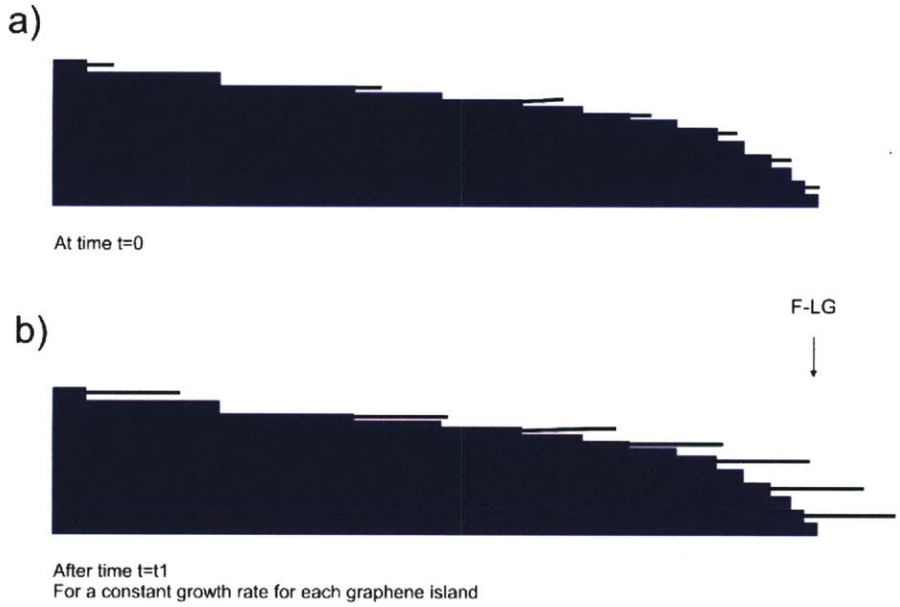

Figure 7-5: Graphene growth and the step density close to a grain boundary. a)Cross-sectional view of the Ni surface close to a grain boundary just after several nucleation events have occurred. Equal nucleation rate per step is assumed and is proportional to $f \exp(\frac{-\Delta G^*}{kT})$. Only the density of steps n changes closer to the grain boundary and therefore, the number of graphene islands. Due to the increase in number of graphene islands, the mean distance between islands increases closer to the boundary. b) Cross-sectional view of the surface after growth of the nucleated islands and after a time t_1. A constant growth rate is assumed. Close to the boundary, F-LG formation could be caused by the overlap of islands growing close to each other. The probability of F-LG formation based on this mechanism should be expected to be larger close to the boundary with respect to that of the surface away from the boundary.

The Gibbs free energy at a temperature T for carbon in solution and carbon in the graphene phase is:

$$G_s = H_s - TS_s \quad G_g = H_g - TS_g, \tag{7.10}$$

where G, H and S are the Gibbs free energy, enthalpy and entropy of carbon in solution (s) and in graphite (g). The change in Gibbs free energy due to graphene formation:

$$\Delta G_p = H_g - H_s - T(S_g - S_s) = \Delta H_p - T\Delta S_p. \tag{7.11}$$

At the saturation temperature, the Gibbs free energy of carbon in solution and carbon in graphene are equal, therefore:

$$G_s(T_{sat}) = G_g(T_{sat}) \qquad H_s(T_{sat}) - T_{sat}S_s = H_g(T_{sat}) - T_{sat}S_g(T_{sat}), \tag{7.12}$$

and

$$S_g(T_{sat}) - S_s(T_{sat}) = \Delta S(T_{sat}) = \frac{H_g(T_{sat}) - H_s(T_{sat})}{T_{sat}} = \frac{\Delta H(T_{sat})}{T_{sat}}. \tag{7.13}$$

Assuming that ΔS and ΔH are temperature independent and combining equations 7.13 and 7.11, it is possible to obtain the change in Gibbs free energy as a function of temperature:

$$\Delta G_p = \Delta H \frac{\Delta T}{T_{sat}}. \tag{7.14}$$

Combining the above expression and the step nucleation barrier expression in 7.6 gives the dependence of the nucleation barrier with undercooling ΔT:

$$\Delta G^*_{step} = -\frac{(\pi\gamma_g + 2\gamma_{Ni-g})^2 T_{sat}}{\pi \Delta H \Delta T}. \tag{7.15}$$

The nucleation barrier is inversely proportional to the undercooling ΔT. Therefore, the barrier decreases with decreasing cooling rate. The exponential term in the nucleation rate equation ($exp(\frac{-\Delta G^*}{kT})$), which corresponds to the potential fraction of nuclei increases with decreasing temperature (increasing undercooling). The meaning of this is that graphene precipitation is favored thermodynamically as the temperature decreases. However, the jump frequency f, which determines how frequently a critical nucleus can receive a carbon atom from the Ni-C solution, is also a thermally activated process where:

$$f = \omega \exp(-\frac{\Delta G_m}{kT}), \tag{7.16}$$

where ω is a constant and ΔG_m is the activation energy for atomic migration and can be assumed to be constant with temperature. Atomic migration, therefore, should decrease with temperature and undercooling. Considering the two terms which are temperature dependent in the nucleation rate equation; f and $exp(-\frac{\Delta G^*}{kT})$, the form of the nucleation rate as a function of temperature should have a qualitative form such as the one shown in Figure 7-6. Notice that the nucleation rate increases as the temperature is lowered below that of saturation. At temperatures close to the saturation temperature, the nucleation rates is low due to a small value of ΔG_p and a large value of ΔG^*_{step}. A maximum in nucleation rate is expected at intermediate temperatures after which the nucleation rate falls down again due to the lack of thermal energy to activate atomic migration.

In the following section, the temperature dependence of growth rate will be considered.

7.3 The temperature dependence of growth rate rate

In order to describe the growth rate as a function of temperature, a diffusive growth view is assumed. This is one of the simplest growth models use to describe the growth

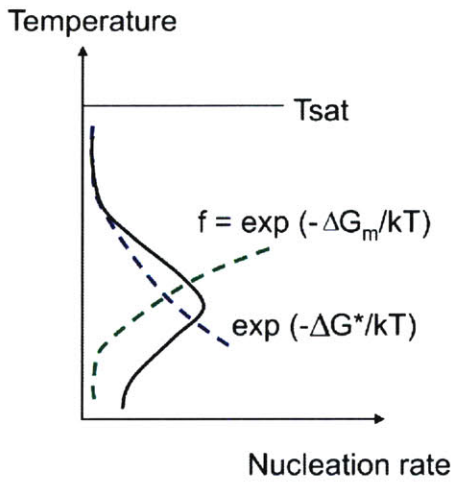

Figure 7-6: Nucleation rate as a function of temperature.

of precipitates in phase transformations. For a circular island of graphene to increase its radius with an increment of dr, a differential of area $2\pi r dr$ of carbon atoms should be added to the island from the surrounding Ni surface. The total amount of carbon per unit length of the island circumference that is supplied is:

$$dN = (C_{graphene} - C_{Ni})dr, \tag{7.17}$$

where $C_{graphene}$ and C_{Ni} are the carbon concentrations for the graphene island and the Ni surface, respectively. The concentration of carbon atoms is given in units of atoms per unit area. The flux of carbon atoms per unit area in a unit time dt can be obtained from Fick's second law of diffusion:

$$dN = Jdt = D(\frac{dC}{dr})dt, \tag{7.18}$$

where D is the diffusion coefficient of carbon on the Ni surface and J is the flux of carbon atoms per unit time and unit length. Equating the two last expressions, the growth rate is given by:

$$\nu = \frac{dr}{dt} = \frac{D}{C_{graphene} - C_{Ni}} \frac{dC}{dr}. \tag{7.19}$$

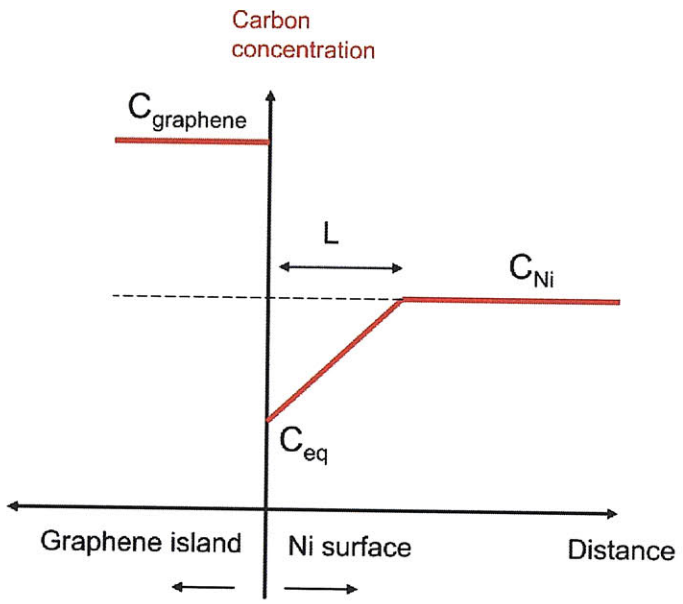

Figure 7-7: Approximation of the carbon concentration profile at the interface between a graphene island and a Ni surface.

In order to obtain an expression of growth rate that is only dependent on the concentrations, island radius and the diffusion coefficient, it is needed that an estimate of the concentration profile $\frac{dC}{dr}$ near the graphene island is given. For this, the concentration profile is first approximated to a linear profile such as that shown in Figure 7-7. Conservation of mass requires that the carbon concentration gained by the graphene island due to growth is equal to the carbon concentration depleted around the island (depletion distance L in Figure 7-7):

$$(C_{graphene} - C_{Ni}) = \frac{(C_{Ni} - C_{eq})L}{2}, \tag{7.20}$$

where C_{eq} is the equilibrium concentration between the graphene island and the Ni surface which can be extracted from the solubility curve of carbon in Ni. From this, the following is obtained:

$$\frac{dr}{dt} = \frac{D}{2r}\left(\frac{\Delta C_o}{C_{graphene} - C_{Ni}}\right)^2, \tag{7.21}$$

where $\Delta C_o = C_{Ni} - C_{eq}$. This is the difference between the concentration of carbon

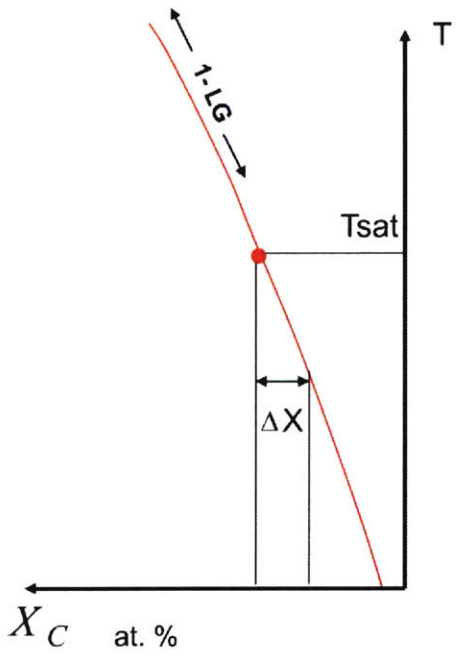

Figure 7-8: Solubility curve of carbon in Ni. ΔX_O increases with decreasing temperature.

atoms on the surface of Ni, which for now can be assumed to be equal to the concentration in the bulk, and the concentration of carbon atoms in equilibrium with the graphene islands. This difference can be obtained from the solubility curve of carbon in Ni as shown in Figure 7-8. Integrating equation 7.21 to obtain an expression for r and afterwards deriving $\frac{dr}{dt}$, the growth is found to be:

$$\frac{dr}{dt} = \frac{\Delta C_o}{(C_{graphene} - C_{Ni})}\sqrt{\frac{D}{t}}. \tag{7.22}$$

With this growth rate expression, it is possible to derive qualitatively the expected behavior of growth rate as a function of temperature. For this, the temperature dependence of ΔC_o and the diffusion coefficients is needed. It is assumed that $C_{graphene}$ is much larger than C_{Ni}. The former is ≈100 at. % (1 carbon atom per Ni atom corresponds to a graphene layer over Ni(111)) and the latter is close to 1 at. %. ΔC_o changes depends logarithmically with $(\frac{1}{T})$ given by equation 6.5, therefore, this term which represents the concentration of carbon out of equilibrium due to the undercooling increases with decreasing temperature. Diffusion is a thermally activated process

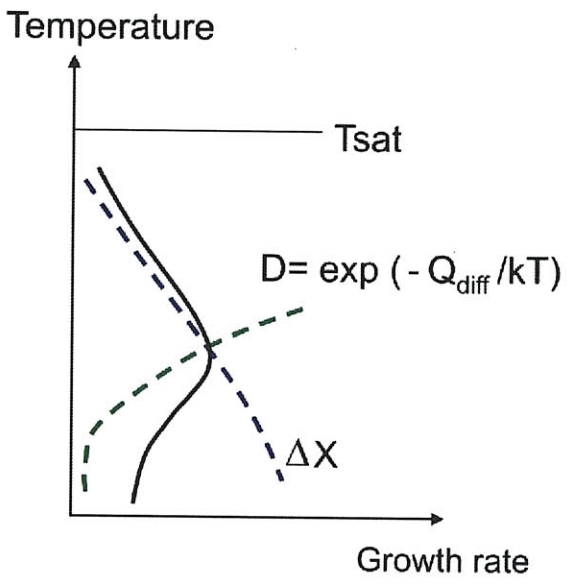

Figure 7-9: Growth rate as a function of temperature.

with the form:

$$D = D_o \exp(-\frac{Q}{kT}), \tag{7.23}$$

where D_o is a constant and Q is the activation energy for diffusion. Therefore, the diffusion term in the growth rate expression in equation 7.22 should decrease with decreasing temperature. The effect of the behavior of these two terms with temperature is shown in Figure 7-9. Due to the competition between D and ΔC_o, the growth rate should behave similarly to nucleation rate with temperature. At small deviations from the saturation temperature, ΔC_o is close to zero, therefore the growth rate is negligible. At intermediate temperatures, both ΔC_o and D are significant, therefore the growth rate reaches a maximum. At lower temperatures, although the oversaturation ΔC_o is high, D is low due to the decrease in temperature.

7.4 The combined effect of nucleation rate and growth rate as a function of changes in temperature

Now that the behavior of nucleation rate and growth rate as a function of temperature has been described, it is possible to develop a qualitative description of graphene growth on polycrystalline Ni or rough crystalline Ni surfaces. The temperature dependence of nucleation and growth rate is helpful as a starting point in the incorporation of the effect of cooling rate in the description of graphene growth on these type of surfaces.

Here, the rate of cooling is not considered. A discrete step of temperature change, ΔT, is considered as a first approach to the problem and in order to simplify the description. Future work should include the magnitude of the rate of cooling.

Figure 7-10 and 7-11 shows the effect of having a small ($\Delta T << T_{sat}$) and a large degree of undercooling ($\Delta T < T_{sat}$), respectively. Notice that both nucleation and cooling rate behave similarly as a function of temperature. That is, both rates are low close to the saturation temperature (small undercooling) and both of them increase as the amount of undercooling increases. The fact that both, nucleation and growth rate increase or decrease at the same time is expected to have a significant effect on the amount of graphene layers growing close to the grain boundaries.

For small amounts of undercooling (Figure 7-10), the nucleation rate of graphene islands growing on the Ni steps is small, therefore the mean distance between islands increases. The growth rate should also be expected to be low. The combination of both low nucleation and growth rate decreases the probability of having graphene islands overlapping during growth at the grain boundaries. On the other hande, when the amount of undercooling is increased and is closer to the maximum of nucleation and growth rate (Figure 7-11), the combination of large nucleation and growth rates increases the probability of having graphene islands overlapping during growth at grain boundaries. This picture may guide future work on the explanation of the mor-

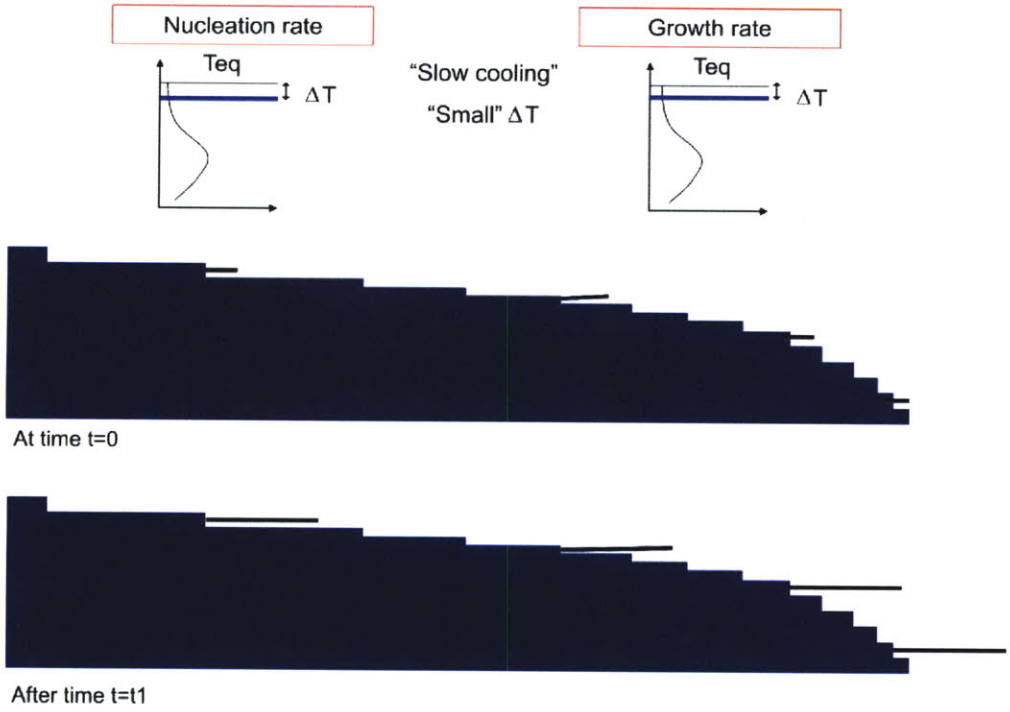

Figure 7-10: Effect of nucleation and growth rate for $\Delta T << T_{sat}$.
Both nucleation and growth rate are small. The nucleation rate defines the number of graphene islands and therefore, the mean distance between them. Assume at time $t = 0$ islands that have been nucleated start growing. At time $t = t_1$, the islands have grown a specific length corresponding to the growth rate at the given temperature. Growth rate is expected to be small. The combined effect of decreased mean distance between islands and low growth rates decreases the probability of graphene island overlap and F-LG formation.

phology of the graphene films obtained with varying cooling rates. For the first case described above, it can be expected that grain boundary saturation with multilayer is minimized while for the second case, it is enhanced.

The analysis here presented only represents a starting point towards future analysis. Future research along this line would benefit significantly from in-situ techniques that could help quantify nucleation and growth rate. However, as mentioned earlier, this presents a challenge due to the fact that graphene growth in this work occurs in ambient pressure.

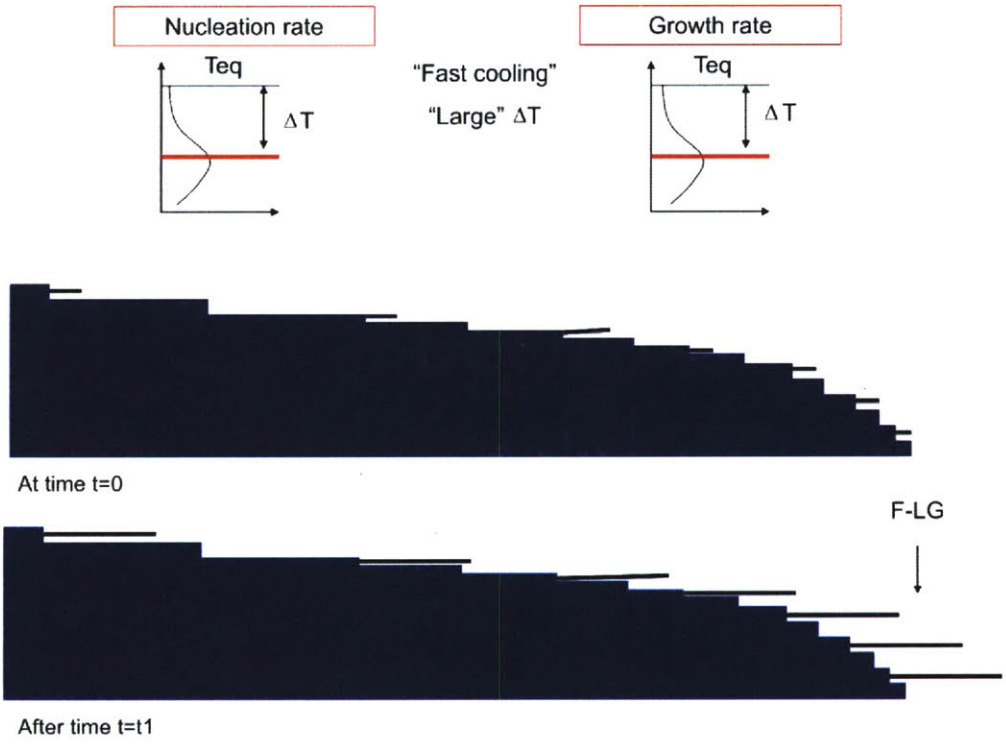

Figure 7-11: Effect of nucleation and growth rate for $\Delta T < T_{sat}$.
Both nucleation and growth rate are larger compared to small undercoolings. The nucleation rate defines the number of graphene islands and therefore, the mean distance between them which also becomes larger. Assume at time $t = 0$ islands that have been nucleated start growing. At time $t = t_1$, the islands have grown a specific length corresponding to the growth rate at the given temperature. Growth rate is expected to be also larger. The combined effect of an increased mean distance between islands and low growth rates decreases the probability of graphene island overlap and F-LG formation.

7.5 Summary

The last four chapters focused on the growth of graphene on polycrystalline Ni and single crystal Ni surfaces. The effect of the substrate and cooling rate in the process was described. In the following chapter, the last one of this thesis, the structural characterization of 2-LG and F-LG derived from the process presented will be described. The characterization is carried using Raman spectroscopy and electron diffraction.

Chapter 8

Structural Characterization: Raman Spectroscopy and Electron Diffraction

In the last four chapters, a process to produce F-LG films and the effects of the process parameters were discussed. In the present chapter, Raman spectroscopy and electron diffraction are used as means to understand better the structure of the film. Specifically, these techniques are used in order to determine the nature of the stacking of the graphene layers in the film.

Characterizing the stacking order of the F-LG sections of the films is relevant due to expected changes in the electronic structure of F-LG depending on the nature of the layer stacking. For the case of 2-LG, the AB stacking or Bernal stacking of the layers induces the inequivalence of both atoms of the unit cell of each graphene layer. This inequivalence is reflected in the alteration of the electronic energy of the π orbitals of the carbon atoms, producing two conduction and two valence bands. Furthermore, the electronic energy of the π bands of 2-LG are no longer linearly dependent with the electron momentum k, decreasing the effective mass of the electrons with respect to those in 1-LG. Deviations from AB stacking of 2-LG or changing the orientation between the two graphene layers is expected to change significantly the scenario described above. For example, in chapter 2 it was discussed that graphene

layers growing on SiC are stacked in a way that each graphene is misoriented around 30^o with each other. It is thought that such misorientation explains why samples with multilayer graphene (5-10) layers show high mobilities with characteristics of highly doped 1-LG [36]. The absence of AB stacking in F-LG brings back the equivalence of the two carbon atoms of the unit cell of each graphene layer, therefore, making each layer behave electronically as two independent 1-LG pieces. Therefore, in this chapter, the structural characterization presented is devoted to determine the absence or presence of AB stacking in our F-LG pieces. This is done by using Raman spectroscopy and electron diffraction. This structural characterization is expected to be valuable to future device performance and characterization using this material.

In the first two sections, an overview of Raman spectroscopy in graphene is given. In the last section, Raman and electron diffraction measurements on the F-LG films are presented with a description of the behavior of the layer stacking in the films.

8.1 Raman Spectroscopy

Raman spectroscopy is a technique used to study vibrational and rotational modes in crystals and molecules. Its discovery is attributed to Sir Chandrasekhara Venkata Raman. It relies on the inelastic scattering of monochromatic light. In a solid, the scattering occurs due to the interaction with vibrational modes of the crystalline structure formed by the atoms. This interaction shifts the frequency of the scattered light with respect to the incoming light. The Raman effect can be understood classically considering the polarization of the crystal by the local electric field created by the light where [92]:

$$\vec{P} = \alpha \cdot \vec{E}, \tag{8.1}$$

in which $\vec{P}$ is the polarization vector describing the displacement between positive and negative charges due to the applied electric field, $\vec{E}$ and α is the polarizability tensor of the atom in the crystal in question. $\vec{E}$ is the electric field and it has the form of $\vec{E} = \vec{E_o} \sin \omega_o t$. Under this classical description [92], the polarizability of the

material is assumed to be modulated by the vibration of the lattice so that:

$$\alpha = \alpha_o + \alpha_1 \sin \omega_q t, \tag{8.2}$$

where ω_q is the frequency of the atomic vibration coupled to the incoming light. Therefore, the polarization induced in the crystal becomes:

$$\vec{P} = \vec{E_o}\,(\alpha_o + \alpha_1 \sin \omega_q t)\cdot \sin \omega_o t = \vec{E_o}\left(\alpha_o \sin \omega_o t + \frac{1}{2}\alpha_1 \cos(\omega_o - \omega_q)t - \frac{1}{2}\cos(\omega_o + \omega_q)t\right). \tag{8.3}$$

This final expression of the polarization shows that light can be scattered both elastically (first term in 8.3) and inelastically by a downshift (second term) and an upshift (third term) in frequency. A downshift in frequency is referred to as the Stokes Raman shift and an upshift in frequency as the Anti-Stokes Raman shift. The former refers to the emission of a phonon and the latter to the absorption of a phonon in the scattering process. Energy and momentum conservation gives the following restrictions to the Raman process:

$$E_s = E_i + E_q \quad and \quad \vec{k_s} = \vec{k_i} + \vec{k_q} \tag{8.4}$$

where E and k are the energy and momentum, respectively, of the incident (i) and scattered (s) light and the vibration or phonon mode (q) involved.

The order of the Raman process refers to the number of scattering events involved. Processes involving one and two scattering events are first and second order, respectively. For first-order processes, the momentum of the vibration mode is $q \approx 0$. This is because the momentum of the scattered and incident light ($k = 2\pi/\lambda$), typically in the visible range, will be very small compared to the Brillouin zone of most materials ($2\pi/a$, a =lattice constant). In second-order processes, it is possible to probe vibration energies with a finite momentum since it would be possible to accommodate the scattering of two modes with equal momentum magnitudes but opposite sign in order to comply with the restriction in equation 8.4. This type of second-order process

will be described in more detail in the next section for the case of graphene. Raman spectra are usually represented in an intensity vs. Raman shift plot. The latter is included in wave number units of cm^{-1}.

The classic description of Raman processes is helpful in understanding the frequency shifts of the scattered light with respect to the incident light. However, in low dimensional systems and graphene, the existence of discrete transition energies for electrons enhances the scattered Raman signal since these transitions increase the probability of the electron-phonon interactions. Resonance Raman processes refer to those that occur when the energy of the incident and scattered light coincide with an electronic transition in the material of interest. Under this picture one is to consider a quantum view of the Raman process. This is relevant in the quantitative Raman characterization of nanostructures such as nanotubes with well-defined electronic transitions. A schematic representation of a first order Raman process is depicted in Figure 8-1. The lines represent electronic states within a material system. The incoming light excites electrons from the lower state to the one with a higher energy (incident resonance). The electron then loses energy and occupies a virtual state due to the emission of a phonon (Stokes process). Finally, the electron recombines with its initial state emitting a photon. The difference between the energies of the incident and scattered photons correspond to the phonon involved in the scattering process. The electronic transition can also occur between a real and virtual state so that the emission of a phonon brings the electron to the upper real state before recombining to its original state. In this case, the process is in resonance with the scattered light (scattering resonance). Figure 8-2 describes first-order and second-order Raman processes for incidence and scattering resonance. The crosses represent the electronic energy levels on a energy vs. wave vector plot. Second-order processes can be divided into two-phonon processes (two phonons with equal momentum magnitude but opposite sign) and one-phonon processes. In the latter case, one of the scattering events is elastic such as the interaction of an electronic state with a defect. The quantification of the scattered Raman signal necessitates the consideration of the interaction between the incident photon and electrons and between electrons and

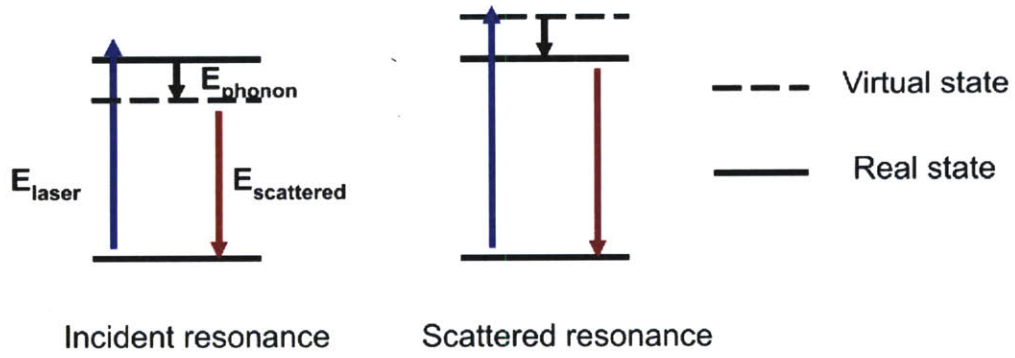

Figure 8-1: Representation of incident and scattered resonance Raman processes. Only the Stokes case (emission of phonon) is shown.

phonons in the crystal lattice. These are described by the electron-light and electron-phonon interaction Hamiltonians [92]. These considerations are beyond the scope of the work presented here and will not be discussed in detail.

In the following section, the Raman processes for graphene are discussed. Emphasis will be given in the application of Raman spectroscopy in the identification of number of graphene layers and the determination of the electronic structure of single- and bi-layer graphene.

8.2 Raman Spectroscopy of Graphene

In this section, the Raman spectra of single- and few-layer graphene are discussed. Before presenting the characteristics of the spectra of this material, it is necessary to introduce the electronic structure of the system as well as its phonon dispersion. These are relevant since the electronic and phonon properties will determine the behavior of the Raman peaks observed.

Under a tight binding description of the graphene lattice with two atoms per unit cell, A and B (see chapter 2), the electronic dispersion of the electrons occupying the π bands follows [94]:

$$E_{\pm}(k) = \pm t\sqrt{1 + 4\cos\left(\frac{\sqrt{3}k_x a}{2}\right)\cos\left(\frac{k_y a}{2}\right) + \cos^2\left(\frac{k_y a}{2}\right)} \tag{8.5}$$

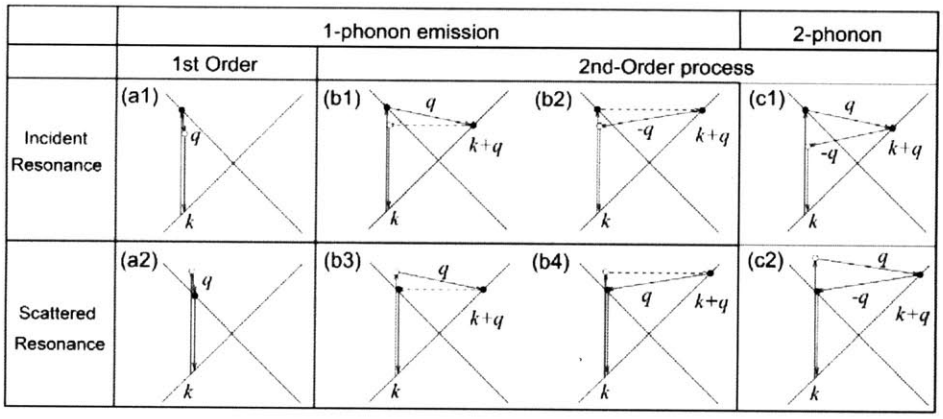

Figure 8-2: First-order and second-order Raman processes in a momentum vs. energy plot.
Incident and scattered resonance are shown. The order of the process refers to the number of scattering processes occurring. Second-order processes can be divided in one-phonon and two-phonon cases. One-phonon processes involve one elastic scattering event (b1-b4) which is a defect scattering process, whereas two-phonon ones involve two phonons with equal wave vector magnitude but opposite direction. From ref [93]

where E_+ and E_- refer to the conduction and valence π bands of the electrons. k is the wave vector, a the lattice constant and t is the nearest neighbor overlap energy. Figure 8-3 shows the two dimensional energy dispersion for the π electrons in graphene in the first Brulluoin zone of the lattice. Figure 8-3(b) shows the first Brilluoin zone identifying the Γ, M and K points of the reciprocal lattice. Near the K point (k_x=0 and k_y=$2\pi/3a$), the energy depends linearly on the momentum k. Because the structure has two atoms in the base, for each K point, there is a K' point with a similar electronic dispersion.

There are six types of vibration modes in the graphene structure ($3N$, N=number of atoms in the unit cell). Three of them are acoustic (A) and three of them are optical (O). Two of the modes are out-of-plane (o) while the rest are all in-plane (i). Longitudinal phonons (L) are those in which the movement is directed along the C-C bond of the structure. Transverse phonons (T) are those in which the atomic movement is directed perpendicular to the C-C bond. Figure 8-4 shows the phonon dispersion for each of the six branches [93](LA, oTA, iTA, LO, oTO, iTO).

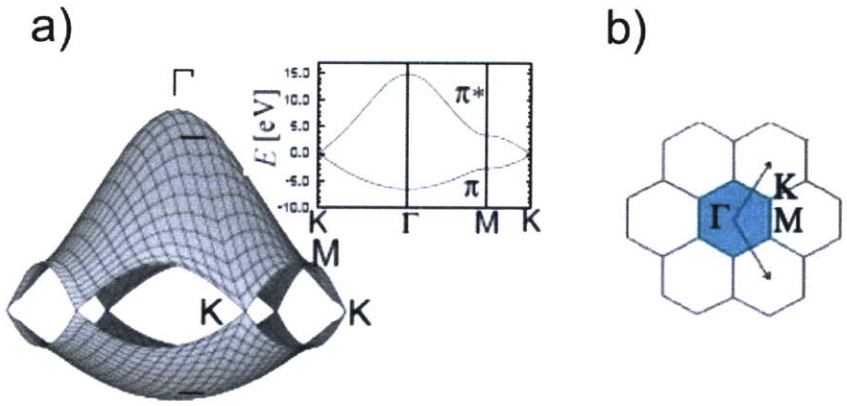

Figure 8-3: Electronic structure of graphene.
a)Electronic energy as a function of electron wavevector (k). The energy-k relation is linear near the K point (inset). b)Reciprocal space of graphene showing the first Brullouin zone with the symmetry points Γ, M and K. From ref [92]

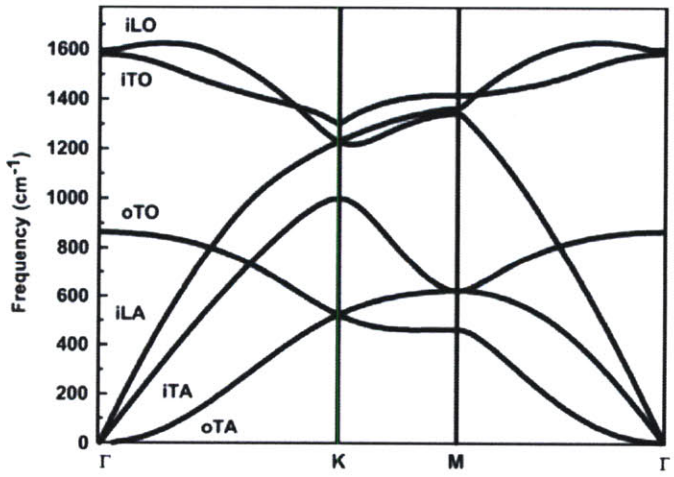

Figure 8-4: Dispersion of the six phonon branches in graphene.
L=longitudinal, T=Transverse, O=optical, A=Acoustic, o=out of plane and i=in plane. From ref [93]

The Raman spectra of graphene related materials show three prominent peaks (Figure 8-5; the G band at $\approx$1580 cm^{-1}, the D band at $\approx$1350 cm^{-1} and the G$'$ at $\approx$2700 cm^{-1}. The G band is the only one arising from a first-order Raman process. It involves the degenerate iTO and LO modes with $q \approx 0$ at the Γ point of the Brullouin zone. The D and G$'$ peak are second-order Raman processes. They involve two scattering events. The D band occurs by the scattering of one iTO phonon and by the elastic scattering with a defect (2nd order, one-phonon process in Figure 8-2), therefore, occurs in defective graphene materials. The G$'$ band occurs by the scattering of two iTO phonons with opposite directions of their wave vector (2nd order, two phonon process in Figure 8-2). In both processes, two of the electronic states are real and one is virtual. The intermediate state is always real giving rise to two possible resonant processes (incident and scattered) as discussed before. Because these processes involve two real states and are resonant they are referred to as double resonance Raman scattering (DRRS). The D and G$'$ bands show a frequency dependence with the laser energy used for excitation. This is because the phonon wave vector involved in the Raman process depends on the wave vector of the electrons which are excited ($q \approx 2k$, Figure 8-2). The laser energy selects the electronic wave vector k through the band structure of graphene near the K point. The disperson of the D band is 50 cm^{-1}/eV while that of the G band is nearly 100 cm^{-1}/eV. The double resonance process, therefore, carries information about both the electronic structure of graphene and the disperson of the phonons. Below, it will be shown that DRRS is useful in identifying the number of graphene layers that are being probed and that it provides information of the stacking order of the layers. In this chapter, a focus will be given to the G$'$ band due to its importance in the characterization of graphene-related materials.

The G$'$ band can be utilized to differentiate between 1-LG and 2-LG. In the case of 1-LG, the G$'$ band has a single Lorentzian peak [93]. In the case of 2-LG obtained from natural graphite or HOPG, the AB stacking (Bernal) of the layers breaks the energy symmetry of the carbon sublattices, therefore, generating two conduction bands and two valence bands for the π electrons (Figure 8-6(a)) [95]. Two subset of atoms, one

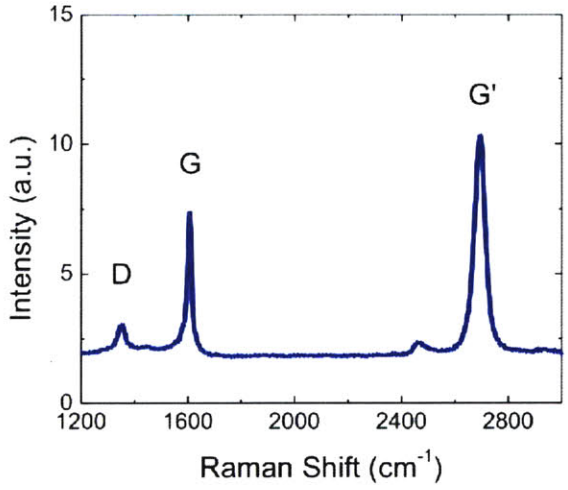

Figure 8-5: Raman spectrum of monolayer graphene.
Three peaks are observed. The G peak is a first-order process at 1580 cm^{-1}. The D peak at 1350 cm^{-1} is a one-phonon second-order process. It involves one iTO phonon and the elastic scattering with a defect. The G′ at 2700 cm^{-1} is a two-phonon (iTO) second-order process. The laser excitation wavelength is 532 nm.

from the top layer and the other from the bottom one, lay aligned on top of each other (A atoms in Figure 8-6(b)). The rest of the atoms lay at the center of the hexagons formed by the adjacent layers (B atoms in Figure 8-6(b)). These are two distinct states with different energies corresponding to the new π bands. Furthermore, the bands are not linear but parabolic near the Dirac point [95]. The existence of two bands results in eight possible double resonance Raman processes as shown in Figure 8-7 [95].ij represent the two conduction bands involved in the scattering event (1 and 2 is used for the upper and lower band, respectively). Four pairs out of the eight processes are degenerate, therefore, there are four different phonons with distinct frequency defining the Raman G′ band [95]. The lineshape of the G′ band of 2-LG is therefore changed compared to that of 1-LG (Figure 8-8(a)) allowing the distinction between the two cases in a straightforward way. The 2-LG G′ lineshape is usually fitted to four Lorentzian peaks corresponding to the four pairs of degenerate processes mentioned above. The G′ band for AB stacked graphite is also shown in Figure 8-

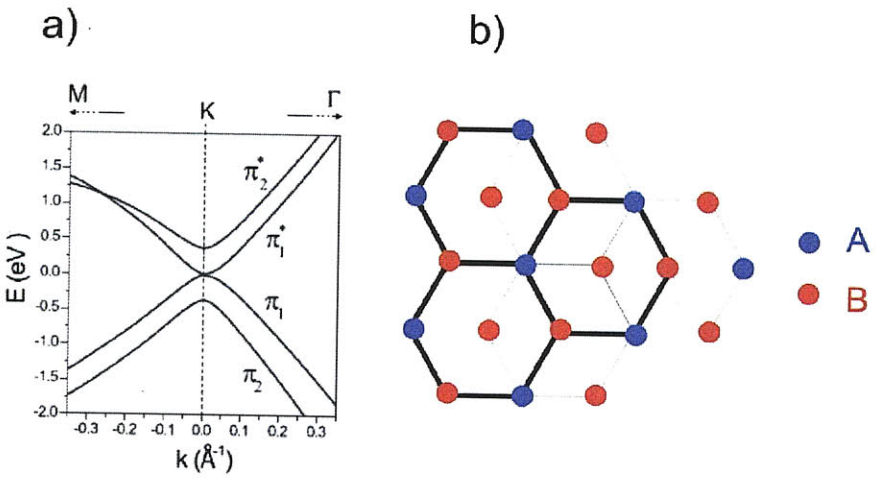

Figure 8-6: Electronic structure of 2-LG graphene.
a) Electron energy vs. electron wavevector for bi-layer graphene around the K point. The π electronic states are described by two conduction and two valence bands. b) Top view of the arrangement of carbon atoms in an AB stacked bilayer. The lattices of the first and second layer are denoted by black and gray lines, respectively. Overlapping atomic positions are shown in blue (A atoms). Atomic positions falling at the center of adjacent layers are shown in red (B atoms). Atomic positions within one layer are no longer equivalent, giving rise to two distinct electronic bands.

8(a) for comparison. Figure 8-8(b) shows the same Raman peak for higher number of layers. Notice that the G$'$ lineshape evolves towards that of graphite which is usually described with two Lorentzian peaks [93](ω_{11} and ω_{22}). The two components of the graphite G$'$ band correspond to the highest and lowest energy processes of the 2-LG case (ω_{11} and ω_{22}, respectively) [95]. The role of the AB stacking in the behavior of the G$'$ band is essential. Later it will be shown that the lineshape of the G$'$ band is useful in quantifying the degree of AB stacking in F-LG.

In the following section, the characterization of the G$'$ band of F-LG films is presented. It is shown along with electron diffraction characterization that the stacking order of the first few graphene layers of the film is turbostratic, while a higher number of layers shows some AB stacking order. These results are relevant in order to understand the electronic properties of devices made with the produced material.

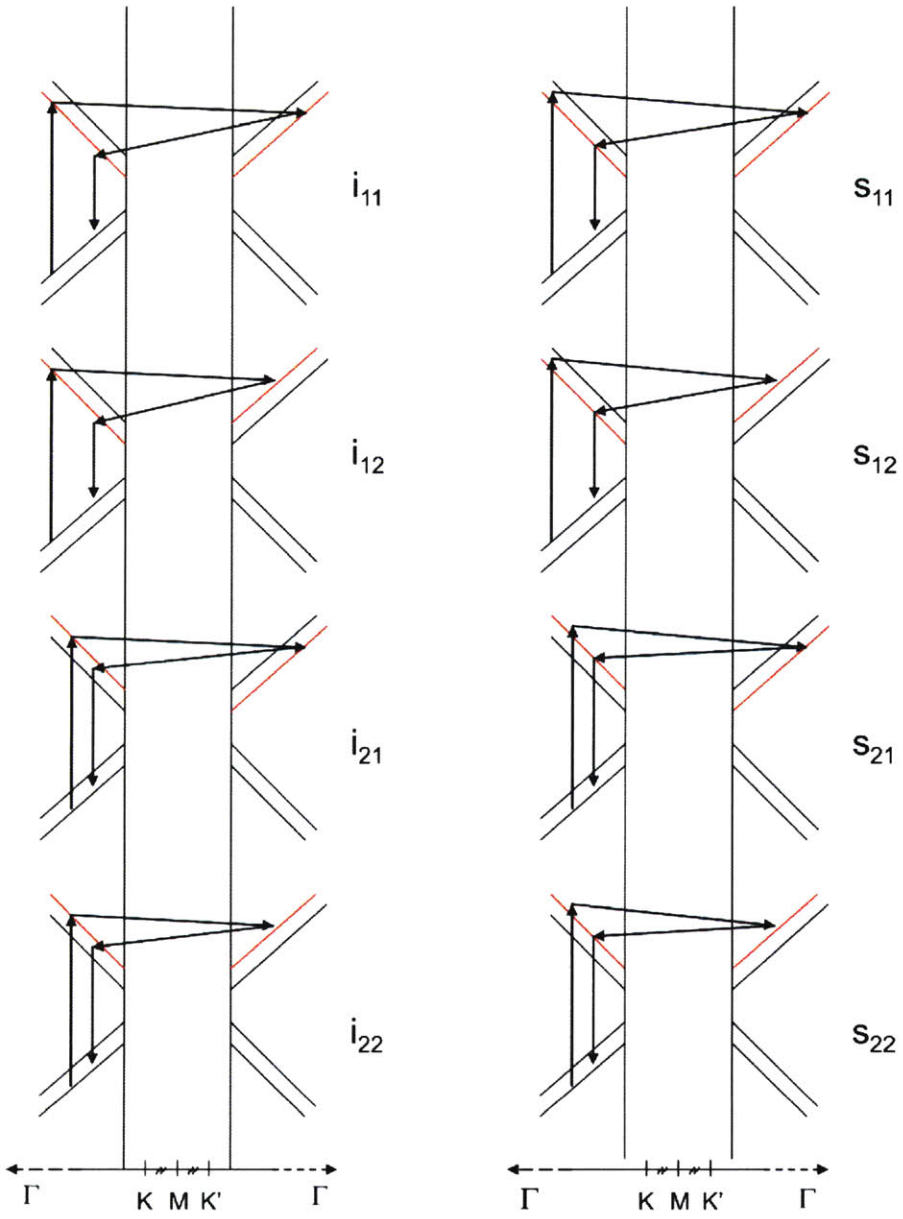

Figure 8-7: Two-phonon double resonance processes in bilayer graphene. The scattering between electronic states occurs between equivalent bands (1-1 or 2-2) or non-equivalent bands (1-2, 2-1). s=scattered resonance, i=incidence resonance. A total of eight processes are possible under this model. Four pairs of the eight cases are degenerate. Therefore the G′ band of bilayer graphene is typically fitted to four peak components.

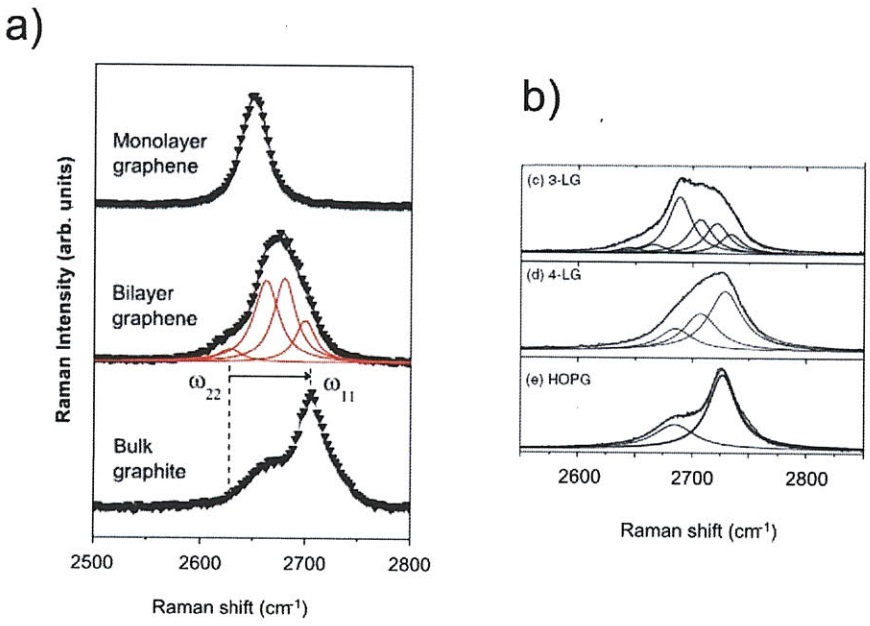

Figure 8-8: The G$'$ band for graphene, F-LG and graphite.
a)The G$'$ band of 1-LG, 2-LG and HOPG. They are fitted to 1, 4 and 2 Lorentzian peaks, respectively. The distinctive lineshapes are useful for the non-destructive identification of 1-LG and 2-LG. b) G$'$ spectra for 3-LG, 4-LG and graphite. The lineshape continues to evolve to that of graphite. From ref [95, 93]

8.3 Structural characteristics of F-LG films by Raman spectroscopy and electron diffraction studies

Raman spectroscopy is a useful characterization technique to quantify the number of layers of F-LG and to obtain information of the stacking order of the layers. Here, Raman spectroscopy is used to characterize the stacking order of F-LG derived from the CVD process described in the previous chapters. The observations made are supported by electron diffraction data obtained from suspended regions of the F-LG films. First, it is shown that the splitting of the G′ peak in 2-LG does not occur for the CVD case. This is due to the mis-orientation between layers in 2-LG which breaks the inequivalence of the A and B atoms shown in Figure 8-8(b) because the stacking is not well established and is not AB stacking. Furthermore, the evolution of the G′ lineshape is analyzed with increasing number of layers. The analysis presented suggests that AB order in the stacking of the layers increases with higher number of layers.

8.3.1 The G′ (2700 cm^{-1}) Raman peak

Representative G′ spectra of 1- and 2-LG from CVD deposited on SiO_2-Si are shown in Figure 8-9(a) and (b), respectively. Both peaks can be fitted to a single Lorentzian suggesting no splitting of the electronic bands for the 2-LG case. Figure 8-9(c) and (d) show the same peak for 1- and 2-LG from graphite acquired with the same experimental conditions used for the CVD case. The peak of 2-LG from graphite can only be fitted to 3 or 4 processes in agreement with the current literature [74, 96]. The G′ linewidths for ensembles of the four cases above are plotted in Figure 8-9(e). For CVD, the linewidths of both 1-LG and 2-LG are similar (43 cm^{-1}) and comparable to those observed for turbostratic graphite (2D graphite) [97, 98]. There is only a small increase in the spread of the measured linewidths for the 2-LG case. For graphite, there is an increase of the linewidth from 25 cm^{-1} (1 LG) to 54 cm^{-1}

(2 LG). The broadening of some of the CVD bilayers is consistent with reports of the Raman spectra of randomly folded graphene layers [99, 100]. The absence of a lineshape change and a broadening for the graphene bilayers is explained by the mis-orientation between the two layers. Such rotation would result in the recovery of the original electron energy states in 1-LG [93] as it happens in 2D graphite [97]. This is confirmed by electron diffraction data of the bi-layers (see next section). Therefore, the G′ band alone cannot be used to differentiate between 1 and 2 graphene layers obtained by the fabrication method discussed. However, it is possible to use this Raman peak to quantify the degree of stacking order in the samples.

The G′ lineshape of higher number of graphene layers shows changes suggesting the splitting of the peak into different components. As the number of graphene layers increases, the lineshape evolves to the one expected for graphite. This is shown in Figure 8-10 where representative spectra from the F-LG films are displayed. The data is fitted to a maximum of three Lorentzian peaks. Each G′ band is fitted by the least squares method to the minimum of peak components necessary to obtain a coefficient of determination above 0.99. For the case of 2-LG, only one peak is sufficient to fit the curve. For intermediate cases between 2-LG and graphite, 2 to 3 peaks are necessary. Lastly, for 20 and above layers, only 2 peaks are sufficient. The choice of a maximum of three peaks is based on the fact that the G′ band of partially ordered graphite is usually described by three peaks ω_{2D}, ω_{3DA} and ω_{3DB} [98]. Under this treatment, it is being assumed that the material being analyzed is composed by only a mixture of turbostratic and AB stacked layers. That is, an ABC stacking order is being neglected. In order to consider other types of stacking, it would be necessary to determine how the G′ lineshape would be affected by them. Detailed considerations regarding the band structure of F-LG would be necessary [101]. The first peak in the fitting corresponds to the contribution of turbostatic layers, and the other two correspond to the usual peaks observed in AB stacked graphite. Turbostratic layers lack electronic interlayer interaction, therefore, their G′ is similar to that of a monolayer of graphene but with a larger linewidth [98]. ω_{3DA} and ω_{3DB} are positioned below and above, respectively, from ω_{2D} and they arise due to the electronic interaction between the

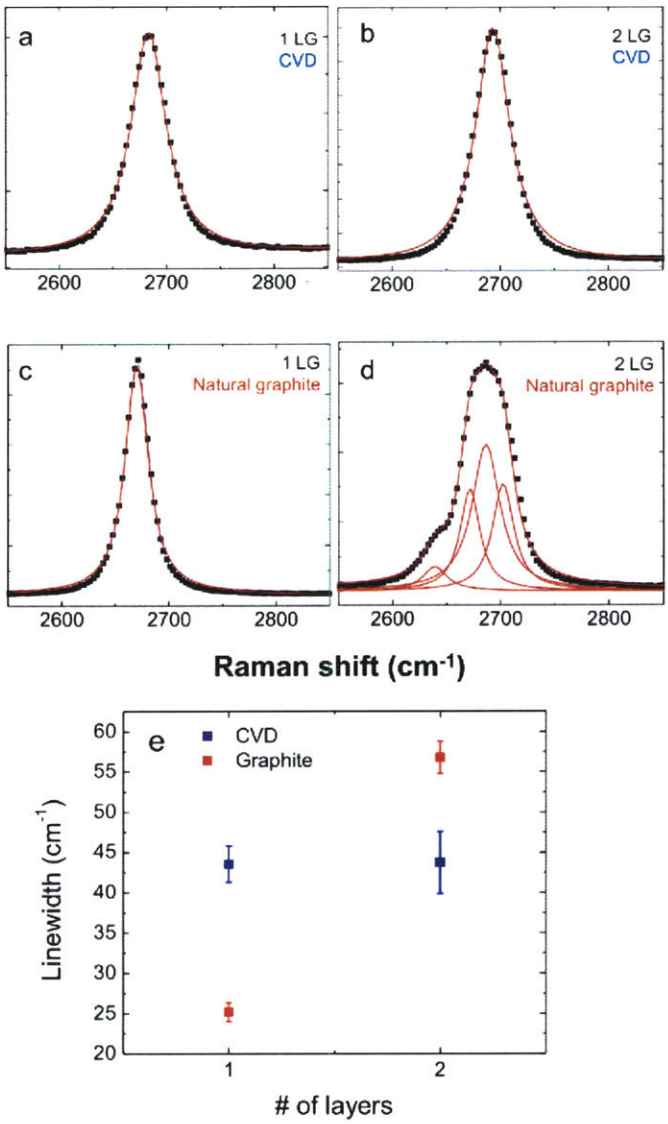

Figure 8-9: The 1-LG and 2-LG G′ band for pieces from natural graphite and CVD. The G′ band for 1-LG (a) and 2-LG (b) in F-LG films by a CVD method. No splitting is observed for 2-LG (No AB stacking of layers). The same peak for 1-LG (c) and 2-LG (d) from natural graphite obtained with the same experimental condition used for the CVD case is shown for comparison. The spectrum for 2-LG shows clearly the separation into four peaks due to the AB stacking of the layers. c) Average linewidths of an ensemble of peaks obtained from 1-LG and 2-LG from CVD (blue) and natural graphite (red). The linewidths of 1-LG and 2-LG are similar for CVD whereas there is a change of 30 cm^{-1} for natural graphite.

layers. This scheme helps in the quantification of the degree of stacking order in graphite materials as done by Cançado et al. [98]. The same approach is adopted here in order to estimate the degree of stacking order in the graphene films grown by CVD. Since the Raman signal is proportional to the volume exposed to the laser signal [97, 98], the volume fraction of AB stacked graphite can be estimated by:

$$V_{AB} = \left| \frac{I_{3DB}}{I_{3DB} + I_{2D}} \right|, \tag{8.6}$$

where I_{3DB} and I_{2D} are the integrated intensities of the ω_{3DB} and ω_{2D}, respectively. This is a relevant parameters since it allowed Cancado et al. [98] to build an empirical relationship between V_{AB} and the average interlayer spacing (c) and the coherence length (L_c) of graphite samples with turbostatic and AB stacked layers. Here, it is also assumed that the volume fraction of AB stacked layers will be proportional to the expression in equation 8.6. For a constant area of laser illumination, the number of AB stacked layers is therefore:

$$Layers_{AB} = n \times \left| \frac{I_{3DB}}{I_{3DB} + I_{2D}} \right|, \tag{8.7}$$

, where N is the total number of layers. The assignment of each of the components is done by taking the $G^{'}$ band of the turbostratic bilayers as ω_{2D} and the two peaks found in the spectra of natural graphite as ω_{3DA} and ω_{3DB} . Figure 8-10(a) compares the spectra of several F-LG graphene pieces against those of bilayer graphene (top of the figure) and natural graphite (bottom of the figure). Figure 8-10(b) shows the average frequency and integrated intensity of each component identified in an ensamble of pieces for each sample thickness. Notice that the frequency of the fitted components fall around the designated ω_{2D}, ω_{3DA} and ω_{3DB}. Deviations from the expected frequency could be attributed to different factors such as doping [102, 103] which can be expected due to the exposure to acids during transfer. Also, F-LG may be more sensitive to differences of doping between the top layers and bottom layers which may change the electronic structure of the stack [104]. Other effects include a reduction in the Fermi velocity [105] and the creation of Van Hove singularities [106]

expected for turbostratic graphene layers. Therefore a more detailed study is needed in the future for the determination of the G′ band behavior in these samples. However, the current assignment of peaks is used in order to estimate the number of AB stacked layers by the model described above.

Figure 8-11 shows the estimated volume fraction and number of layers having AB stacking obtained using equation 8.6. This is plotted against the thickness of the samples probed. It is observed that with increasing thickness, the number of layers stacked with AB sequence increases. Since no AB order is seen for 2 and 3 graphene layers, it is hypothesized that the first 3 layers growing during carbon segregation always grow misoriented between each other. However, as the growth proceeds, the top layers become ordered with an AB sequence. Electron diffraction on sections with 2 and 4 graphene layers supports this view and this is discussed in the following subsection.

8.3.2 Electron Diffraction

Electron diffraction of the F-LG films is possible by implementing a transfer process similar to the one described in chapter 3. A PMMA/graphene membrane after Ni etching is laid on top of a Quantifoil TEM grid. The grid is made out of copper and is covered by an amorphous carbon film (10 nm in thickness) with periodic circular holes with a 2 μm in diameter. When the PMMA is removed, the F-LG film lays on top of the amorphous carbon. Across the 2 μm holes, the F-LG is suspended freely. Films with a high density of 2-LG, as those shown in chapter 5 (Figure 5.1 (d)), are used for this purpose. Figure 8-12 shows optical and SEM images of the films utilized for electron diffraction measurements. The optcial image is from a film on SiO_2-Si and is shown for comparison. The SEM image is from a film deposited on a TEM grid. The regions between the graphite islands are composed mostly of 2-LG (40-60%). The circles correspond to the holes in the amorphous carbon support layer.

Figure 8-13 shows the electron diffraction pattern obtained from a 2-LG domain. The number of layers is confirmed by imaging the folding of a broken part of the 2-LG

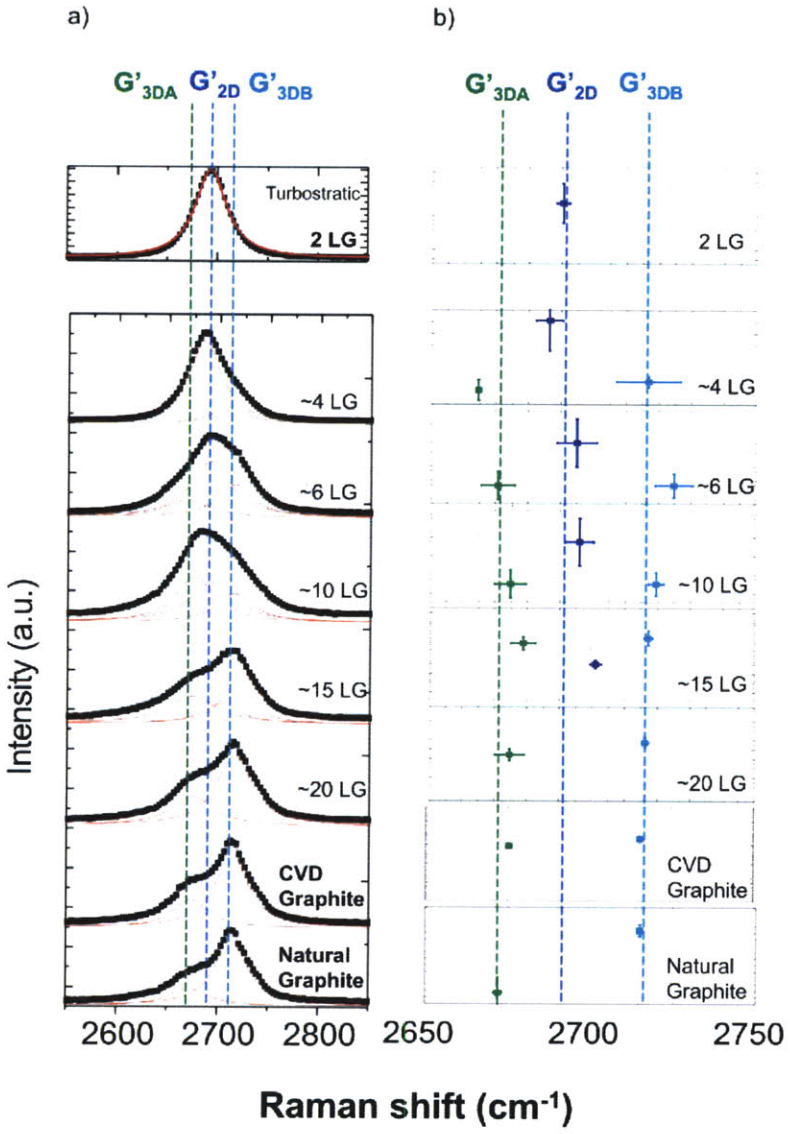

Figure 8-10: Evolution of the G′ band with increasing number of graphene layers. a) G′ band of F-LG. The lineshape evolves to the one expected for graphite with increasing number of layers. The bands are fitted to up to 3 Lorentzian peaks. Each fitted component is assigned to ω_{3DA}, ω_{3DB} or ω_{2D}. The spectra for natural graphite and turbostratic bilayers are included for comparison and are used as reference peaks for ω_{3DA}, ω_{3DB} or ω_{2D} . b) Mean frequency and integrated intensities of the components fitted to the spectra obtained from various F-LG pieces. The mean frequencies usually fall close to the ω_{3DA}, ω_{3DB} and ω_{2D} values obtained from natural graphite and 2-LG. The assignment of each component is used to quantify the degree of AB ordering in the samples.

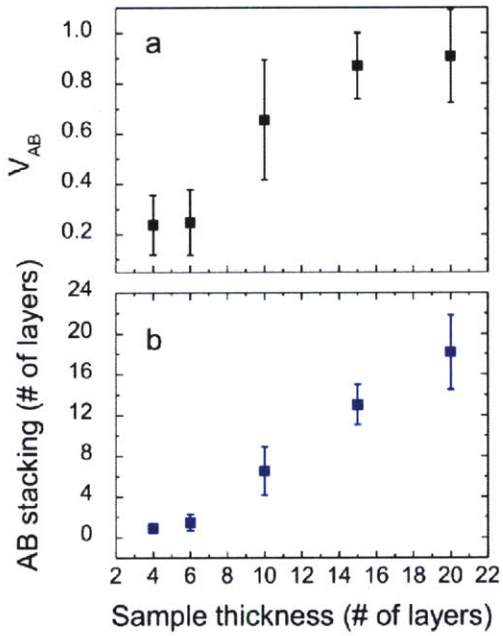

Figure 8-11: Estimation of the fraction of layers with AB stacking order. Volume fraction (a) and number of layers (b) with AB ordering as a function of F-LG thickness estimated from the integrated intensities of ω_{3DB} and ω_{2D}.

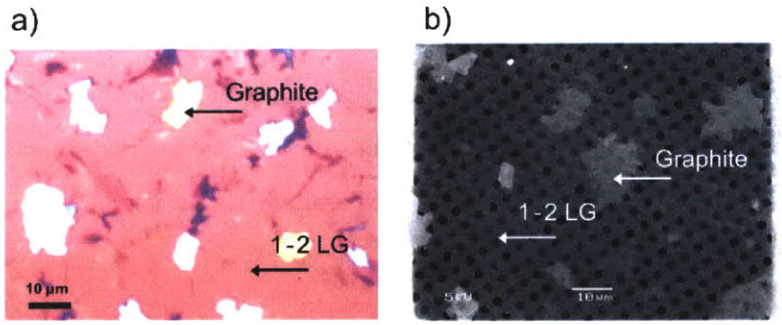

Figure 8-12: F-LG films used for electron diffraction experiments. Optical and SEM images are shown in a) and b), respectively. Isolated islands are mostly graphite. Regions between the islands correspond to monolayer or bilayer graphene.

section Figure 8-13(a). The electron diffraction pattern shows two sets of spots with the symmetry corresponding to a graphitic lattice. The misorientation measured is 20.01^o for the case shown. Other 2-LG sections show rotations between 10 and 20^o. All the bi-layers measured ($\approx$20) show a rotation and none of them show evidence of AB stacking. Therefore, it is thought that the second layer growing during the CVD process always grows misoriented with respect to the first one.

Figure 8-13 also shows the diffraction pattern from a region with an estimated number of graphene layers of $\approx$4. The number of layers is estimated from direct TEM imaging. Figure 8-13 (c) shows a low magnification TEM image of the $\approx$4 LG piece region analyzed. Notice that the piece is adjacent to a region with 2 LG. The diffraction pattern shows three sets of spots (Figure 8-13(d)). Two of them with equal intensity are likely to be from the first two graphene layers of the stack. The third and strongest set of diffraction must come from the rest of the graphene layers. Since the diffraction of the rest of the layers fall into one pattern, they must be stacked in an AB manner [107].

The electron diffraction data presented in Figure 8-13(c) supports the view that the first 2 graphene layers of the F-LG films fabricated grow with a misorientation between them. The observation shown in Figure 8-13(d) supports the hypothesis that sections with more than 3 graphene layers possess some degree of AB stacking order. The stacking order is thought to become apparent for the top layers of the multilayer stacks which are away from the Ni-graphene interface. The reason for this behavior may be multiple. The stacking order may be affected by the interaction of the Ni surface since the first graphene layer would be subject to a stronger binding than the top layers [108]. Moreover, a stronger adhesion of the first layers to the Ni surface may induce a decreased expansion of the first graphene layer with respect to the other layers during cooling. A rotation between the top layers and the first one (attached to Ni) could be induced by the wrinkle formation that occurs during cooling [55]. However, more detailed experiments with other characterization techniques would be required to determine the cause of the selective misorientation between the first graphene layers growing on the Ni surface.

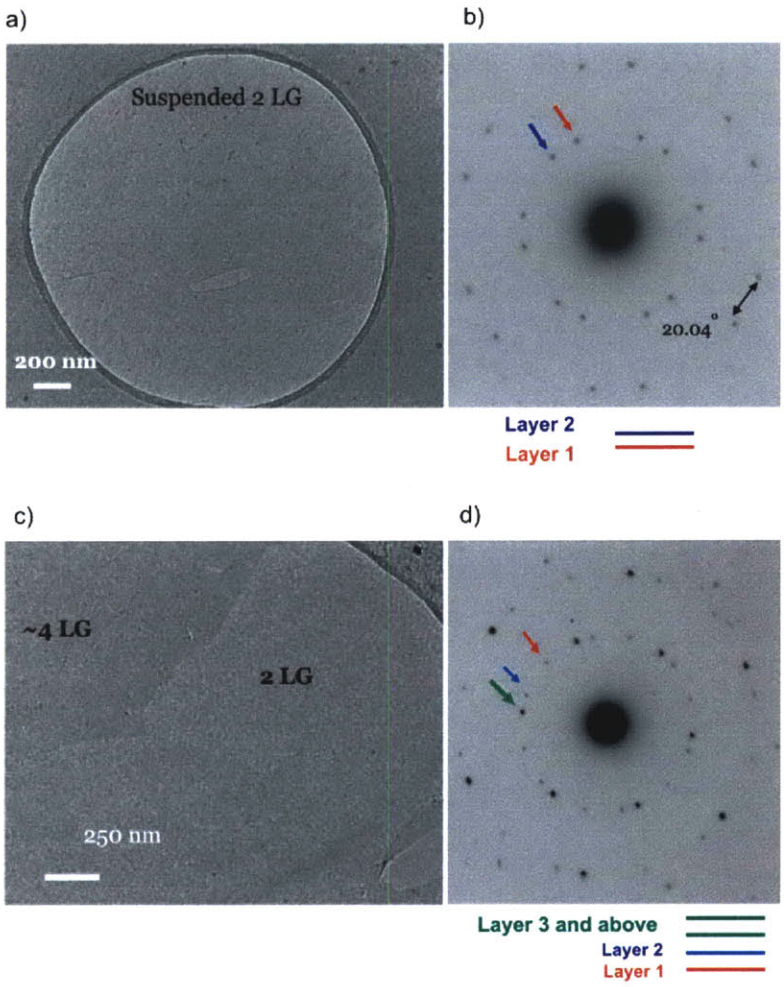

Figure 8-13: Electron diffraction results obtained from suspended F-LG films. a) Low magnification image of a 2-LG pieces suspended over one of the circular holes of a TEM grid. b) Representative electron diffraction pattern of a suspended bilayer. Two hexagonal sets of spots are visible demonstrating a rotation of 20^o between the two layers. c) Low magnification image of a 4-LG region adjacent to a 2-LG piece. d) Electron diffraction pattern of the 4 LG piece shown in c). Three hexagonal sets of spots are visible. Two of them with similar intensities likely correspond to two graphene layers. The rest of the layers create the third set which is much higher in intensity, suggesting their AB stacking order.

8.3.3 Summary

It was shown that the Raman G′ band is helpful in quantifying the degree of AB stacking in the samples fabricated. However, it cannot be used alone as a way to identify the 1-LG and 2-LG of the APCVD process. This is due to a rotation between graphene layers in 2-LG. Furthermore, it is observed that an AB stacking of layers occurs for 4 or more graphene layers on the film. However the first 2 layers are always misoriented. Because of the absence of AB stacking, the 2-LG graphene thus fabricated is expected to retain electronic properties similar to 1-LG or 2D graphite. This information may be helpful in future device prototypes in which the electronic properties of 2-LG play a critical role.

Chapter 9

Conclusions

In conclusion, the results presented demonstrate the possibility of using an ambient pressure CVD process to grow graphene films by carbon segregation. This process is expected to provide an alternative to UHV processes for large scale and throughput fabrication of graphene films. Furthermore, it was demonstrated that the graphene material so produced can be isolated from the Ni surfaces on which it is grown to integrate it to other substrates such as dielectrics on which prototype devices can be built.

Two types of Ni substrates were predominantly used. First, polycrystalline Ni thin films with thickness rage between 200 and 500 nm were used. The graphene films produced consist of domains with varying number of graphene layers. Domains of 1 and 2 LG coexist with higher number of layers and graphite on the same film structure. The film thickness uniformity can be altered by the Ni thin film grain size and the rate of carbon segregation during cooling of the films. Films with only 1 LG across their entire area are obtained by sing single crystalline Ni substrates with (111) surface orientation. This is accomplished by using a well polished Ni(111) surface and due to the thermodynamic stability of one graphene monolayer on Ni(111).

Due to the interest of 2 LG as another material for optoelectronic applications, the structure of bilayer graphene derived from this CVD method was studied. It was found that the produced bilayers are turbostratic, that is, the layers are mis-oriented between each other. This was determined by electron diffraction and Raman

spectra analysis. Furthermore, it was observed that the degree of AB stacking order increased for domains with higher number of layers (≥ 4). These observations may be of relevance if the material is to be used for electronic applications.

Future work in the graphene growth aspects of this project may include the following. More insights in the growth mechanisms are necessary in order to guide future research involving other metals, hydrocarbons and processing conditions. Many of the assumptions presented in this thesis are based on previous graphene and graphite growth in UHV conditions which may not necessarily be the best description for the APCVD process presented here. In-situ experiments for ambient pressure may be beneficial for these purposes, however, these are limited with respect to UHV in-situ experimentation due to the working pressures.

Furthermore, structural characterization of the material produced is very limited. Specifically, it will be valuable to determine the types of defects in the graphene produced. It is expected that in-plane grain boundaries and point defects are present on the graphene layers, however, currently there is a lack of quantitative information of grain size or point defect density. Because of the pressure range at which the process takes place, the polymer spin coated on the graphene surface and the chemicals utilized for transfer, it is possible that the graphene network is composed with functional groups which may affect its performance as an electronic material. Chemical characterization of possible functional groups is needed in depth for a better assessment of the quality of the material.

An important aspect of the results obtained is the high density of 2 LG on the F-LG films presented in chapter 5. Further exploration should be devoted towards the growth of uniform bilayer graphene films. Optoelectronic properties and applications of 2 LG may be distinct from those of 1 LG opening avenues for new prototype devices and applications. Lastly, it is hoped that future work leads to further improvements by exploring other growth substrates, processing and transferring conditions in order to advance the possibilities of the large scale applications of graphene materials

Appendix A

Identification of 1-LG and 2-LG

A.1 Calibration with the G channel value in RGB images of HOPG-derived graphene samples

The color contrast generated by 1-LG, 2-LG and 3-LG derived from exfoliated HOPG and deposited on 300 nm SiO2/Si is used as a calibration for the assignment of the number of layers of the CVD graphene films (also on 300nm SiO_2-Si) as described below. Figure A-1 shows microcleaved graphene pieces on 300 nm SiO_2-Si. The number of layers can be determined by inspecting the G$'$ band (2700 cm^{-1}) of the Raman spectra of the graphene pieces (Figure A-1 (b)). AFM can also assist in the layer number assignment (Figure S1c). However, the RGB (Red Green Blue) color model is a model used for displaying and representing optical images (Foley, J. D., Computer graphics: principles and practice. Addison-Wesley: Reading, Mass. 1996) and is shown here to be useful for automated characterization of the layer number assignment. In this model, each pixel of an image mixes red, green and blue light to reproduce the color of a pixel. The color obtained for each pixel depends on the intensities of the red, green and blue components that are mixed. Figure A-1(d) shows the values corresponding to the green component G extracted from the optical image along the line in Figure A-1(a). The Red, Green and Blue values of each pixel of our images are expressed on a scale of 0-255 (8-bit per channel). A stepwise change

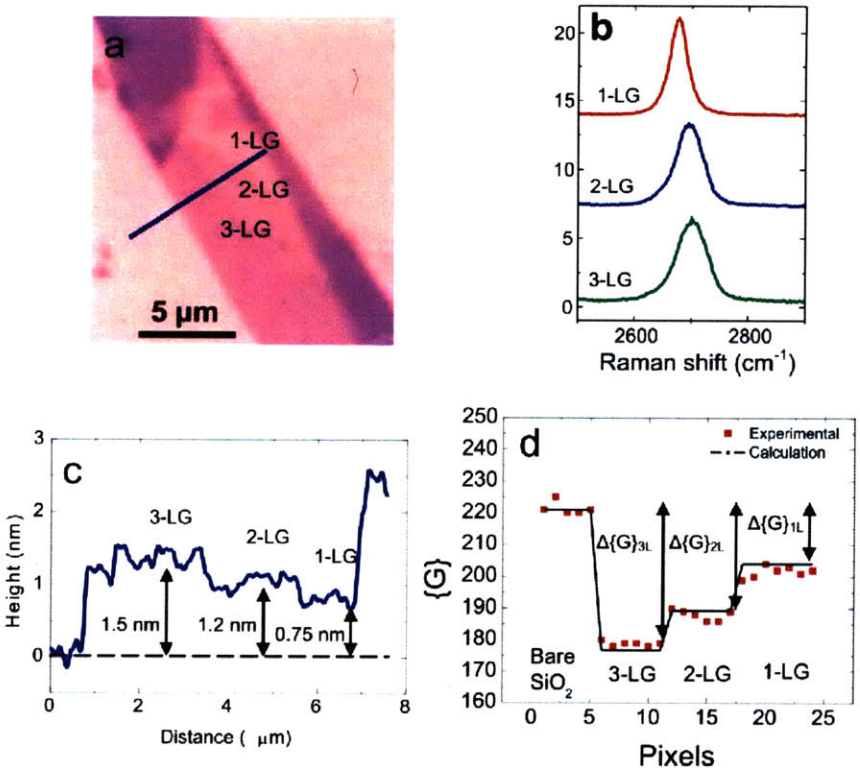

Figure A-1: Determination of number of layers with AFM, Raman and the G value. a) An optical image of microcleaved HOPG graphene (1-3 layers) on 300 nm SiO_2-Si. b) Raman spectra of the regions identified as 1, 2 or 3 graphene layers in (a). c) Measured AFM cross sectional height vs. distance corresponding to the blue line in a). d) G values extracted from the RGB values along the blue line shown in a). The black line shows the calculated G values for 1, 2 and 3 graphene layers on SiO_2 and the red points are experimental readings.

of G is observed (Figure A-1(d)) with respect to the value of G corresponding to the pixels of the bare SiO_2-Si substrate. Each step in Figure A-1(d) corresponds to the addition of one graphene layer. In Figure A-1(d), the black line shows the calculated G decrease with respect to the bare SiO_2 G value. This is obtained by calculating the reflectivity of bare SiO_2-Si and graphene on SiO_2-Si at a wavelength of 532 nm (see discussion below). The difference between the G number of graphene layers on SiO_2-Si and the G number of a bare SiO_2-Si substrate is defined as ΔG (see Figure A-1(d)). ΔG is used to determine automatically the number or layers in each optical image as shown in Figure A-1(d).

A.2 Modeling of G for graphene on SiO_2-Si

To model G of graphene layers, perpendicular incident light is considered for which the magnetic field is polarized in the z-direction. The light is incident to a system with 3 different layers; graphene, SiO_2 and Si. In each layer the magnetic field can be written as the sum of a forwards and backwards propagating wave (Figure A-2). The amplitude of the incident wave is set to 1. The magnetic field can be expressed as [109]:

$$H_{0z} = \exp(-ik_{0y}x) + A\exp(ik_{0y}x) \tag{A.1}$$

$$H_{1z} = B\exp(-ik_{1y}x) + C\exp(ik_{1y}x) \tag{A.2}$$

$$H_{2z} = D\exp(-ik_{2y}x) + F\exp(ik_{2y}x) \tag{A.3}$$

$$H_{3z} = G\exp(-ik_{3y}x), \tag{A.4}$$

where A,B,C,D,F and G are parameters, H_{iZ} is the magnetic field in z-direction and k_{iy} is the wavevector in the i^{th} layer, which can be calculated by:

$$k_{iy} = \frac{2\pi}{\lambda_0} n_i, \tag{A.5}$$

where n_i are the reflective indices, and λ_0 is the wavelength of the incident light (532 nm). The boundary conditions are:

$$H_{jz}(-dj) = H_{(j+1)z}(-dj) \tag{A.6}$$

and

$$\frac{1}{\epsilon_j}\left|\frac{dH_{jz}}{dy}\right|_{-dj} = \frac{1}{\epsilon_{j+1}}\left|\frac{dH_{(j+1)z}}{dy}\right|_{-dj} \tag{A.7}$$

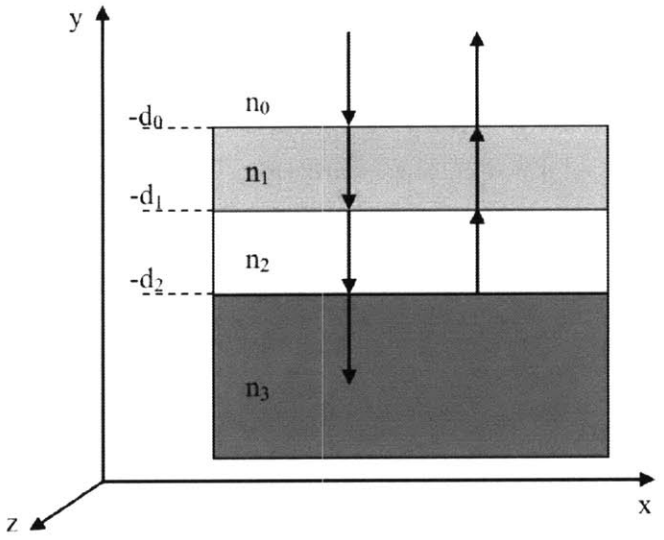

Figure A-2: Schematic of light reflection and transmission in a graphene-SiO_2-Si system.

The thickness of graphene d is estimated as d =n$\times$0.335 nm, where n is the number of layers. The thickness of SiO_2 is d_2 and the Si substrate is considered as semi-infinite, H_{jz} therefore represents the magnetic field in the z-direction, $-dj$ is the j^{th} interface and j is the dielectric function in the j^{th} layer. For this calculation the following refractive indices are used: n_0=1, n_1=2.6+1.3i, n_2=1.46, and n_3=4.15+0.044i for air, graphite, SiO_2, and Si at 532 nm, respectively.

The two boundary conditions together with the three interfaces result in six equations with six variables A,B,C,D,F and G and these equations are used to determine the six variables. A is the reflectivity and proportional to the G value in our optical images. To get the real G value of our experiment we have to multiply the reflectivity with the G value of the bare SiO_2-Si substrate, which is proportional to the illumination intensity used in the microscope settings. Now we can calculate how this value changes as a function of the number or graphene layers and the illumination conditions.

In Figure A-3, we plot ΔG as a function of the number of layers (1-LG, 2-LG and 3-LG) and the illumination (G value of the bare SiO_2-Si substrate at the same microscope illumination). Points are experimental values and lines are calculations

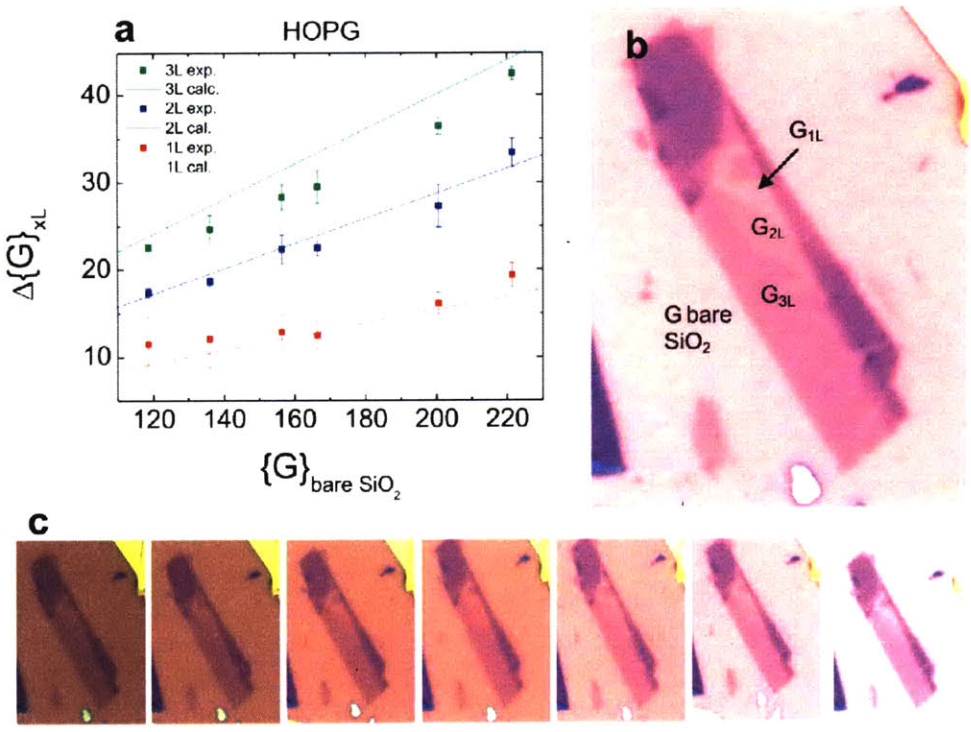

Figure A-3: Change in G for 1-LG, 2-LG and 3-LG as a function of the background G intensity.
a)Empirical dependence of ΔG_{xL} with $G_{bareSiO_2}$ for 1-LG, 2-LG and 3-LG. Calculation results are shown as solid lines. b)Optical image of the regions used to acquire the data for a). c) Examples of different illumination intensities which were used to extract the data plotted in a).

derived from above. Changes in the illumination intensities can be monitored by the G value of the bare SiO_2 background. The plot in Figure A-3(a) is a plot of ΔG for 1-LG, 2-LG and 3-LG vs. the G value of the bare SiO_2 next to them (proportional to illumination). The effect of illumination was considered since on the same optical image, the illumination can change depending on the pixel position (higher illumination at the center with respect to the corners). The same color scale settings are used for every image in the software utilized for acquiring them.

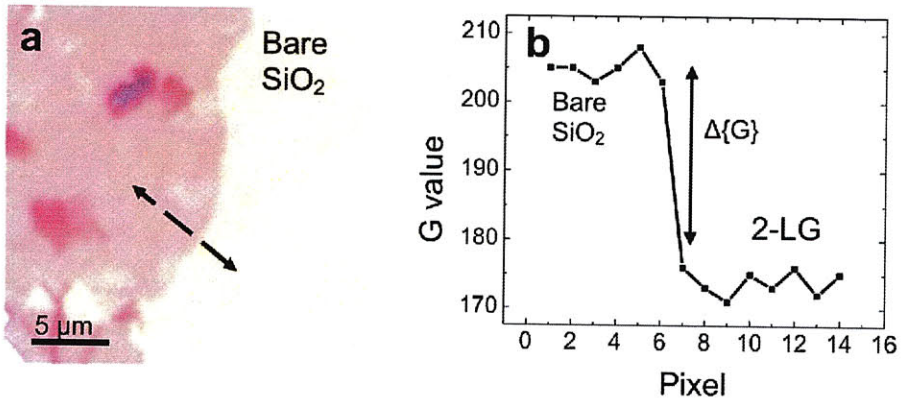

$G_{bare\ SiO2}$=204.83 (illumination)

Δ{G}= 30.95 (measured above)
Assignment: 2L
Expected for 2L = 32.23 (from Figure S3a)

Figure A-4: Example of color contrast identification of 1-LG and 2-LG.
a) Optical image of another CVD graphene region on SiO_2-Si. (b) G values corresponding to the dashed line shown in (a). ΔG values for these regions are extracted from (b) and compared to the expected values for 1-2 LG as suggested by the fits in Fig. S3a.

A.3 Quantification of the area covered by 1-LG and 2-LG CVD graphene layers using optical images

For illustration, Figure A-4 shows the determination of ΔG for a specific CVD graphene region with a particular illumination. The observed values of ΔG closely match the expected values for HOPG-derived 1-2 LG at the same illumination. These assignments are also consistent with AFM height measurements.

To quantify θ_{1-2LG} in large areas, we use optical images taken at 50x magnification (field of view of 229×289 μm^2). The pixel to pixel distance is ≈500 nm. The distance between thickness variations in the regions composed of 1-2LG is usually much larger than this spatial resolution (typically on the order of a few microns). Therefore, images at this magnification and resolution are suitable for analyzing our

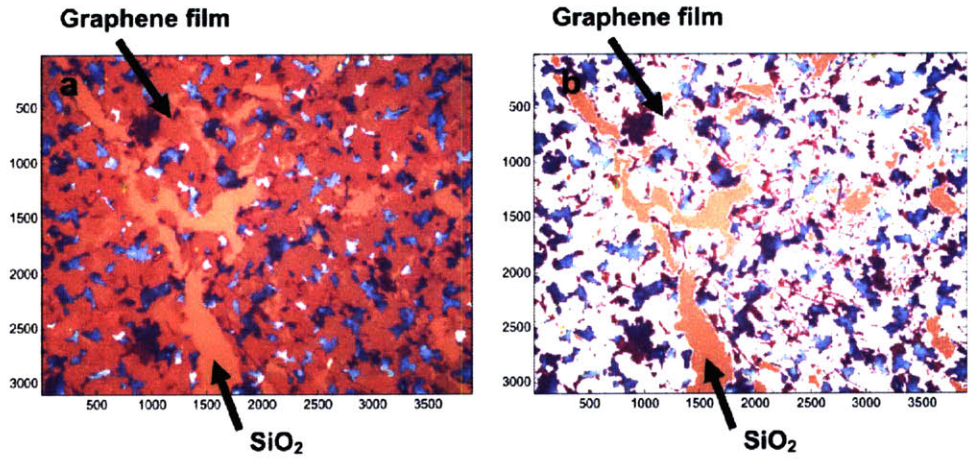

Figure A-5: Identification of 1-LG and 2-LG regions in 50× optical images. a)An optical image of a graphene film on 300 nm SiO_2. b)The same optical image as a) with pink regions in a) (1-2 LG) tagged with white in b). The film was broken (shown by upward arrow) in order to expose part of the bare SiO2 substrate and to test the algorithm. Images are 290×230 μm^2

films. Although, lower magnification images could enable the quantification of θ_{1-2LG} across larger areas of the films on SiO_2-Si, they were not used due to the increase in pixel to pixel distance.

Identification of 1-LG and 2-LG from was done in the following way. The G component of the optical images of clean SiO_2-Si was used as a background which is subtracted from the G component of the optical images of CVD graphene on SiO_2-Si. The background and CVD graphene images were taken at the same magnification and illumination conditions. The ΔG values obtained at each pixel by the subtraction were compared with the ΔG values expected for 1-LG or 2-LG (shown in Figure Figure A-3(a)) in order to label each pixel as 1-LG or 2-LG. This procedure was implemented with MATLAB and applied to multiple optical images in order to calculate the fraction of pixels corresponding to 1-LG and 2-LG in each image (θ_{1-2LG}). Figure A-5 shows an example of the identification process. Notice that the pink regions of the graphene film in Figure A-5(a) (1-2 LG) are identified effectively and tagged by the algorithm (Figure A-5(b)).

Bibliography

[1] C. Lee, X. Wei, J. W. Kysar, and J. Hone. Measurement of the elastic properties and intrinsic strength of monolayer graphene. *Science*, 321(5887):385–388, 2008.

[2] P. R. Wallace. The band theory of graphite. *Physical Review*, 71(9):622, 1947.

[3] K. S. Novoselov, A. K. Geim, S. V. Morozov, D. Jiang, M. I. Katsnelson, I. V. Grigorieva, S. V. Dubonos, and A. A. Firsov. Two-dimensional gas of massless dirac fermions in graphene. *Nature*, 438(7065):197–200, 2005.

[4] Y. B. Zhang, Y. W. Tan, H. L. Stormer, and P. Kim. Experimental observation of the quantum hall effect and berry's phase in graphene. *Nature*, 438(7065):201–204, 2005.

[5] K. I. Bolotin, K. J. Sikes, Z. Jiang, M. Klima, G. Fudenberg, J. Hone, P. Kim, and H. L. Stormer. Ultrahigh electron mobility in suspended graphene. *Solid State Communications*, 146(9-10):351–355, 2008.

[6] S. V. Morozov, K. S. Novoselov, M. I. Katsnelson, F. Schedin, D. C. Elias, J. A. Jaszczak, and A. K. Geim. Giant intrinsic carrier mobilities in graphene and its bilayer. *Physical Review Letters*, 100(1):016602–4, 2008.

[7] J. Moser, A. Barreiro, and A. Bachtold. Current-induced cleaning of graphene. *Applied Physics Letters*, 91(16):163513–3, 2007.

[8] F. Schedin, A. K. Geim, S. V. Morozov, E. W. Hill, P. Blake, M. I. Katsnelson, and K. S. Novoselov. Detection of individual gas molecules adsorbed on graphene. *Nat Mater*, 6(9):652–655, 2007.

[9] R. R. Nair, P. Blake, A. N. Grigorenko, K. S. Novoselov, T. J. Booth, T. Stauber, N. M. R. Peres, and A. K. Geim. Fine structure constant defines visual transparency of graphene. *Science*, 320(5881):1308, 2008.

[10] K. S. Novoselov, D. Jiang, F. Schedin, T. J. Booth, V. V. Khotkevich, S. V. Morozov, and A. K. Geim. Two-dimensional atomic crystals. *Proceedings of the National Academy of Sciences*, 102(30):10451–10453, 2005.

[11] S. Roddaro, P. Pingue, V. Piazza, V. Pellegrini, and F. Beltram. The optical visibility of graphene: Interference colors of ultrathin graphite on sio2. *Nano Lett.*, 7(9):2707–2710, 2007.

[12] P. Blake, E. W. Hill, A. H. Castro Neto, K. S. Novoselov, D. Jiang, R. Yang, T. J. Booth, and A. K. Geim. Making graphene visible. *Applied Physics Letters*, 91(6):063124–3, 2007.

[13] A. K. Geim. Graphene: Status and prospects. *Science*, 324(5934):1530–1534, 2009.

[14] X. Liang, Z. Fu, and S. Y. Chou. Graphene transistors fabricated via transfer-printing in device active-areas on large wafer. *Nano Lett.*, 7(12):3840–3844, 2007.

[15] Li Dongsheng, Windl Wolfgang, and P. Padture Nitin. Toward site-specific stamping of graphene. *Advanced Materials*, 21(12):1243–1246, 2009. 10.1002/adma.200802417.

[16] Xiaogan Liang, Allan S. P. Chang, Yuegang Zhang, Bruce D. Harteneck, Hyuck Choo, Deirdre L. Olynick, and Stefano Cabrini. Electrostatic force assisted exfoliation of prepatterned few-layer graphenes into device sites. *Nano Letters*, 9(1):467–472, 2008. doi: 10.1021/nl803512z.

[17] Xiaogan Liang, Valentina Giacometti, Ariel Ismach, Bruce D. Harteneck, Deirdre L. Olynick, and Stefano Cabrini. Roller-style electrostatic printing of prepatterned few-layer-graphenes. *Applied Physics Letters*, 96(1):013109–3, 2010.

[18] William S. Hummers and Richard E. Offeman. Preparation of graphitic oxide. *Journal of the American Chemical Society*, 80(6):1339–1339, 1958. doi: 10.1021/ja01539a017.

[19] Sasha Stankovich, Richard D. Piner, Xinqi Chen, Nianqiang Wu, SonBinh T. Nguyen, and Rodney S. Ruoff. Stable aqueous dispersions of graphitic nanoplatelets via the reduction of exfoliated graphite oxide in the presence of poly(sodium 4-styrenesulfonate). *Journal of Materials Chemistry*, 16(2):155–158, 2006.

[20] Sungjin Park and Rodney S. Ruoff. Chemical methods for the production of graphenes. *Nat Nano*, 4(4):217–224, 2009.

[21] Sasha Stankovich, Dmitriy A. Dikin, Richard D. Piner, Kevin A. Kohlhaas, Alfred Kleinhammes, Yuanyuan Jia, Yue Wu, SonBinh T. Nguyen, and Rodney S. Ruoff. Synthesis of graphene-based nanosheets via chemical reduction of exfoliated graphite oxide. *Carbon*, 45(7):1558–1565, 2007.

[22] Sasha Stankovich, Dmitriy A. Dikin, Geoffrey H. B. Dommett, Kevin M. Kohlhaas, Eric J. Zimney, Eric A. Stach, Richard D. Piner, SonBinh T. Nguyen, and Rodney S. Ruoff. Graphene-based composite materials. *Nature*, 442(7100):282–286, 2006.

[23] Guoxiu Wang, Juan Yang, Jinsoo Park, Xinglong Gou, Bei Wang, Hao Liu, and Jane Yao. Facile synthesis and characterization of graphene nanosheets. *The Journal of Physical Chemistry C*, 112(22):8192–8195, 2008.

[24] Yongchao Si and Edward T. Samulski. Synthesis of water soluble graphene. *Nano Letters*, 8(6):1679–1682, 2008.

[25] Dan Li, Marc B. Muller, Scott Gilje, Richard B. Kaner, and Gordon G. Wallace. Processable aqueous dispersions of graphene nanosheets. *Nat Nano*, 3(2):101–105, 2008.

[26] Yenny Hernandez, Valeria Nicolosi, Mustafa Lotya, Fiona M. Blighe, Zhenyu Sun, Sukanta De, I. T. McGovern, Brendan Holland, Michele Byrne, Yurii K. Gun'Ko, John J. Boland, Peter Niraj, Georg Duesberg, Satheesh Krishnamurthy, Robbie Goodhue, John Hutchison, Vittorio Scardaci, Andrea C. Ferrari, and Jonathan N. Coleman. High-yield production of graphene by liquid-phase exfoliation of graphite. *Nat Nano*, 3(9):563–568, 2008.

[27] Xiaolin Li, Guangyu Zhang, Xuedong Bai, Xiaoming Sun, Xinran Wang, Enge Wang, and Hongjie Dai. Highly conducting graphene sheets and langmuir-blodgett films. *Nat Nano*, 3(9):538–542, 2008.

[28] Rui Hao, Wen Qian, Luhui Zhang, and Yanglong Hou. Aqueous dispersions of tcnq-anion-stabilized graphene sheets. *Chemical Communications*, (48):6576–6578, 2008. 10.1039/b816971c.

[29] Yoon-Soo Park. *SiC materials and devices.* Academic Press, San Diego, 1998.

[30] Ajit Ram Verma and P. Krishna. *Polymorphism and polytypism in crystals.* Wiley, New York,, 1966.

[31] V. Ramachandran, M. Brady, A. Smith, R. Feenstra, and D. Greve. Preparation of atomically flat surfaces on silicon carbide using hydrogen etching. *Journal of Electronic Materials*, 27(4):308–312, 1998.

[32] R. Kaplan. Surface structure and composition of [beta]- and 6h-sic. *Surface Science*, 215(1-2):111–134, 1989.

[33] J. Hass, W. A. de Heer, and E. H. Conrad. The growth and morphology of epitaxial multilayer graphene. *Journal of Physics: Condensed Matter*, 20(32):323202, 2008.

[34] A. J. Van Bommel, J. E. Crombeen, and A. Van Tooren. Leed and auger electron observations of the sic(0001) surface. *Surface Science*, 48(2):463–472, 1975.

[35] J. Hass, R. Feng, T. Li, X. Li, Z. Zong, W. A. de Heer, P. N. First, E. H. Conrad, C. A. Jeffrey, and C. Berger. Highly ordered graphene for two dimensional electronics. *Applied Physics Letters*, 89(14), 2006.

[36] J. Hass, F. Varchon, J. E. Millan-Otoya, M. Sprinkle, N. Sharma, W. A. de Heer, C. Berger, P. N. First, L. Magaud, and E. H. Conrad. Why multilayer graphene on 4h-sic(000[overline 1]) behaves like a single sheet of graphene. *Physical Review Letters*, 100(12):125504–4, 2008.

[37] J. Hass, R. Feng, J. E. Millan-Otoya, X. Li, M. Sprinkle, P. N. First, W. A. de Heer, E. H. Conrad, and C. Berger. Structural properties of the multilayer graphene/4h-sic(000[overline 1]) system as determined by surface x-ray diffraction. *Physical Review B (Condensed Matter and Materials Physics)*, 75(21):214109–8, 2007.

[38] J. Kedzierski, Hsu Pei-Lan, P. Healey, P. W. Wyatt, C. L. Keast, M. Sprinkle, C. Berger, and W. A. de Heer. Epitaxial graphene transistors on sic substrates. *Electron Devices, IEEE Transactions on*, 55(8):2078–2085, 2008.

[39] G. M. Rutter, J. N. Crain, N. P. Guisinger, P. N. First, and J. A. Stroscio. Structural and electronic properties of bilayer epitaxial graphene. In *54th International AVS Symposium*, volume 26, pages 938–943, Seattle, Washington (USA), 2008. AVS.

[40] Konstantin V. Emtsev, Aaron Bostwick, Karsten Horn, Johannes Jobst, Gary L. Kellogg, Lothar Ley, Jessica L. McChesney, Taisuke Ohta, Sergey A. Reshanov, Jonas Rohrl, Eli Rotenberg, Andreas K. Schmid, Daniel Waldmann, Heiko B. Weber, and Thomas Seyller. Towards wafer-size graphene layers by atmospheric pressure graphitization of silicon carbide. *Nat Mater*, 8(3):203–207, 2009.

[41] P. E. I. Ching Li. Preparation of single-crystal graphite from melts. *Nature*, 192(4805):864–865, 1961.

[42] A. E. B. Presland and P. L. Walker. Growth of single-crystal graphite by pyrolysis of acetylene over metals. *Carbon*, 7(1):1–4, 1969.

[43] I. Minkoff and I. Einbinder. Dendritic growth of graphite from melts. *Nature*, 194(4830):765–766, 1962.

[44] S. B. Austerman, S. M. Myron, and J. W. Wagner. Growth and characterization of graphite single crystals. *Carbon*, 5(6), 1967.

[45] F. J. Derbyshire, A. E. B. Presland, and D. L. Trimm. The formation of graphite films by precipitation of carbon from nickel foils. *Carbon*, 10(1):114, IN21, 115–114, IN21, 115, 1972.

[46] F. J. Derbyshire, A. E. B. Presland, and D. L. Trimm. Graphite formation by the dissolution–precipitation of carbon in cobalt, nickel and iron. *Carbon*, 13(2):111–113, 1975.

[47] J. C. Shelton, H. R. Patil, and J. M. Blakely. Equilibrium segregation of carbon to a nickel (111) surface: A surface phase transition. *Surface Science*, 43(2):493–520, 1974.

[48] Peter W. Sutter, Jan-Ingo Flege, and Eli A. Sutter. Epitaxial graphene on ruthenium. *Nat Mater*, 7(5):406–411, 2008. 10.1038/nmat2166.

[49] Peter W. Sutter, Jan-Ingo Flege, and Eli A. Sutter. Epitaxial graphene on ruthenium. *Nat Mater*, 7(5):406–411, 2008.

[50] B. C. Banerjee, T. J. Hirt, and P. L. Walker. Pyrolytic carbon formation from carbon suboxide. *Nature*, 192(4801):450–451, 1961. 10.1038/192450a0.

[51] Alexander E. Karu and Michael Beer. Pyrolytic formation of highly crystalline graphite films. *Journal of Applied Physics*, 37(5):2179–2181, 1966.

[52] A. R. Ubbelohde, D. A. Young, and A. W. Moore. Annealing of pyrolytic graphite under pressure. *Nature*, 198(4886):1192–1193, 1963.

[53] Masako Yudasaka, Rie Kikuchi, Takeo Matsui, Yoshimasa Ohki, Mark Baxendale, Susumu Yoshimura, and Etsuro Ota. Graphite formation on ni film by chemical vapor deposition. *Thin Solid Films*, 280(1-2):117–123, 1996.

[54] Yudasaka Masako, Kikuchi Rie, Ohki Yoshimasa, and Yoshimura Susumu. Graphite growth influenced by crystallographic faces of ni films. *Journal of Vacuum Science and Technology A: Vacuum, Surfaces, and Films*, 16(4):2463–2465, 1998.

[55] A. N. Obraztsov, E. A. Obraztsova, A. V. Tyurnina, and A. A. Zolotukhin. Chemical vapor deposition of thin graphite films of nanometer thickness. *Carbon*, 45(10):2017–2021, 2007. doi: DOI: 10.1016/j.carbon.2007.05.028.

[56] M. Yudasaka, R. Kikuchi, T. Matsui, H. Kamo, Y. Ohki, S. Yoshimura, and E. Ota. Graphite thin film formation by chemical vapor deposition. *Applied Physics Letters*, 64(7):842–844, 1994.

[57] A. Nagashima, N. Tejima, and C. Oshima. Electronic states of the pristine and alkali-metal-intercalated monolayer graphite/ni(111) systems. *Physical Review B*, 50(23):17487, 1994.

[58] Y. Gamo, A. Nagashima, M. Wakabayashi, M. Terai, and C. Oshima. Atomic structure of monolayer graphite formed on ni(111). *Surface Science*, 374(1-3):61–64, 1997.

[59] D. Farias, A. M. Shikin, K. H. Rieder, and S. Dedkov Yu. Synthesis of a weakly bonded graphite monolayer on ni(111) by intercalation of silver. *Journal of Physics: Condensed Matter*, (43):8453, 1999.

[60] Elena Loginova, Norman C. Bartelt, Peter J. Feibelman, and Kevin F. McCarty. Evidence for graphene growth by c cluster attachment. *New Journal of Physics*, 10(9):093026, 2008.

[61] Xuesong Li, Weiwei Cai, Jinho An, Seyoung Kim, Junghyo Nah, Dongxing Yang, Richard Piner, Aruna Velamakanni, Inhwa Jung, Emanuel Tutuc, Sanjay K. Banerjee, Luigi Colombo, and Rodney S. Ruoff. Large-area synthesis of high-quality and uniform graphene films on copper foils. *Science*, 324(5932):1312–1314, 2009.

[62] Xuesong Li, Weiwei Cai, Luigi Colombo, and Rodney S. Ruoff. Evolution of graphene growth on ni and cu by carbon isotope labeling. *Nano Letters*, 9(12):4268–4272, 2009.

[63] A. LeClaire. 8.2 diffusion tables for c, n, and o in metals. In *Diffusion in Solid Metals and Alloys*, pages 473–485. 1990.

[64] Lijie Ci, Zhiping Xu, Lili Wang, Wei Gao, Feng Ding, Kevin Kelly, Boris Yakobson, and Pulickel Ajayan. Controlled nanocutting of graphene. *Nano Research*, 1(2):116–122, 2008.

[65] Chae Seung Jin, Gne Fethullah, scedil, Kim Ki Kang, Kim Eun Sung, Han Gang Hee, Kim Soo Min, Shin Hyeon-Jin, Yoon Seon-Mi, Choi Jae-Young, Park Min Ho, Yang Cheol Woong, Pribat Didier, and Lee Young Hee. Synthesis of large-area graphene layers on poly-nickel substrate by chemical vapor deposition: Wrinkle formation. *Advanced Materials*, 21(22):2328–2333, 2009.

[66] T. G. Kollie. Measurement of the thermal-expansion coefficient of nickel from 300 to 1000 k and determination of the power-law constants near the curie temperature. *Physical Review B*, 16(11):4872, 1977.

[67] Hugh O. Pierson. *Handbook of carbon, graphite, diamond, and fullerenes : properties, processing, and applications.* Noyes Publications, Park Ridge, N.J., U.S.A., 1993.

[68] Chun-Chung Chen, Wenzhong Bao, Jesse Theiss, Chris Dames, Chun Ning Lau, and Stephen B. Cronin. Raman spectroscopy of ripple formation in suspended graphene. *Nano Letters*, 9(12):4172–4176, 2009.

[69] K.V. Emtsev, Th. Seyller, F. Speck, L. Ley, P. Stojanov, J.D. Riley, and R.G.C. Leckey. Initial stages of the graphite-sic(0001) interface formation studied by photoelectron spectroscopy. *Materials Science Forum*, 556-557:525–528, 2007.

[70] Liying Jiao, Ben Fan, Xiaojun Xian, Zhongyun Wu, Jin Zhang, and Zhongfan Liu. Creation of nanostructures with poly(methyl methacrylate)-mediated nanotransfer printing. *Journal of the American Chemical Society*, 130(38):12612–12613, 2008.

[71] F. Tuinstra and J. L. Koenig. Raman spectrum of graphite. *The Journal of Chemical Physics*, 53(3):1126–1130, 1970.

[72] M. S. Dresselhaus, G. Dresselhaus, R. Saito, and A. Jorio. Raman spectroscopy of carbon nanotubes. *Physics Reports-Review Section of Physics Letters*, 409(2):47–99, 2005.

[73] A. C. Ferrari and J. Robertson. Interpretation of raman spectra of disordered and amorphous carbon. *Physical Review B*, 61(20):14095, 2000.

[74] A. C. Ferrari, J. C. Meyer, V. Scardaci, C. Casiraghi, M. Lazzeri, F. Mauri, S. Piscanec, D. Jiang, K. S. Novoselov, S. Roth, and A. K. Geim. Raman spectrum of graphene and graphene layers. *Physical Review Letters*, 97(18):187401–4, 2006.

[75] C. V. Thompson. Grain growth in thin films. *Annual Review of Materials Science*, 20(1):245–268, 2003.

[76] R. Carel, C. V. Thompson, and H. J. Frost. Computer simulation of strain energy effects vs surface and interface energy effects on grain growth in thin films. *Acta Materialia*, 44(6):2479–2494, 1996.

[77] Carl V. Thompson and Roland Carel. Stress and grain growth in thin films. *Journal of the Mechanics and Physics of Solids*, 44(5):657–673, 1996.

[78] J. E. Palmer, C. V. Thompson, and Henry I. Smith. Grain growth and grain size distributions in thin germanium films. *Journal of Applied Physics*, 62(6):2492–2497, 1987.

[79] H. J. Frost, C. V. Thompson, and D. T. Walton. Simulation of thin film grain structures–i. grain growth stagnation. *Acta Metallurgica et Materialia*, 38(8):1455–1462, 1990.

[80] W. W. Mullins. The effect of thermal grooving on grain boundary motion. *Acta Metallurgica*, 6(6):414–427, 1958.

[81] Zhinan An, Hong Ding, Qingping Meng, and Yonghua Rong. Kinetic equation of the effect of thickness on grain growth in nanocrystalline films. *Scripta Materialia*, 61(11):1012–1015, 2009.

[82] M. Eizenberg and J. M. Blakely. Carbon monolayer phase condensation on ni(111). *Surface Science*, 82(1):228–236, 1979.

[83] L. C. Isett and J. M. Blakely. Binding of carbon atoms at a stepped - ni surface. *Journal of Vacuum Science and Technology*, 12(1):237–241, 1975.

[84] L. C. Isett and J. M. Blakely. Binding energies of carbon to ni(100) from equilibrium segregation studies. *Surface Science*, 47(2):645–649, 1975.

[85] L. C. Isett and J. M. Blakely. Segregation isosteres for carbon at the (100) surface of nickel. *Surface Science*, 58(2):397–414, 1976.

[86] Gruneis Alexander, Kummer Kurt, and V. Vyalikh Denis. Dynamics of graphene growth on a metal surface: a time-dependent photoemission study. *New Journal of Physics*, (7):073050, 2009.

[87] Shigemitsu Nakanishi and Tetsuo Horiguchi. Surface lattice constants of si(111), ni(111) and cu(111). *Japanese Journal of Applied Physics*, 20(3):L214–L216, 1981.

[88] P.A. Dowben and A. Miller. *Surface Segregation Phenoman.* CRC Press, Boca Raton, FL, 1990.

[89] W.W. Dunn, R.B. McLellan, and W.A. Oates. Segregation isosteres for carbon at the (100) surface of nickel. *Trans. AIME*, 242:2129, 1968.

[90] David A. Porter, K. E. Easterling, and Mohamed Y. Sherif. *Phase transformations in metals and alloys.* CRC Press, Boca Raton, FL, 3rd ed. edition, 2009.

[91] Helen E. Grenga and Kenneth R. Lawless. Active sites for heterogeneous catalysis. *Journal of Applied Physics*, 43(4):1508–1514, 1972.

[92] A. Jorio, R. Saito, G. Dresselhaus, and M. S. Dresselhaus. *Raman spectra of graphene related systems.* Unpublished, 2009.

[93] L. M. Malard, M. A. Pimenta, G. Dresselhaus, and M. S. Dresselhaus. Raman spectroscopy in graphene. *Physics Reports*, 473(5-6):51–87, 2009.

[94] R. Saito, G. Dresselhaus, and M. S. Dresselhaus. *Physical properties of carbon nanotubes.* Imperial College Press, London, 1998.

[95] L. G. Canado, A. Reina, J. Kong, and M. S. Dresselhaus. Geometrical approach for the study of g[sup [prime]] band in the raman spectrum of monolayer graphene, bilayer graphene, and bulk graphite. *Physical Review B (Condensed Matter and Materials Physics)*, 77(24):245408–9, 2008.

[96] J. S. Park, A. Reina, R. Saito, J. Kong, G. Dresselhaus, and M. S. Dresselhaus. G' band raman spectra of single, double and triple layer graphene. *Carbon*, 47(5):1303–1310, 2009.

[97] E. B. Barros, N. S. Demir, A. G. Souza Filho, J. Mendes Filho, A. Jorio, G. Dresselhaus, and M. S. Dresselhaus. Raman spectroscopy of graphitic foams. *Physical Review B*, 71(16):165422, 2005.

[98] L. G. Canado, K. Takai, T. Enoki, M. Endo, Y. A. Kim, H. Mizusaki, N. L. Speziali, A. Jorio, and M. A. Pimenta. Measuring the degree of stacking order in graphite by raman spectroscopy. *Carbon*, 46(2):272–275, 2008.

[99] Zhenhua Ni, Yingying Wang, Ting Yu, Yumeng You, and Zexiang Shen. Reduction of fermi velocity in folded graphene observed by resonance raman spectroscopy. *Physical Review B*, 77(23):235403, 2008.

[100] P. Poncharal, A. Ayari, T. Michel, and J. L. Sauvajol. Raman spectra of misoriented bilayer graphene. *Physical Review B*, 78(11):113407, 2008.

[101] Sylvain Latil and Luc Henrard. Charge carriers in few-layer graphene films. *Physical Review Letters*, 97(3):036803–4, 2006.

[102] A. Das, S. Pisana, B. Chakraborty, S. Piscanec, S. K. Saha, U. V. Waghmare, K. S. Novoselov, H. R. Krishnamurthy, A. K. Geim, A. C. Ferrari, and A. K. Sood. Monitoring dopants by raman scattering in an electrochemically top-gated graphene transistor. *Nat Nano*, 3(4):210–215, 2008.

[103] C. Casiraghi, S. Pisana, K. S. Novoselov, A. K. Geim, and A. C. Ferrari. Raman fingerprint of charged impurities in graphene. *Applied Physics Letters*, 91(23):–, 2007.

[104] T. Ohta, A. Bostwick, T. Seyller, K. Horn, and E. Rotenberg. Controlling the electronic structure of bilayer graphene. *Science*, 313(5789):951–954, 2006.

[105] S. Shallcross, S. Sharma, E. Kandelaki, and O. A. Pankratov. Electronic structure of turbostratic graphene. *arXiv:0910.5811v2*, 2010.

[106] Guohong Li, A. Luican, J. M. B. Lopes dos Santos, A. H. Castro Neto, A. Reina, J. Kong, and E. Y. Andrei. Observation of van hove singularities in twisted graphene layers. *Nat Phys*, 6(2):109–113, 2010.

[107] Jannik C. Meyer, A. K. Geim, M. I. Katsnelson, K. S. Novoselov, T. J. Booth, and S. Roth. The structure of suspended graphene sheets. *Nature*, 446(7131):60–63, 2007.

[108] Alexander Grneis and Denis V. Vyalikh. Tunable hybridization between electronic states of graphene and a metal surface. *Physical Review B*, 77(19):193401, 2008.

[109] Y. Y. Wang, Z. H. Ni, Z. X. Shen, H. M. Wang, and Y. H. Wu. Interference enhancement of raman signal of graphene. *Applied Physics Letters*, 92(4):043121–3, 2008.